Mini/micro Coil Design and Optimization for Wearable and Implantable Magnetic Stimulation

Changhao Ge

Submitted in fulfilment of the requirements for the

Degree of Doctor of Philosophy (PhD)

School of Engineering

College of Electronics and Nanoscale Engineering

University of Glasgow

Author's Declaration

I hereby declare that this thesis entitled, "Wearable and Implantable mini/micro-Coil Design and Optimization for Next Generation Magnetic Stimulation" submitted in partial fulfilment of the requirements of the University of Glasgow for the degree of Doctor of Philosophy represents my own work. No part of the work referred to in this thesis has been supported in the application of another degree or qualification of this university or any other university or institute of learning.

Signed:

Changhao Ge

Date: 31/05/2025

Abstract

The first-generation magnetic stimulation technology, transcranial magnetic stimulation, has been successfully applied in various neurological disorders' treatment. However, this technology's limitation is enlarged with higher requirements of stimulation precision in nowadays and the next-generation invasive and nano-invasive magnetic stimulation technologies featuring precision and wearable/implantability are in urgent need of development. As new specialized coils are considered to be key factors for the future development of the next-generation magnetic stimulation methods. Novel coil design and efficient manufacturing will significantly accelerate the development of this field. For invasive magnetic stimulation, this project proposes a hypothesis to explain the questions remain in the selective stimulation mechanism and brings up three optimization routes which enhance the resolution and selectivity. Besides, innovative laser-assisted cleanroom manufacturing process is innovated, which reduced the fabrication period from weeks to days, and meanwhile enables biocompatible integration of traditional non-biocompatible metals (such as aluminum), thereby broadening material choices and reducing costs. For nano-invasive stimulation, this project first minimizes coil designs to cm scale with generating mT level magnetic field. There are two experimental designs explored here, planar coils, and slinky coils. Three planar coil fabrication methods, laser processing, ultra-thick lithography, and physical cutting are tested, optimized, and evaluated. Here, an alignment method of laser process is brought up, an optimized recipe of ultra-thick (over ninety micrometer) photoresist method is proposed, and a cheap fast cutting fabrication method is invented reducing the cost three to four orders of magnitude. On the other hand, the first successful miniaturization of slinky coils to the centimeter scale can achieve high-intensity magnetic fields and improved high-frequency performance with resonant circuit assistance. Overall, this thesis provides cutting-edge techniques for the development of non-invasive, invasive, and nano-invasive magnetic stimulation technologies and explores the coils' design and microfabrication methods for next-generation applications. Especially, the innovation in fabrication method brings much faster fabrication speed and much lower manufacturing cost, which builds a bridge between lab research and industry/clinical wide demand. The contributions will accelerate the development and application of next-generation magnetic stimulation technologies in daily life.

Acknowledgement

First and foremost, I would like to express my deepest gratefulness to my supervisor, Prof. Hadi Heidari. I can still remember the first time we met. When I said I felt nervous, he said, "Why? I won't eat you", and then this sense of humor accompanied me in the following six years. Without your support in projects, research, and daily life, this PhD degree would not have ever been possible. Then I would like to thank my second supervisors Dr. Bhavani Prasad Yalagala, and Dr. Finlay Walton for the help in guiding me of learning skills, performing experiments, and writing papers, which transformed me to a real researcher.

I am also grateful to my colleagues in meLab. I would really like to thank Dr. Eve McGlynn and Dr. Maria Cerezo Sanchez, for their help and training in cleanroom. I will always remember the time we worked together in JWNC. Besides, I would also like to thank Jungang Zhang, Huxi Wang, Yuanxi Cheng, Siming Zuo, Yuqi Ding, and Jiaoran Wang etc. who give me a colorful life, company me the stressful time, and help me in difficulties during my whole PhD. I will never forget every meal we ate together, every place we traveled together, and every festival we celebrated together. I will never forget… Additionally, I would also like to express my gratitude to Antonia Pavlidou and Dr. Hannah Thomson for their help in revising my writing. I am thankful to everyone in (and outside of) meLab for their collaboration and support. Though members come and go, I hope we all remain part of the meLab family in spirit forever.

Finally, I would like to express my thankfulness to my beloved Yuxin Mu, who has totally changed not only my PhD journey but also possibly my entire life. Together, we created priceless memories during our 300 days in Glasgow, UK, and across Europe. Her over 900 days of accompaniment helped me overcome countless challenging and hard moments. From you, I have learned so much, and it is you who make me a better and more complete person. Last but never least, I owe endless thanks to my loving parents, who firmly support me much more than emotionally and financially. Without their unconditional love, care, patience, and belief to me, this PhD would have remained an impossible dream. I feel lucky to be your son.

Time flies mercilessly. The past four years are the most colorful pages in the book of my life, how I wish I never turn to next chapter, how I wish I never say goodbye to the characters… With a whisper of pages closing, the story takes its place among memories now, but I am still looking forward to our unexpected encounter in the future!

CONTENTS

List of Figures

List of Tables

List of Abbreviations Used

DALYs	Disability-Adjusted Life Years
2D-SM	Two-Dimensional Surface Micromachining
3D-SM	Three-Dimensional Surface Micromachining
AMF	Alternating Magnetic Field
AO	Acridine Orange
DBS	Deep Brain Stimulation
FBS	Foetal Bovine Serum
FEBID	Focused Electron Beam-Induced Deposition
H-coil	Hesed Coil
MASMCs	Mouse aorta smooth muscle cells
MEPs	Motor-Evoked Potentials
MNPs	Magnetic Nanoparticles
PBS	Phosphate-Buffered Saline
Q-factor	Quality Factor
rTMS	rapid/repetitive transcranial magnetic stimulation
SEM	Scanning Electron Microscope
TMR	Tunnel Magnetoresistance
TMS	Transcranial Magnetic Stimulation
TPP	Two-Photon Polymerization
TPR	Transient Receptor Potential
TSV	Through-Silicon Via
μMS	micro-Magnetic Stimulation

List of Symbols Used

μ	Permeability
$\vec{A}$	Magnetic vector potential
B	Magnetic flux density
$\vec{D}$	Electric displacement vector
E	Electric field intensity
e	Natural logarithm base
E_x	X direction component of electric field
E_y	Y direction component of electric field
E'	Gradient of electric field
f	Frequency
H	Magnetic field intensity
I	Current in coil
$\vec{j}$	Electric current vector
N	Number of turns
P_{heat}	Joule heat power
R	Reference resistance
r_o	Outer radius
r_i	Inner radius
R	Resistance of coil
S_0	Unit cross section area of wire
S	Gross cross section of coil holder
T_0	Reference temperature
w	Wire width
β	Temperature sensitivity coefficient
ε	Permittivity
ρ	Electric charge density
ω	Angular frequency

1 INTRODUCTION

This project's focus is mini/micro-coil design and fabrication for next-generation wearable/implantable magnetic stimulation technologies. Magnetic stimulation is a technology adopted to treat brain neurological disorders [1-7]. Compared to other neural stimulation therapies, magnetic stimulation offers several advantages. This technology does not require direct contact with tissue and exhibit excellent penetration through the human brain, which enable magnetic stimulation to minimize tissue damage in invasive applications, while in non-invasive applications, it avoids signal absorption, thereby ensuring more effective stimulation than other non-invasive methods [8, 9]. Therefore, the next-generation magnetic stimulation technologies place special emphasis on high-precision stimulation of the deep brain. Advanced accurate neurological disease treatments will greatly reduce patient suffering and social burden.

However, a major difficulty faced by the next generation of magnetic stimulation is the lack of suitable mini/micro coils. Conventional cleanroom fabrication leads to high manufacturing cost. Besides, the existing coil devices also have limitations, non-ergonomic design, that still need to be addressed for implantable/wearable applications. These problems have become a barrier preventing them from being widely accessible for clinical applications. Therefore, the project aims to design ergonomic implantable/wearable coils, keep the manufacturing cost of the coils as low as possible, reduce the production time cycle, and improve the manufacturing method to adapt to large-scale batch production, which will eventually accelerate the speed of applying these technologies in clinical situations and daily life.

This thesis describes the progress made towards addressing these limitations through three key aims since overcoming them will significantly accelerate progress in this field.

1) **Coil Parameter Optimization**: Balancing trade-offs between factors like field strength, precision, and energy, by improving coil shape, pattern, and materials etc.
2) **Fabrication Efficiency**: Simplifying fabrication processes to accelerate prototyping and iterative design refinement by using new equipment, reducing redundant steps, and applying program-assisted designing etc.
3) **Cost and Scalability**: Minimizing fabrication expenses and enabling large-scale fabrication for broader clinical and commercial adoption, by enabling to use cheaper materials, simplifying fabrication procedure, and using cost-efficient fabrication methods.

The optimized coil and fabrication methods will enable large-scale application of mini/micro-coils with very low cost, which paves the way for future laboratory results to be widely used in clinics.

1.1 Thesis Structure

The remaining chapters of the thesis are outlined below:

Chapter 2 presents a literature review focused on the development of three types of magnetic neurostimulation techniques (non-invasive, invasive, and nano-invasive) and microfabrication technologies for mini/micro-coil. The review includes the development and working principles of each approach, currently available coil designs, introduction to multiple 2D and 3D microfabrication techniques, and a discussion of the potential future applications of each stimulation technology.

Chapter 3 systematically explores the optimization of probe micro-coil for invasive magnetic stimulation. This chapter first discussed the source of the unique spatial selectivity from the probe micro-coil design. Based on this analysis, several potential improvement design strategies are proposed. Then, the fabrication process of this coil was successfully implemented, incorporating an innovative approach that integrates cleanroom recipe with laser processing. This methodological advancement has significantly enhanced production efficiency.

Chapter 4 focuses on nano-invasive magnetic stimulation and, for the first time, explores the use of ergonomic mini-coil designs instead of conventional solenoids in this field. Two potential mini-coil designs (planar coil and slinky coil) applicable to this domain are proposed and investigated with analysis of their fabrication methods and final performance. These findings contribute valuable experience to coil design in this area.

Chapter 5 gives the conclusion and future works of this project.

1.2 Publication

Journal Articles

[1] **Ge, C**., Masalehdan, T., Shojaei Baghini, M., Duran Toro, V., Signorelli, L., Thomson, H., ... & Heidari, H. (2024). Microfabrication Technologies for Nanoinvasive and High-Resolution Magnetic Neurostimulation. Advanced Science, 11(46), 2404254.

[2] **Ge, C**., Yalagala, B. P., Masalehdan, T., Shojaei Baghini, M. & Heidari, H. A Simple, Cost-effective, Ultra-fast Fabrication of Mini-coils, Using Programmable Craft Blade Cutters,

towards the Non-invasive Magnetic Applications, Advanced Engineering Materials. (Submitted)

[3] Yalagala, B. P., Masalehdan, T., **Ge, C**., Kirimi, M. T., Mercer, J., Heidari, H. Lab to fab process using ablation lasers: A light weight and flexible and biocompatible Microheaters for wearable therapy applications, ACS Applied Bio Material. (Submitted)

Conference Proceedings

[1] **Ge, C**., Walton, F., Xu, W., & Heidari, H. (2022, October). Orientationally Selective micro-Coil Design of Intracortical Magnetic Neurostimulation. In 2022 29th IEEE International Conference on Electronics, Circuits and Systems (ICECS) (pp. 1-4). IEEE.

[2] Walton, F., Cerezo-Sanchez, M., **Ge, C**., & Heidari, H. (2022, October). A Multi-Parametric Finite Element Analysis of Heat Distributions in Implanted Micro-LEDs. In 2022 29th IEEE International Conference on Electronics, Circuits and Systems (ICECS) (pp. 1-4). IEEE.

1.3 CONTRIBUTION

-The hypotheses that explain the remained questions of existing theories (invasive).

-Three optimization routes of probe coils enhancing the resolution and selectivity (invasive).

-The success application of non-biocompatible metals in probe coil (invasive).

-The miniaturized coil designs of planar coils, and slinky coils for nanoparticle application (nano-invasive).

-The 100kHz tuning of coils with resonant circuit (nano-invasive).

-The laser-assisted cleanroom manufacturing with alignment methods (fabrication).

-The optimized recipe of ultra-thick photoresist application (fabrication).

-The ultra low-cost, fast-fabrication cutting manufacturing (fabrication).

2 LITERATURE REVIEW

Over centuries of observation, experimentation, and surgical exploration, researchers have developed a deeper understanding of the human brain and nervous system [10]. Advances in generating precisely controlled artificial electrical currents and fields have further refined neurostimulation techniques [11, 12], enabling their wide applications in therapies of neurological disorders such as headaches [1], Parkinson's disease [2], and epilepsy [3]. The global burden of these disorders, measured in Disability-Adjusted Life Years (DALYs), has increased from 6.29% in 2005 to 6.39% in 2015, with prediction suggesting a rise to 6.77% by 2030 [4]. Moreover, because neurological disorders account for over 11% of global mortality annually [4], the continued development and implementation of effective neurostimulation strategies are critical to mitigating both individual suffering and societal costs in future healthcare. The development of neurostimulation techniques could potentially mitigate this condition.

Neurostimulation techniques can be systematically categorized by the type of energy used to modulate neural activity, including electrical, magnetic, optical, and acoustic stimuli (Figure 1below). Electrical neurostimulation, the most established method, employs controlled voltage and current to influence neuronal activity. However, its invasive implantation procedures or direct scalp contact with large stimulators carry risks such as pain and tissue damage [13, 14]. Optical (optogenetics) neurostimulation utilize light to activate genetically encoded photosensitive rhodopsin ion channels, enabling precise neuronal control [15]. However, as these channels are non-mammalian, optogenetics typically requires genetic modification of target neurons, raising medical and ethical concerns [16-18]. Transcranial ultrasound neurostimulation delivers focused ultrasonic waves to brain regions, but its efficacy is limited by signal absorption and attenuation [8, 9].

In contrast, magnetic neurostimulation—including non-invasive, invasive, and nano-invasive approaches—addresses many of these limitations. Non-invasive magnetic techniques induce significantly less pain than electrical stimulation [19-21], while invasive magnetic methods employ microelectronic implants to achieve high spatial resolution without genetic modification, and also yield fewer side effects than invasive electrical alternatives [22]. Nano-invasive approaches utilize magnetic nanoparticles (MNPs) for highly selective modulation with minimal invasiveness, though genetic modification is often still required. A key advantage shared by all magnetic methods is the low absorption of low-radiofrequency

(<1MHz) magnetic fields by human tissues [23]. Given these benefits, magnetic stimulation plays an important role in next generation neurostimulation therapies.

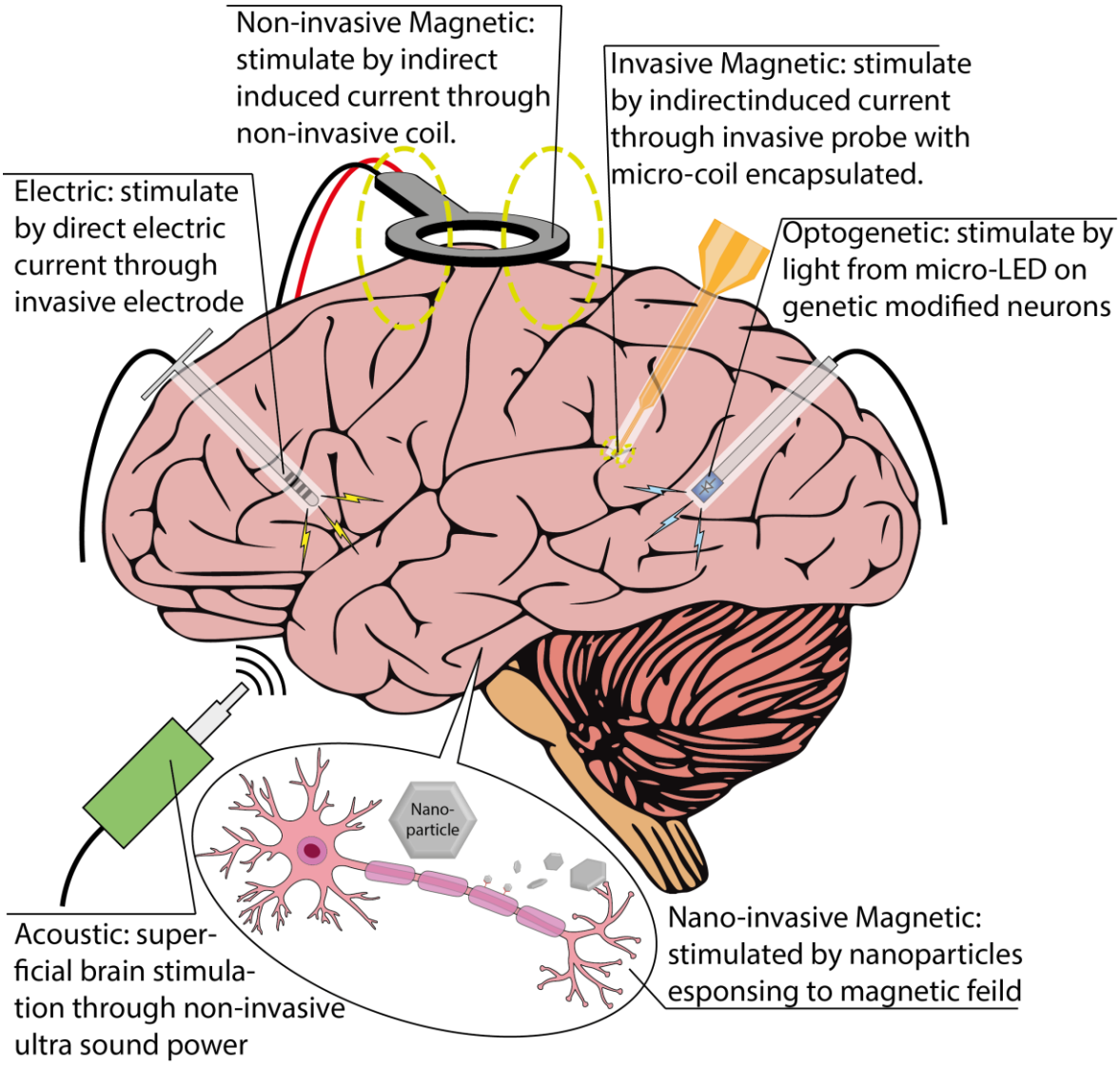

Figure 1. The schematic diagram and features of various neurostimulation approaches for the brain.

As the development potential of conventional non-invasive magnetic stimulation technologies approaches its limits, the next generation of advancements is expected to shift toward invasive and nano-invasive methods. As previously outlined, these approaches offer superior precision, enhanced selectivity, and greater compatibility with wearable applications. However, realizing these benefits relies on the development of advanced coil designs. However, next-generation magnetic stimulation coils remain underdeveloped. Notably, current nano-invasive methods in animal studies still use bulky solenoids—a design unsuitable for future human applications. Consequently, the miniaturization of coils into mini/micro-scale is critical for advancing magnetic neurostimulation technologies. To achieve the objectives, this review will focus on three critical aspects:

1) A deep understanding of the working principles of various magnetic stimulations, which is essential to determine the optimal coil designs that meet the application requirements.
2) Comprehensive analysis of existing coil designs, which is necessary to identify their limitations and potential direction of improvement.
3) Systematic evaluation of available fabrication methods, which is required to ensure the practical implementation of proposed optimal designs.

2.1 Background of Magnetic Stimulation Technologies

This section will give a brief introduction of three magnetic stimulation approaches. Figure 2 presents the development milestones of each technology and illustrate the difference between them.

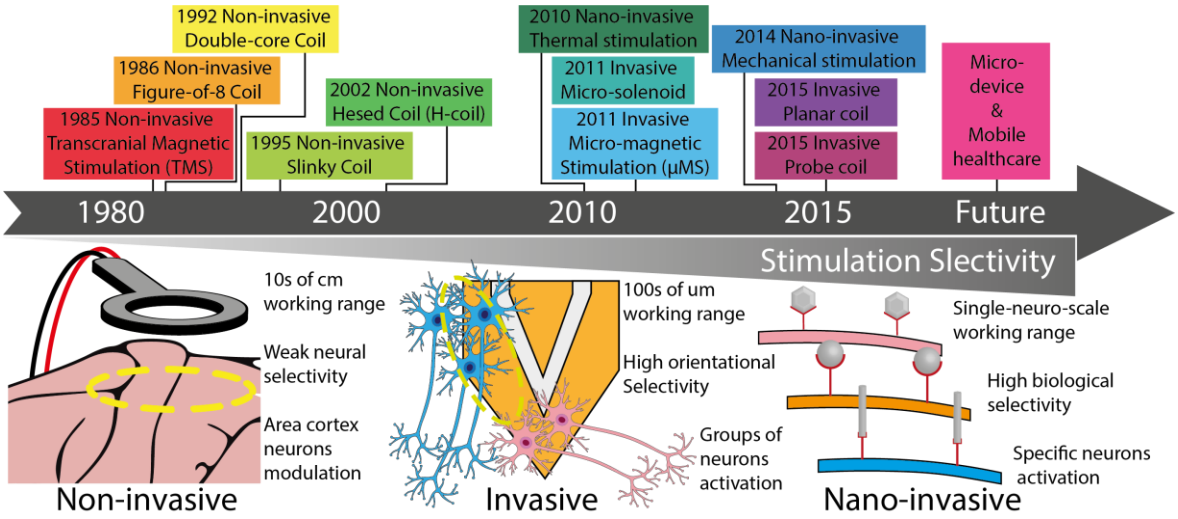

Figure 2. A brief timeline of the important event point for magnetic neurostimulations and comparison between three types of magnetic stimulation.

2.1.1 Non-invasive Neurostimulation

Non-invasive magnetic neurostimulation employs time-varying magnetic fields to induce electrical currents in biological tissues, thereby enabling targeted neural stimulation. The earliest recorded application of this principal dates back to 1896, when researchers administered cortical stimulation using a large circular coil positioned around a human's head, eliciting phosphenes, vertigo, and syncope [24, 25]. However, a real clinical application of this technology had not been developed until the 1980s, before scientists first applied magnetics stimulation to the peripheral nervous system of the human subject [26], as well as to their motor cortex [27]. The latter advancement led to the formal establishment of Transcranial Magnetic Stimulation (TMS) as a distinct therapy. As a nearly painless alternative to transcranial electrical stimulation, TMS has since then become a cornerstone technique in both neuroscientific research and clinical practice [27-30]. Following its initial

clinical validation in 1985 [31], TMS achieved widespread recognition as an important therapeutic tool by the end of the 1980s.

Up until now, TMS serves as a kind of therapy for depression [5], chronic pain management [6], seizures [7], and various other neurological disorders [32, 33]. Despite these advances, however, the technique faces inherent limitations in resolution. Even with advanced mapping protocols, TMS can achieve targeting accuracy only at the cm scale, with further degradation of precision with deeper penetration [34, 35]. This fundamental constraint significantly restricts its utility for deep brain stimulation (DBS) applications.

2.1.2 Invasive Magnetic Neurostimulation

Invasive magnetic neurostimulation was developed in order to address the spatial resolution limitation of non-invasive approaches, enabling precise targeting of small, specific brain regions. This technique utilizes implanted sub-millimeter micro-coils positioned directly within target neural tissue, achieving greater precision. Due to its μm scale, this method is also commonly known as micro-Magnetic Stimulation (μMS).

The evolution of μMS starts in 2010 with the development of mm-scale mini-coils that effectively elicited neural responses in monkeys [36]. Further advancements in 2012 yielded sub-millimeter scale coils capable of stimulating retinal neurons *in vitro* [37]. By 2013, refined micro-coil designs enabled systematic investigation of auditory pathway modulation between the cochlear nucleus and inferior colliculus [38]. A significant milestone was reached in 2014 when μMS demonstrated 70% suppression of subthalamic nucleus activity – comparable to conventional electrical neurostimulation efficacy [39]. Extensive computational modeling and experimental studies in following years have consistently validated μMS as a high-resolution magnetic stimulation approach [35, 40, 41].

Despite these advantages, μMS shares the inherent limitations of all invasive techniques, including surgical risks and potential complications associated with chronic implantation [42]. These factors must be carefully weighed against the method's superior spatial resolution when considering clinical applications.

2.1.3 Nano-invasive Magnetic Neurostimulation

Nano-invasive magnetic neurostimulation employs MNPs composed of ferromagnetic or superparamagnetic materials, typically with diameters ranging from several nanometers to hundreds of nanometers [43-45]. The biomedical application of MNPs is particularly advantageous due to its two key properties:

1) Nanoscale dimensions allows direct interaction with cellular membranes and proteins, including ion channels.
2) Its magnetic properties enable remote control at arbitrary tissue depths via external magnetic fields [46, 47].

While MNPs have been utilized in drug delivery, hyperthermia therapy, and MRI contrast enhancement for decades, their application in neurostimulation was not explored until 2010 [48-50].

The neurostimulation effects of MNPs are mediated through two types of magneto-responsive mechanisms: magneto-mechanical and magneto-thermal neurostimulation. In magneto-mechanical neurostimulation approach, the force/torque generated in the MNPs translates to stimuli for the activation of mechanosensitive ion channels such as PIEZO1 and transient receptor potential cation channel subfamily V member 4 (TRPV-4) [51-53]. In magneto-thermal neurostimulation, when external magnetic fields oscillate at frequencies of several hundred kHz, MNPs with high magnetic saturation can generate heat, a process known as magnetic hyperthermia, which is used in magneto-thermal neurostimulation targeting thermosensitive ion channels like transient receptor potential subfamily V member 1 (TRPV-1) [49, 54, 55].

Recent studies have demonstrated the exceptional spatiotemporal precision of nano-invasive neurostimulation [23, 56-61], advancing technology and their application to brain disorders. However, some of these approaches often require genetic modification of neurons to express receptors sensitive to mechanical deformation or temperature, which are not naturally prevalent in the central nervous system.

2.2 Working Principles and Coil Designs

2.2.1 Non-invasive Magnetic Neurostimulation

As the first generation of magnetic stimulation, TMS has played a major role in the advancement of magnetic neurostimulation due to its ability to modulate neuronal activity non-invasively. This section explores the operational principles of TMS and the key advancements that have enhanced its application.

2.2.1.1 Mathematical and Physical Theory

The operation of TMS is grounded in Faraday's law of electromagnetic induction, in which a time-varying magnetic field generates an electric field within brain tissue [62-65]. This induced electric field modulates transmembrane ion flow, altering the neuronal membrane

potential, either depolarizing neurons to enhance excitability or hyperpolarizing them to reduce excitability [66]. This induced electric field is instrumental in triggering neuronal activity and responses. This process plays a crucial role in eliciting neuronal activity and responses. The mathematical relationship for a sinusoidal magnetic field is expressed through the differential form of Maxwell's equations as follows:

$$\nabla \times \vec{E} = -j\omega\vec{B} \tag{2.1}$$

$$\nabla \times \vec{H} = \vec{J} + j\omega\vec{D} \tag{2.2}$$

Where, $\vec{E}$ is the electric field intensity, $\vec{H}$ the magnetic field intensity, $\vec{B} = \mu\vec{H}$ the magnetic flux density and $\vec{D} = \varepsilon\vec{E}$ is the electric displacement vector, where ε and μ are permittivity and permeability, respectively. The electric charge density and electric current density are denoted by ρ and $\vec{J}$, respectively. The angular frequency of the sinusoidal field is denoted by ω where $\omega = 2\pi f$. The presence of free charge within brain tissue is considered negligible [22, 41] and hence $\vec{E}$ can be now calculated with Eq. 2.3:

$$\vec{E} = -j\omega\vec{A} \tag{2.3}$$

The magnetic vector potential, $\vec{A}$, is:

$$\vec{A} = \frac{\mu}{4\pi}\int_V \frac{\vec{J}}{\mathrm{R}}dv \tag{2.4}$$

While the induced electric field can be expressed as:

$$\vec{E} = -j\omega\frac{\mu}{4\pi}\int_V \frac{\vec{J}}{\mathrm{R}}dv \tag{2.5}$$

In the case of a current carrying coil composed of N turns wire, Eq. 2.5 can be transformed to:

$$\vec{E} = -j\mu fNi\int_L \frac{1}{2\mathrm{R}}d\vec{l} \tag{2.6}$$

Where i is the magnitude of the input current; $d\vec{l}$ is the differential vector in the same direction as the current unit vector in a turn of wire, L is the length of integrating route for one turn, R is the distance between $d\vec{l}$ and the point of interest. Since the parameters are known, Eq. 2.6 can be utilized to calculate the induced electric field.

2.2.1.2 Realization and Improvement

A standard TMS system comprises two main components: stimulator and coil(s). Early non-invasive neurostimulation systems employed monophasic pulsed stimulation paradigms [27]. The circuit responsible for generating this pulsed signal consists of a circular coil connected

to a high-voltage source and a large capacitor, as illustrated in Figure 3. A. Initially, the capacitor is charged by the high-voltage source. When discharged, it releases a high current, peaking at thousands of amperes within μs [19, 67]. This rapid current surge generates a magnetic field pulse strong enough to induce neuronal depolarization.

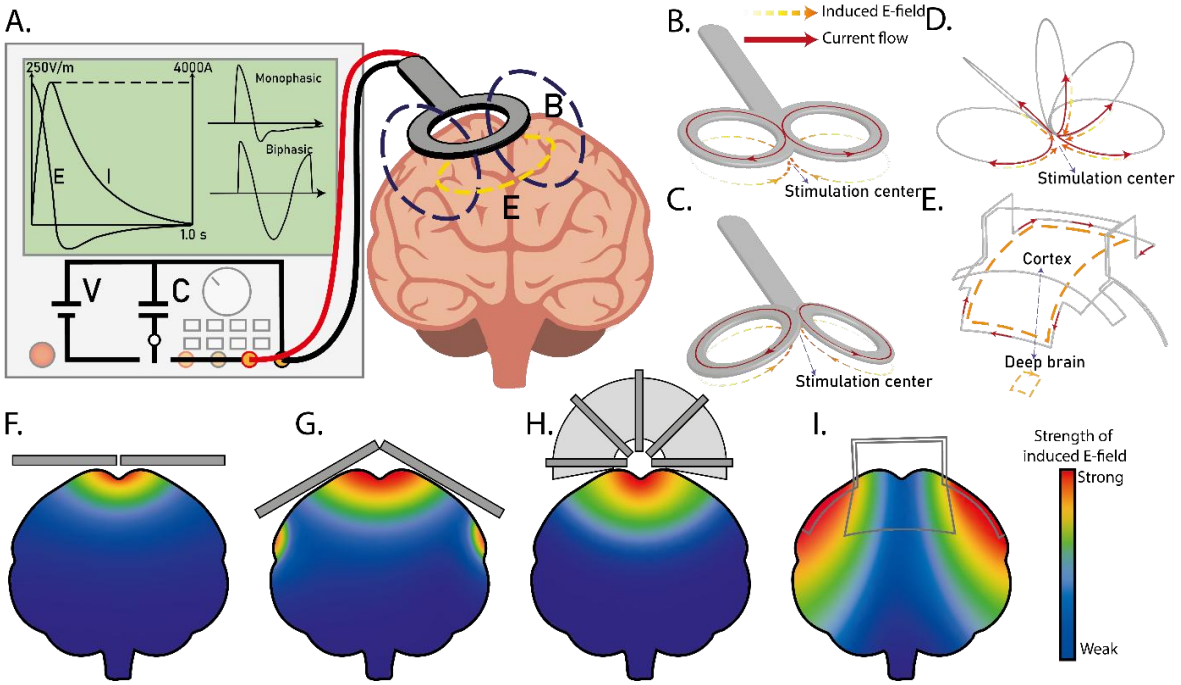

Figure 3. **A**. Working principle of first-generation TMS with example waveform. B-I, schematic diagrams of the coil and possible electric field strength distribution in the brain cross-section. In B- E, red arrows represent current flow; orange arrows represent induced electric field, deeper color means stronger field: **B**. Figure-of-8 coil, **C**. Double-core coil, **D**. Slinky coil (without core), and **E**. simplified Hesed coil / H-coil. In F-I, red transitioning to blue means strong transitioning to weak: **F**. Figure-of-8 coil, **G**. Double-core coil, **H**. Slinky coil (with core), **I**. simplified Hesed coil / H-coil.

In its early stages, TMS faced challenges in enhancing both stimulation effectiveness and spatial resolution. The effectiveness issue was primarily addressed through advancements in stimulation signals. Early TMS techniques operated at low stimulation rates, sometimes delivering fewer than one pulse every three seconds [27]. To improve efficacy, stimulation rates were increased, leading to the development of rapid or repetitive transcranial magnetic stimulation (rTMS), comprising of pulse trains at frequencies above 1 Hz [68]. Initially, despite supporting research [69, 70], concerns were raised about rTMS, particularly regarding potential tissue overheating [71, 72] and the risk of seizures [73]. However, with appropriate safety protocols, rTMS has become a widely accepted and widely used stimulation technique [74, 75], actively applied in the treatment of various conditions, including [76], movement disorder [77], and stroke rehabilitation [78]. Beyond stimulation frequency, the waveform of the pulses is another critical factor. Monophasic and biphasic pulse shapes offer distinct advantages in clinical applications. Monophasic pulses induce stronger motor-evoked

potentials (MEPs), whereas biphasic pulses result in shorter MEP latency and greater power efficiency [79-81].

Efforts to improve the spatial precision, or focality, of TMS have mainly focused on coil design advancements. Early TMS coils featured a simple flat circular shape with a diameter of approximately 10 cm, as shown in Figure 3. A [27]. However, this design did not achieve the desired level of focal neurostimulation. Studies revealed that modifying coil size alone did not significantly enhance TMS focality or efficacy [82]. As a result, research then shifted toward innovative coil designs. In decades, various coil configurations have been developed to improve stimulation focality. The following sections provide an overview of key designs and their underlying principles.

2.2.1.3 Coil Designs

2.2.1.3.1 Figure-of-8 Coil

This design consists of two flat circular coils positioned closely in the same plane, forming a figure '8' shape (Figure 3. B) [82]. A key feature of this configuration is that the input currents flow in the same direction at the center of the figure '8', where the coils intersect. As previously discussed in principle section, this arrangement enhances the induced electric field intensity at the intersection, as illustrated in Figure 3. F.

In 1988, finite element simulations and *in vivo* experiments on frog nerve-muscle systems were conducted to evaluate the feasibility of achieving localized stimulation with this coil design. The findings demonstrated that the target area exhibited a current density 2 to 3 times higher than the surrounding regions, confirming the potential of this configuration for improved focal stimulation [83]. Subsequent studies further validated its ability to generate stronger and more focused stimuli [82, 84-86]. The figure-of-8 coil significantly improved stimulation focality compared to the original TMS coil and has since become the most widely adopted design, influencing the development of miniaturized coils for next-generation magnetic neurostimulation.

Despite its advantages, the figure-of-8 coil has limitations. The stimulation strength must be carefully controlled, typically based on the motor threshold, to prevent under/overstimulation, as excessive stimulation can lead to adverse effects such as seizures [87]. Therefore, calculated by Eq. 2.6, stimulation strength decreases with distance sharply, making it challenging to generate safe and effective fields for both cortical stimulation and DBS simultaneously.

2.2.1.3.2 Double-core Coil

The double-core coil is an enhanced version of the figure-of-8 design, featuring an angular offset between the two circular coils, as shown in Figure 3. C above[88]. Recent studies indicate that this modification improves stimulation efficiency in deep brain regions compared to the traditional figure-of-8 coil. Consequently, the double-core coil is increasingly being adopted for the treatment, including depression [89], and tinnitus [90, 91].

2.2.1.3.3 Slinky Coil

The slinky coil consists of multiple coils evenly distributed along a defined path, with each coil rotating 180 degrees, as shown in Figure 3. Dabove. This configuration directs current toward a focal region, enhancing stimulation at the target area while minimizing unintended field effects in surrounding regions. Additionally, the slinky coil can be paired with a core (Figure 3. H) to further concentrate the magnetic field, increasing field density and improving efficiency compared to the standard figure-of-8 coil. By enhancing both focality and stimulation strength, the slinky coil presents a promising approach for DBS [92-96]. However, like the figure-of-8 coil, it carries the risk of overstimulation due to high current density exceeding the motor threshold.

2.2.1.3.4 Hesed Coil (H-coil)

The Hesed coil, or H-coil, is a specialized design for DBS, characterized by its complex structure, as illustrated in the simplified model in Figure 3. E above[96]. Unlike other coil designs that focus stimulation on a focal point, the H-coil distributes currents across the entire head surface. This distributed current pattern creates an additive effect, enabling effective stimulation of deep brain regions (Figure 3. I) while reducing the risk of overstimulating the cortex. Later iterations of the H-coil refined the wire layout, achieving a more uniform current distribution with a single input and output port for current flow [97, 98]. Research indicates that the H-coil can stimulate at depths of 5–6 cm [98]. Today, it is widely recognized as a promising technique for magnetic DBS [99-101]. However, the H-coil has certain drawbacks, including low selectivity, structural complexity, and its relatively large size, which may be burden for patients.

2.2.1.3.5 Other Alternative Designs

In addition to the previously discussed coil designs, several alternative configurations are worth exploring. The 'Halo coil' is a large circular coil that encircles the cranial region, typically used in conjunction with other coils, such as the H-coil and figure-of-8 coil, to enhance DBS [102, 103]. Another innovative design is the coil array [104], which consists of multiple coils arranged in sequence, with each coil controlled independently. Simulations

suggest that coil arrays enable precise targeting without requiring coil movement, while also improving power management [105]. Furthermore, combining coils, such as the figure-of-8, may enhance stimulation flexibility, strength [106], and penetration [107].

Table 1 Comparison between the four types of coils

Coil	Focality	DBS	Flexibility
Figure-of-8 Coil	√	X	√
Double-core Coil	√ √	√	√
Slinky Coil	√ √	√ √	√
Hesed Coil	X	√ √ √	X

2.2.2 Invasive Magnetic Neurostimulation

Building on the foundation of TMS, μMS operates on the same fundamental principle of inducing electrical currents in neural tissue, and thus, the stimulation principles will not be repeated here. Stimulation via μMS exhibits critical distinctions from non-invasive predecessor due to its implanted nature. The transition to invasive applications imposes strict design requirements. Implantable coils must be miniaturized to submillimeter dimensions while maintaining effective stimulation parameters. This size reduction necessitates precise placement near target neurons, making the spatial characteristics of the generated magnetic field, including its distribution and orientation, important considerations. Consequently, μMS implementations demand specialized coil configurations optimized for specific targets and applications.

2.2.2.1 Coil Design

2.2.2.1.1 Micro-solenoid

The miniaturization of conventional coil architectures to sub-millimeter scales represents a fundamental research direction in μMS. Solenoid configurations have emerged as the most used design choice due to their well-characterized electromagnetic properties. As illustrated in Figure 4. Bbelow, micro-solenoids maintain the predictable current-field relationships of their macroscopic counterparts while achieving the dimensional requirements for implanted applications, making them particularly suitable for μMS implementations.

Early research consistently identified micro-solenoids as the preferred design for micro-coils [36-38, 108, 109]. The first demonstration of micro-coil-based magnetic neurostimulation occurred in 2012 for retinal neuron stimulation [36]. Subsequent studies expanded μMS

applications to neurons in the brain [38, 108]. In 2014, *in vitro* experiments on the mouse subthalamic nucleus confirmed the effectiveness of μMS for neuronal inhibition through micro-solenoid [39]. Later advancements introduced magnetic cores to enhance field strength of it [110, 111], and recent studies have explored micro-solenoid configurations similar to the figure-of-8 configuration to improve focality [112]. Additionally, micro-solenoids have been used in various applications, including *in vivo* neuronal activation in mice [113, 114], selectivity control [115, 116], and heat dissipation management [117, 118]. These developments have established the micro-solenoid as the predominant design in μMS research.

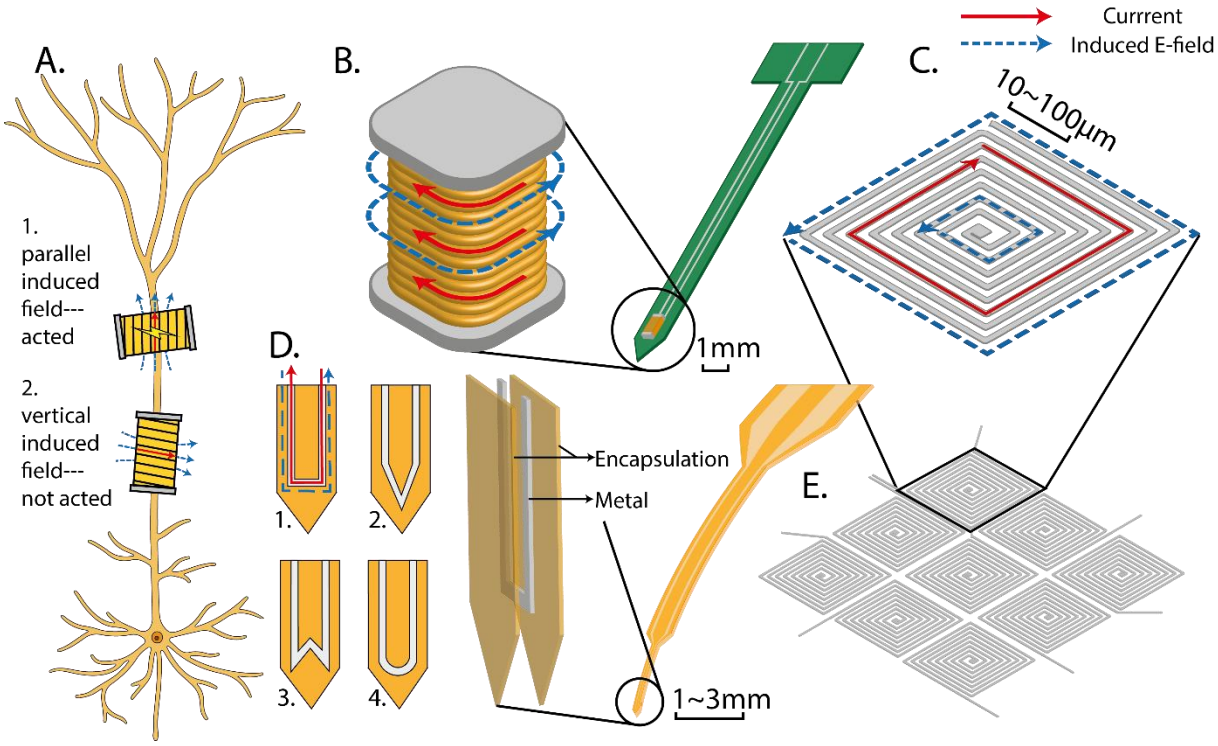

Figure 4. **A**. The orientational stimulation of neurons. The upper coil's electric field is parallel to the axon, the lower coil's is vertical. Only the upper coil successfully stimulates. **B**. The implantable micro-solenoid on a PCB and a zoom-in figure. **C**. A square planar micro-coil. **D**. The probe micro-coil with a zoom-in structure diagram and 4 example designs of coil's shapes. **E**. An example coil array with 3 x 3 square planar micro-coils.

2.2.2.1.2 Planar micro-Coil

A planar micro-coil is a flat coil arranged within a single plane, typically featuring a spiral wire layout to maximize the number of turns. An example of a square planar micro-coil is shown in Figure 4. Cabove. Due to its compact and flat structure, planar micro-coils are more suitable for under-skull implants than for DBS.

In 2015, a set of circular spiral coils with diameters ranging from 8 to 30 mm was evaluated for potential use in under-skull TMS implants. The study found that while heat dissipation

was manageable, optimizing the coil's outer diameter was crucial, as larger diameters can improve thermal management [87]. However, millimeter-scale coils were deemed unsuitable for μMS, prompting the development of a 50 μm × 50 μm square planar micro-coil. Simulations confirmed its ability to excite a 70 μm axon [119, 120]. Subsequent studies have further refined this design, consistently maintaining a sub-millimeter scale [121-124]. This advancement has been instrumental in implantable applications, leading to successful *in vivo* experiments on mice [125]. More recently, in 2021, the square planar micro-coil was incorporated into a figure-of-8 configuration to enhance stimulation focality [126, 127].

2.2.2.1.3 Probe micro-Coil

Probe micro-coils are μm-scale coils integrated into implanted prosthetic devices, often encased in a biocompatible material to enhance flexibility, as illustrated in Figure 4. Dabove [22]. These coils feature V-shape, W-shape etc. geometries designed to generate diverse electric field distributions and bring selective neurostimulation (Figure 4. A) [22, 41, 128] , which will be discussed in depth in Section 3.2. In addition to selectivity, the constrained field distribution increases the resolution. Compared to the over 1 mm activation region typical of conventional invasive electric stimulation, μMS's stimulation is typically confined to a ~300 μm diameter around the stimulation site. [22, 129]

In 2020, semi-circular probe micro-coils successfully stimulated the mouse auditory cortex, achieving a more localized stimulation region compared to conventional electrical methods [129]. By 2021, a probe micro-coil configuration incorporating a programmable circuit was introduced, enabling dynamic spatial programming to modify the stimulation focus [130]. More recently, studies have demonstrated neurostimulation propagation through visual cortex layers, highlighting the potential for stimulating complex neuronal activity [131]. Additional research has explored material effects on probe micro-coils [132] and examined thermal effects associated with their operation [133].

2.2.2.1.4 Micro-coil Array (Multi-micro-coil)

A micro-coil array consists of multiple interconnected coils designed to perform targeted neurostimulation functions [134]. Examples include planar micro-coil arrays (Figure 4. E) [119, 120, 135] and micro-solenoid arrays [136, 137]. These arrays enable precise neurostimulation by selectively activating the coil nearest to the target neuron or modulating multiple regions simultaneously. To enhance focality, some micro-solenoid and planar micro-coil arrays adopt a 'figure-of-8' configuration [112, 126]. Additionally, certain arrays integrate probe micro-coils, which allow for localized field enhancement or attenuation by adjusting the relative current directions in neighboring coils [138-140]. The ability to control each coil

independently also improves energy efficiency, which is crucial for chronic neurostimulation applications.

Table 2. Publications overtime on μMS coil design.

Year	Contribution	*in vivo*/*in vitro*	Coil type	Ref
2012	Demonstration of neuron activation via coils,	*in vitro*	Micro-solenoid	[141]
2013	Demonstration of system-level dorsal cochlear nucleus-inferior colliculus neurons activation.	*in vivo*	Micro-solenoid	[38]
2014	Adoption of micro-solenoid array	-	Micro-solenoid (array)	[134]
2014	Demonstration of cellular inhibition via micro-magnetic stimulation	*in vitro*	Micro-solenoid	[39]
2014	Demonstration of the role of field direction and single/repetitive stimulation in micro-magnetic stimulation	*in vitro*	Micro-solenoid	[142]
2016	Demonstration of feasibility of high selectivity micro-coil	*in vitro*	Probe micro-coil	[41]
2016	Adoption of planar micro-coil and planar micro-coil array	-	Planar micro-coil (array)	[119]
2017	Animal micro-coil implantation test	*in vivo*	Micro-solenoid	[113]
2018	Adoption of selective probe micro-coil designs	*in vitro*	Probe micro-coil	[22]
2019	Animal micro-coil array test	*in vivo*	Micro-solenoid (array)	[136]
2020	Adoption of probe micro-coil array	*in vitro*	Probe micro-coil (array)	[138]
2023	Adoption of ‘figure-of-8’ micro-solenoid	-	Micro-solenoid (array)	[112]

2.2.3 Nano-invasive Magnetic Neurostimulation

Nano-invasive magnetic neurostimulation represents a distinct approach compared to traditional methods like TMS and μMS. Instead of relying on electromagnetic induction, it utilizes implantable nanoparticles to influence neuronal activity. This technique introduces more complex modulation mechanisms, where multiple factors, including nanoparticle material composition, shape, ion channel targeting, and coil configuration, play crucial roles in determining efficacy.

2.2.3.1 Working Principles

Before applying a magnetic field, implanted MNPs can attach to the cell surface via two binding mechanisms: unspecific site binding through electrostatic interactions between MNPs and cell membrane without targeting specific proteins [143, 144]; specific site binding by functional coatings on MNPs to anchor directly to membrane proteins by targeting their external domains (Figure 5. A) [145].

Once the magnetic field is applied, neurostimulation can occur through two main mechanisms: magneto-mechanical modulation and magneto-thermal modulation. Magneto-mechanical neurostimulation uses a magnetic field to control mechanical forces that are applied to mechanosensory cells. This force originates from the movement of MNPs within the field. By turning the magnetic field on and off or adjusting its direction and magnitude, the nanoparticles align their torque with the external field. The movement of the MNPs can cause deformation of the cell membrane or mechanically stimulate mechanosensitive ion channels, triggering an action potential in the cell. There are mainly two types of mechanical movement in this approach:

1) Linear displacement or dragging by isotropic MNPs generating 'pull' forces in a strong magnetic field gradient (as illustrated in the transition from Figure 5. A to C) [146].
2) Rotational or twisting motion by anisotropic MNPs generating torques when aligned with external alternating fields of a few Hz with tens of mT strength (as depicted in the transition from Figure 5 A to B) [51, 147].

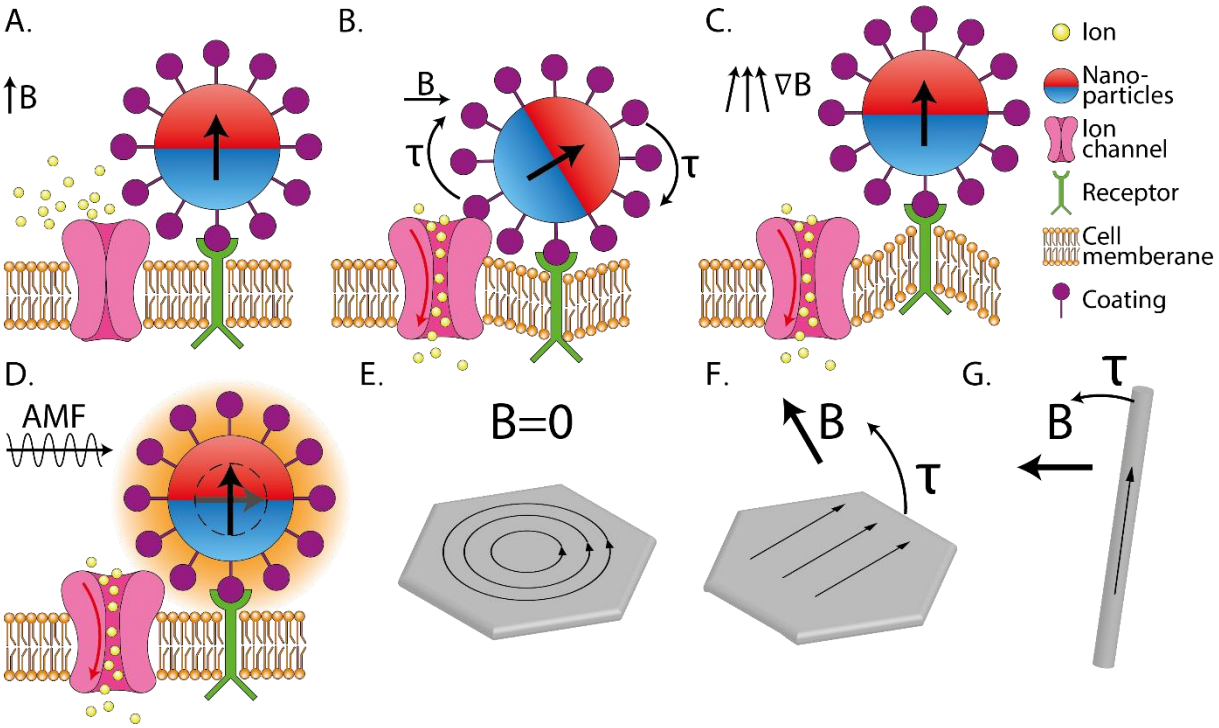

Figure 5. **A**-**D**. The schematic diagram of nano-invasive magnetic stimulation principles. **E**-**G**. Different torque of various shaped particles.

Magneto-thermal neurostimulation utilizes the heat generated by MNPs in response to an Alternating Magnetic Field (AMF) to stimulate cells. When a magnetic nanoparticle is placed in an AMF, its magnetic moment undergoes rapid changes to align with the kHz-switching magnetic field and generates heat (Figure 5. D). There are several physical principles of heat generation. In ferro/ferrimagnetic nanoparticles, the hysteresis loss, caused by shifting of the

spin domain walls during the nonlinear realignment process, dissipates heat [148]. For superparamagnetic nanoparticles sufficiently small, they will undergo relaxation losses due to their single domain spins, thus producing heat [149]. This technique is employed to induce localized heating and is commonly referred to as magnetic hyperthermia, often applied for selective cell destruction, particularly in cancer treatment [150]. Optimization of the field parameters and controllable synthesis of MNPs allows a temporary local temperature rise up to 44°C [151-153], where the heat applied is tuned to be sufficient to activate thermosensitive ion channels, but prevent the membrane and neuron integrity. This approach has been shown to be safe and effective in longitudinal *in vivo* neurostimulation studies and other clinical MNPs applications such as cancer hyperthermia [154, 155], but the clinical translation in the neurostimulation area awaits further systematic safety studies. This approach has already demonstrated usefulness in wireless DBS and applicability in behavioral and therapeutic control of neurological diseases [151, 152]. Advances with the magnetothermal approach include a demonstration of sub-second neurostimulation of temporal scale comparable to optogenetics [60], and extend towards transgene-free approaches to control activity in the deep brain [61].

2.2.3.2 Magnetic Nanoparticles

Nanoparticles serve as the central components of stimulation, and their performance in magnetic fields is primarily influenced by several factors: the choice of materials, size, shape, and crystalline anisotropy. This is a broad topic, so this section is for understanding this technology better. Therefore, the following subsections will give a more general summary of each aspect.

Material

A variety of magnetic materials are employed in the synthesis of nanoparticles, with many being based on iron (Fe) containing compounds. One common approach is to use transition metals or their alloys, such as Cobalt-Iron (CoFe) [156, 157]. However, these materials are susceptible to oxidation, which is why iron oxide, particularly magnetite (Fe_3O_4) and maghemite (γ- Fe_2O_3), are often favored. Among these, Fe_3O_4 is the most widely used choice for MNPs due to its stability, non-toxicity, cost-effectiveness, and favorable magnetic and biological properties [158-161].

In addition to pure iron oxide, MNPs can be engineered by incorporating divalent transition metal cations, such as Zn^{2+} and $Mn^{2+.}$ This modification allows for the adjustment of the saturation magnetization value of the iron oxide core. For example, nanoparticles like

$Zn_{0.2}Fe_{2.8}O_4$ [162, 163], and $(Zn_{0.4}Mn_{0.6})Fe_{2.8}O_4$ [164] have been reported to exhibit improved saturation magnetization values compared to iron oxide nanoparticles.

A core-shell structure is frequently employed in the design of magnetic nanoparticles. In this design, a core material is encapsulated by a shell that imparts additional functions. This brings an extremely diverse combination of various organic, and inorganic materials and is widely applied in bioimaging, biosensors, drug delivery, etc. [165]. As for MNPs, an example application is the $Fe@Fe_3O_4$ structure. This involves a core of Fe enclosed by a shell of Fe_3O_4. This shell can protect the high specific absorption rate of the Fe core from oxidation [166].

Shape

The shape of nanoparticles plays a crucial role in serval physiological interactions such as toxicity and cellular uptake, but importantly in magnetic neurostimulation, it influences the forces acting on MNPs in a magneto-mechanical approach. The particles in general terms can be divided into isotropic and anisotropic groups. The isotropic nanoparticles are faceted with the appearance of a sphere-like geometry, due to their cubic crystal lattice, and typically exhibit isotropic magnetic behavior, meaning their magnetic properties are uniform in all directions [167, 168]. This characteristic simplifies their response to external magnetic fields, allowing for predictable and efficient heating profiles during hyperthermia treatment when exposed to gradient magnetic fields. These nanoparticles experience forces proportional to the field gradient, leading to migration towards regions of higher field strength. The moment produced will decrease with the size of the particle reducing and with the distance from the field source increasing.

Anisotropic nanoparticles such as discs, bars, rings, clusters, etc. exhibit specific magnetic properties and can generate magnetic field forces not averagely distributed across the particle, which enables physical movement due to a change of magnetic field direction [169-171]. Among them, nano-discs and nano-bars are two representative designs. Nano-discs are typically hexagonal or square-shaped with diameters ranging from tens to hundreds of nanometers [57, 169-173]. Their thickness-to-diameter ratio gives them an almost two-dimensional (2D) appearance, which impacts their magnetic properties. These nano-discs can exhibit vortex spin alignment in their ground state. Their vortex magnetization grants them near zero net magnetization (Figure 5. E), allowing for improved colloidal stability by negligent inter-particle forces, and permits for rotational forces, “torque”. Under slow (1-20 Hz) magnetic fields during the transition to “in-plane” to align with the magnetic field direction (Figure 5. F) [57]. Nano-bars have stick shapes with lengths ranging from 100 nm to

1000 nm [174]. These structures typically feature magnetic poles at both ends, which facilitates exceptional control of their movement under the influence of the torque of an external magnetic field using the lever principle with minimal forces (Figure 5. G) [175].

2.2.3.3 Stimulus Target

Thermo- and mechano-sensitive channels serve as promising targets for controlling neural activity. Thermosensitive channels respond to temperature changes, while mechanosensitive channels react to mechanical forces, by opening the gate and allowing for selective passage of ions thus modulating neuronal depolarization.

The activation of thermosensitive channels is related to certain temperature thresholds or temperature changes [176]. Transient Receptor Potential (TRP) superfamily contains many thermosensitive channels. TRPV1 is a common non-selective cation channel used in magneto-thermal stimulation. This channel responds to a temperature above the threshold of around 41°C and is expressed in mammals, mostly in the peripheral nervous system [176-178]. Another common TRP member, TRP member of vanilloid family 4, TRPV4 is also a thermosensitive channel responding to a warm temperature located above 30°C, however, due to its polymodality, it is also actively responding to mechanical stimuli [179-181]. Similar multimodal channels that respond to several stimuli are TREK 1, TREK2, and TRAAK, which can respond to temperatures above physiological, but with little mechanical sensitivity [182]. While the majority of magnetothermal neurostimulation approaches so far relied on targeting the TRPV1 channel demonstrating kinetics on the temporal scale of seconds, more recent studies demonstrate sub-second control of neuronal activation and even silencing when MNPs are targeted to ion channels activated by sudden change in the temperature such as transient receptor potential ankyrin member 1 (TRPA1) and potassium channel TREK1. Since the latter are sensitive to temperature gradient instead of a temperature threshold, their response to temperature stimuli is faster compared to TRPV1 [182-184], they demonstrate targets for neurostimulation technology with high spatial and temporal resolution [60, 61].

The mechanosensitive ion channels can transform mechanical signals into electrical or chemical signals [176]. PIEZO1 and PIEZO2 were described as the first mechano-specific Ca^{2+} permeable mammalian receptors in 2010, with important roles in touch perception, proprioception, and noxious mechanical stimuli [53, 185-187]. They have a special three-bladed structure, and they deform with the curvature of the membrane, which leads to channel opening, placing them among favorable targets for mechanical stimulation [187-190]. TRPV4 is expressed in various tissues and therefore is a common target for magneto-mechanical

modulation [179, 185, 191-193]. As mentioned before, TRPV4 is however also sensitive to other stimuli, including thermal and chemical signals which may cause plasticity of its mechanical response *in vivo* [179]. TREK-1 and TRAAK can also respond to mechanical stimuli, but their response is stronger to other stimuli [52, 147, 179, 185, 191-196]. Additionally, there are anionic channels such as cystic fibrosis transmembrane conductance regulator CFTR, which has the potential for mechanical neuronal inhibition [197, 198].

2.2.3.4 Coil Design

There are few special designs of the coil for nano-invasive neurostimulation technologies. The existing ideas include mini-solenoids [49, 50, 199, 200], large solenoids [201, 202], and Helmholtz coil(s) [203]. Some research also generates changing magnetic fields by rotating magnets [204]. Most of these designs put tissue or animals under or surrounded by the coil, so the experiments are constrained by the size of the coils. Besides, to account for the field attenuation due to distance, a large current is required to increase the electric field in the region of interest. This also brings unneglectable heat generation, some even need water cooling [152], which is not energy efficient. Therefore, the design of the coil has not received enough attention in this method. Applying microelectronics to nano-invasive magnetic neurostimulation will be an effective improvement to current research. Millimeter-scale mini-coil array can break the space limitation of experiments by making stimulation devices wearable and moveable and increase energy efficiency by reducing the energy loss in large coils from field attenuation, which are crucial for stable chronic further nano-invasive magnetic neurostimulation [205].

Table 3. Publications over time on neurostimulation using MNPs.

Year	Type of Stimulus	Material	Particle size	Shape	Channel	External magnetic source	Ref
2010	Thermal	$MnFe_2O_4$	6 nm	Nano-disc	TRPV-1	Solenoid (25 turns, d=7 mm)	[49]
2014	Mechanical	$Zn_{0.4}Fe_{2.6}O_4$	<50nm	Cube	-	Solenoid (with core, d=1 mm)	[50]
2015	Thermal	Fe_3O_4	22 nm	Spherical	TRPV-1	Solenoid (with C-shape core, d=4 cm)	[23]
2017	Thermal	Co-ferrite core at Mn-ferrite shell	15.65 nm	Core-shell	TRPV-1	Solenoid	[152]
2020	Mechanical	Fe_3O_4	98−226 nm	Nano-disc	TRPV-4	Solenoid (with core, d=20 cm)	[57]
2021	Thermal	Iron oxide	<25 nm	-	TRPV-1	Solenoid	[59]
2021	Mechanical	Iron oxide	25 nm	500nm spherical cluster with nano-octahedral	PIEZO-1	Magnets placed on a circular path with d=20 cm	[204]
2021	Mechanical	Fe_3O_4	100nm	-	TRPV-4	Magnets	[206]
2021	Mechanical	collagen coated Fe_3O_4	100nm-10μm	cluster	-	Solenoid (with core, 1035turns d=20 mm)	[199]
2022	Thermal	Iron oxide	19nm	-	TRPV-1	Solenoid (with core)	[60]
2022	Mechanical	Fe_3O_4	212.4nm, 280.0nm	Nano-disc	TRPC family	Solenoid (2000 turns, d=20 mm)	[200]
2023	Thermal	g-Fe_2O_3 core at dextran shell	25nm	Core-shell	TRPV-1	Solenoid (17 turns, d=5 cm)	[207]
2024	Thermal	$CoFe_2O_4$ at $MnFe_3O_4$	14nm	Core-shell	TREK1	Solenoid	[61]

2.2.4 Comparison of Magnetic Neurostimulation Technologies

The previous sections have provided a comprehensive overview of the three magnetic neurostimulation methods. In principle, non-invasive and invasive methods are based on induced electric fields, while nano-invasive methods involve the movement or heating of nanoparticles. The spatial resolution and performance of DBS of invasive and nano-invasive

methods are significantly better than that of non-invasive methods. However, invasive, and nano-invasive methods require invasiveness. Although the nano-invasive method is less invasive, it is also the only method that requires genetic engineering.

Table 4. Comparison between three magnetic neurostimulation methods.

Property	Non-invasive	Invasive	Nano-invasive
Principle	Stimulate by magnetic field induced electric field	Stimulate by magnetic field induced electric field	Stimulate by movement or heating of nanoparticles
Spatial Resolution	Tens of cm	Hundreds of μm	Specific neuron(s)
Invasiveness	No	Yes	Yes (MNPs)
Genetic Engineering	No	No	Yes*
Deep Brain Stimulation Accuracy	Low	High	High
Coil Size	Centimeter	Sub-millimeter	Millimeter to centimeter

* Transgene-free methods for PNS stimulation are available. Transgene-free methods for CNS reported [61].

2.3 Microfabrication Technologies for Magnetic Neurostimulation

Building on previous sections discussing next-generation magnetic stimulation and the importance of mini/micro-coils, this section explores state-of-the-art microfabrication techniques for coil miniaturization. Each technique is analyzed in terms of its fundamental principles, compatible materials, and applications in micro-coil fabrication. Although some of these technologies have not yet been applied in neurostimulation, particularly in nano-invasive approaches, they show significant promise for future applications, especially in targeted modulation scenarios.

2.3.1 Through-Silicon Vias

Through-Silicon Vias (TSV) technology employs high-aspect-ratio etching and deposition techniques to fabricate openings ranging from sub-micrometer to several hundred micrometers in scale [208]. This method enables efficient access and modulation of high-density coils integrated on the same substrate. The TSV process begins by creating vias in Silicon (Si) or glass substrates. These vias are subsequently filled with conductive materials, including doped polysilicon, low-resistivity monocrystalline Si, tungsten, or copper (Cu) [209-212].

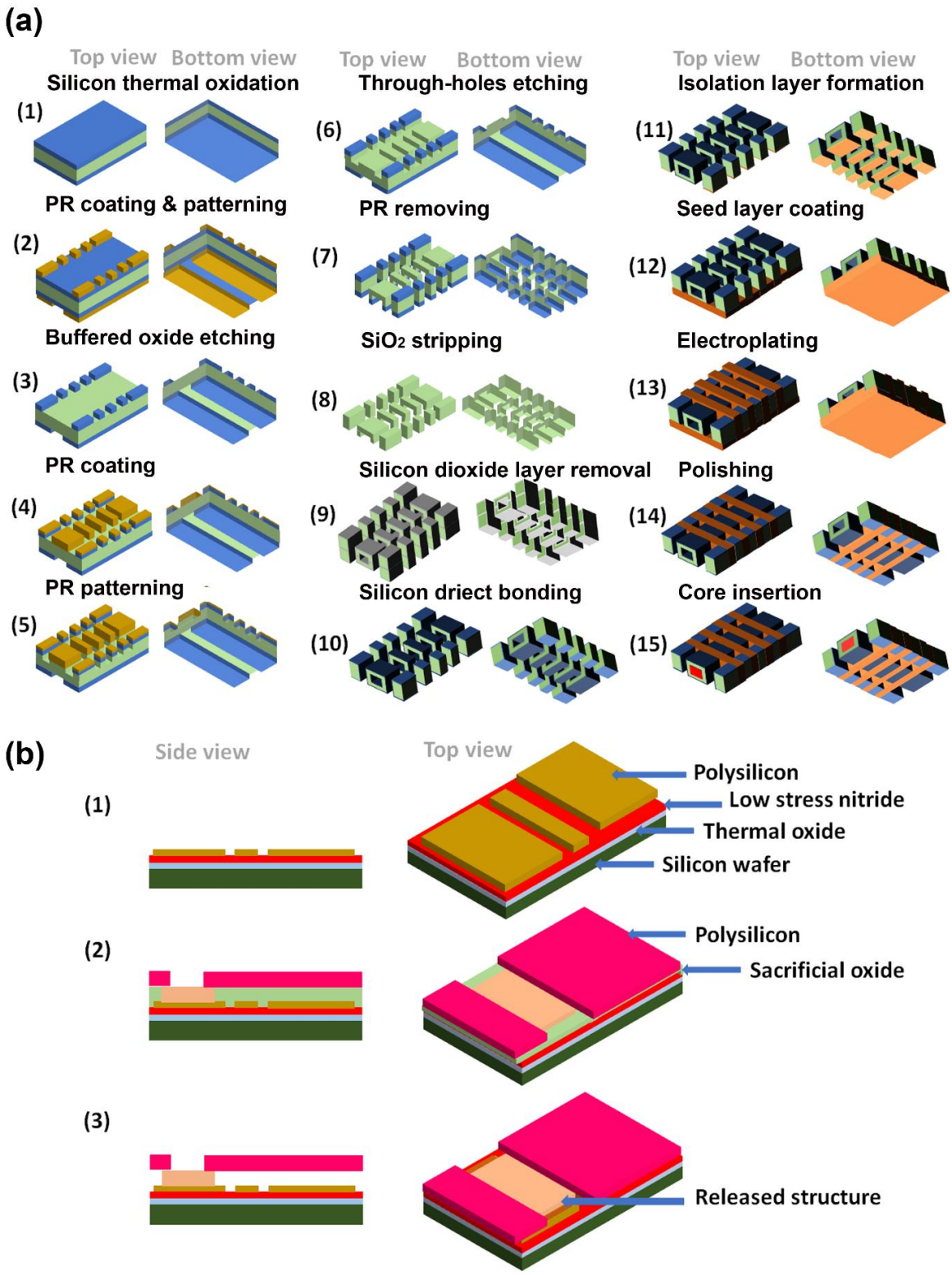

Figure 6. (**a**) schematic of TSV process for micro-coils [213]. (**b**) schematic of the fabrication process of a surface micromachined constructs [214].

An example of micro-coil made by this method is shown in Figure 6. A (not to scale). In the first stage, coil and core geometries are defined within a double-side-polished silicon (Si) substrate. The core is then sealed within the substrate using Si direct bonding. In the second stage, Cu coils are formed via electroplating. A thick oxide layer is grown for insulation, followed by seed layer deposition and 'bottom-up' filling of the trenches and vias. Excess Cu

is removed by grinding, and the inductors are separated by dicing. Finally, an iron core is inserted into each coil to complete fabrication [213]. The fabricated coil have a height of 1 mm, square Cu coils with 100 μm sides, and 100 μm gaps between the coils [213].
heavily rely on hazardous materials and chemicals [215]. Within these methodologies, a

2.3.2 Surface Micromachining

Surface micromachining involves fabricating structures layer-by-layer through the deposition of thin films on substrates as functional compounds [216]. This technique is commonly used in producing micro-coils with high precision in a clean-room-compatible micro/nano-scale range. It comprises of deposition of thin films and sacrificial layers, photolithography, and etching steps [217-219]. Silicon is a common choice as a substrate due to its compatibility with microfabrication processes, but other materials such as glass also have been utilized [220, 221] The deposition of thin films onto the substrate is performed through techniques like chemical or physical vapor deposition with selected materials [222]. Sacrificial layers are temporarily deposited and subsequently removed to release the final microstructure, which is deposited between the coil windings [223]. Following thin film deposition, a photoresist is patterned to define the intended structure after which the sacrificial layer is etched away via wet or dry etching [217-219, 222, 224, 225]. Figure 6. b (not to scale) outlines an example of surface micromachining process on a Si substrate. The process starts with thermal oxidation (0.6 μm), Si nitride deposition (0.8 μm), and patterning of phosphorous-doped polysilicon. A 2 μm sacrificial oxide layer is then deposited, followed by structural polySi deposition (0.8 μm), patterning, and annealing. Finally, the sacrificial oxide is etched with hydrofluoric acid, releasing the microstructures from the substrate. The final resonator has dimensions of approximately 200 μm × 200 μm × 1 μm [214].

2.3.3 3D Micro/Nano-fabrication Methods

The drive towards creating 3D structures through additive manufacturing processes has been instigated by the need for high-resolution, eco-friendly fabrication techniques that do not variety of techniques such as lithography, direct writing, and 3D printing have been employed to manufacture a spectrum of 3D nanostructures [226, 227].

2.3.3.1 Two-Photon Polymerization

Lithography is a methodology employed for creating structures at the nanoscale or microscale. By exposing the photoresist under a source of light going through a mask with the desired pattern [228]. The pattern size is limited to the exposure wavelength and sub-micrometer features are developed via electron-beam lithography. The substrate undergoes a coating

process with single or multiple layers of functional compounds serving as a hard mask, dielectric, or conducting layer [229]. Resists are commonly categorized as negative or positive and amplified or nonamplified resists including polymethylmethacrylate, SU-8, and novolac-epoxy resin [230, 231]. Besides, there is the use of composite materials, combining gold (Au) and silver (Ag) salts with photoresists for metal deposition [232]. In general, lithography processes form a pattern in the resist, followed by the pattern transfer to the substrate through processes such as lift-off or etching [225].

For precise micropatterning on a substrate surface, various lithography techniques are deemed effective, including photolithography, X-ray lithography, and two-photon polymerization (TPP) [225, 229, 233]. TPP provides superior process flexibility and resolution, enabling the fabrication of constructs with dimensions smaller than 100 nm [234]. Another advantage of employing TPP is its capability to print within the resin, extending beyond surface limitations. However, due to its reliance on a focused laser beam and a spot scanning approach, TPP exhibits a lower processing speed when compared to other lithography methods [235]. The schematic of the TPP system is shown in Figure 7. abelow. A multi-turn 3D micro-coil, with a diameter and height of 200 μm, and 60 μm was successfully fabricated through this method [236]. However, the drawback of this method lies in the necessity for an expensive and large synchrotron radiation facility to serve as the light source.

2.3.3.2 Focused Electron Beam-Induced Deposition

Focused electron beam-induced deposition (FEBID) is a direct-writing approach that exploits the direct deposition of structures on the surface of a substrate by scanning a focused electron beam across the desired pattern of the construct in the presence of a precursor gas. Typically performed within electron microscopes, this method facilitates easy in-situ inspection of the manufactured construct [237, 238]. Considering the focus-ability of electron beams in the range of micrometers to sub-angstrom, this process is appropriate for applications in both the micro- and nanometer scales [239].

In FEBID, precursors are delivered through a capillary tube to provide a continuous supply of molecules in gaseous form to the surface. A portion of the incoming flux is then chemo- or physio-sorbed on the surface of the substrate [240]. The precursor molecules dissociation can occur due to the interaction of backscattered, secondary, and primary electrons with the adsorbed molecules on the surface [237, 241]. Typically, the precursors are complexes comprising ligands and a metal core named organometallic precursors, where the selection of the precursor type primarily determines the composition of the deposited compound [237,

242]. FEBID can deposit superconducting alloys, metallic materials, metamaterials, and intermetallic compounds, including Au, Ag, tungsten, iron, ferro-cobalt alloys, cobalt, and platinum (Pt) [237, 242]. The Schematic diagram of FEBID is shown in Figure 7. bbelow. FEBID has the capability of depositing materials on non-flat substrates and is geometrically intricate [238] and has been successfully employed to deposit magnetic nanowires demonstrating the potential of FEBID in tailoring nanoscale coil for specialized applications [243-245]. However, for neurostimulation applications, a restrictive factor is the need for high throughput FEBID with higher functioning speed as current systems operate at a speed of tens of nanometers per second. This especially is observed as a critical factor in tall constructs and long parts where a significant reduction in growth rates has occurred [237, 246, 247].

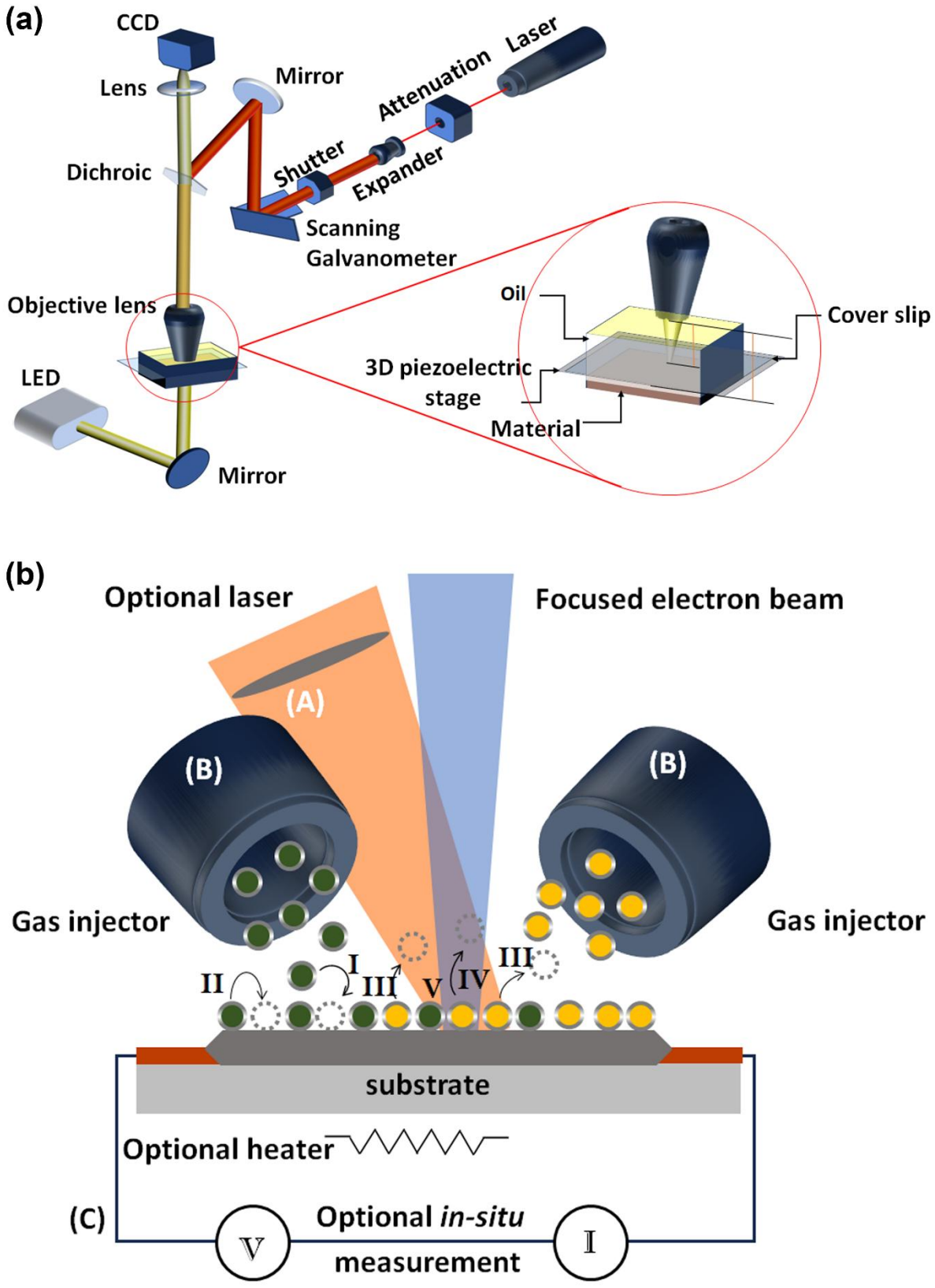

Figure 7. Schematic of a (**a**) two-photon polymerization schematic system setup [233] and (**b**) scanning electron microscopy adapted for focused electron beam-induced deposition [242].

2.3.4 Micro-coils Printing

As already mentioned, the conventional approach for producing micro-coils is both costly and time-consuming. Nevertheless, there are highly rapid, consistent, and cost-effective methods for manufacturing micro-coils through additive manufacturing techniques also known as digital writing and direct printing [248]. These processes such as screen printing, inkjet printing, electrohydrodynamic printing, and aerosol jet printing are utilized to create parts with precise control over their composition and architecture for a wide range of applications at both the macro- and micro-scale [249-252].

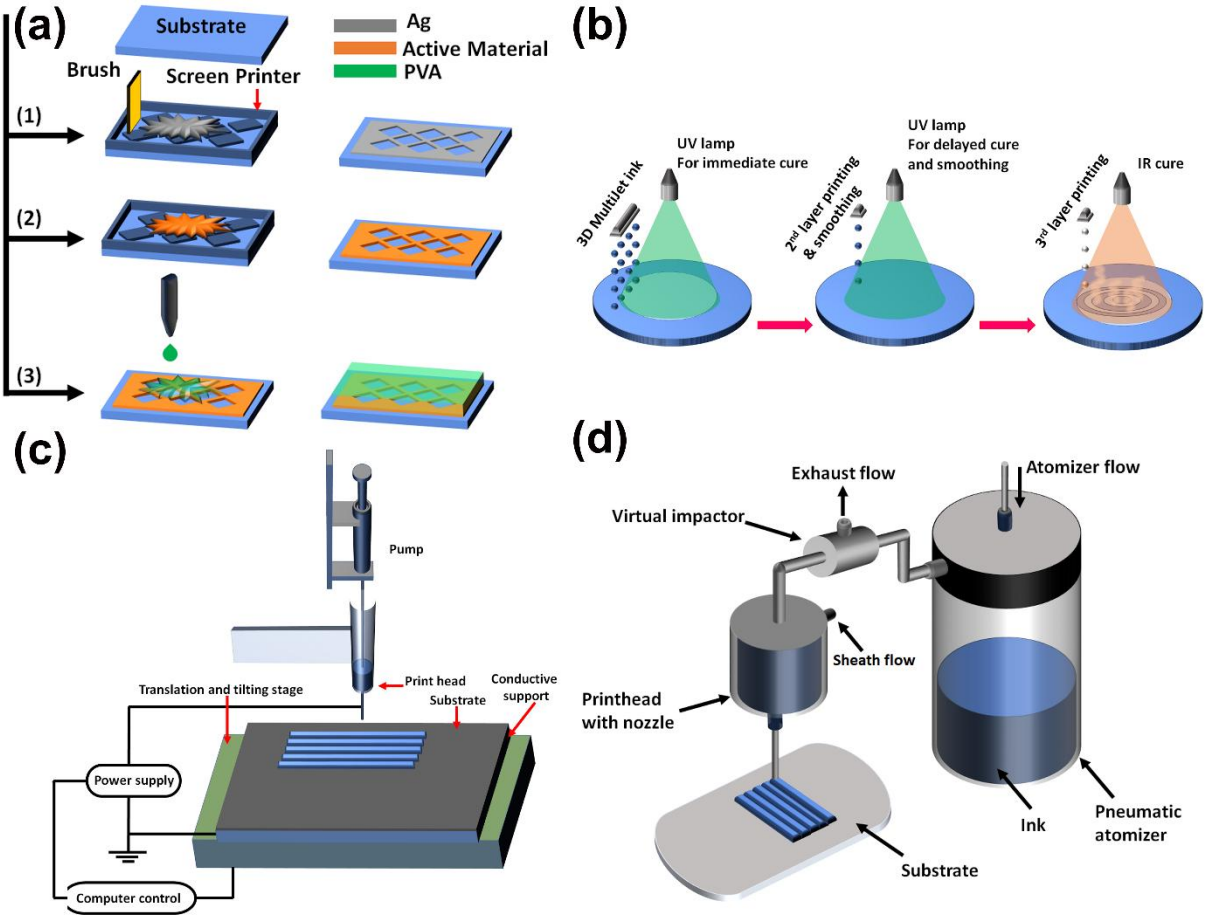

Figure 8. Schematic presentation of (**a**) screen printing, (**b**) inkjet printing [253], (**c**) electrohydrodynamic printing [254], and (**d**) aerosol jet printing [255].

2.3.4.1 Screen Printing

Screen printing can print a desired design on a flat surface using a squeegee, ink, and a mesh screen [256, 257]. The fundamental process forms a stencil on a fine mesh screen and subsequently uses a squeegee to paint, thereby generating an imprint of the design on the underlying substrate. It can be utilized on surfaces of any size and shape, including eyeglasses, inner surfaces, or windshields, distinguishing it from inkjet technologies [256]. The fabrication of micro-coils via screen printing involves three key steps, as depicted in Figure 8.

a: electrode printing, active material printing, and electrolyte deposition. Initially, electrodes (e.g., Ag) are screen-printed onto a bare substrate such as polyethylene terephthalate, followed by drying and annealing in a vacuum oven. Subsequently, the active material ink (e.g., MnO_2/onion-like carbon) is printed atop the Ag electrodes and dried. Lastly, an electrolyte sol such as polyvinyl alcohol /H_3PO_4 is coated over the device to encapsulate the channel area and then air-dried to complete the fabrication process [257]. Employing this method, a micro-inductor with a low profile was created on a substrate of copper-cladded polyimide. The coils carrying the current were designed from the pre-existing metallization layer, and using a composite of ferrite-polymer the magnetic core was printed [249]. A study investigated the viability of graphene nanoplatelet-printed electrodes for cortical direct current stimulation, comparing them to traditional Ag/silver chloride pellet electrodes [258]. The study found that while silver-based electrodes pose a risk to living tissue due to redox reactions caused by partial permeability of the printed layers, graphene nanoplatelet-based electrodes are electrochemically safe for direct neural stimulation [258].

2.3.4.2 3D Inkjet Printing

3D inkjet printing is a process that operates at low pressures and temperatures, involving the laying down of either suspension of solid or liquid substances such as dielectric nanoparticles, polymers, and conductive nanoparticles. In this technique, the printing compounds are extruded via a nozzle, while the print head moves back and forth across a surface in a raster pattern, constructing multiple layers one after the other in a sequential layering process, which is shown in Figure 8. b. The primary methods of inkjet printing include drop-on-demand mode and continuous inkjet mode [246, 247, 253, 259]. Drop-on-demand printing is recognized for its capability in the fabrication of constructs composed of multi-materials, due to its technological flexibility in dynamically adjusting to various materials and patterns. This is in contrast to other manufacturing and printing processes, which typically necessitate fixed tooling or masks [260]. While this printing method stands out as scalable, non-contact, and less prone to issues like contamination and damage to masks or substrates, the achievable resolution and range of possible shapes in fabrication were restricted [261]. For instance, this method has been used to print a flexible micro-inductive coil composed of Cu on a paper substrate [250]. In another study, a combination of electroplating and printing methods was used to fabricate a 16-turn solenoid on microcapillaries, measuring 1.6 mm in length and 324 μm in diameter, which exhibited a high spectral resolution, characterized by a narrow linewidth of merely 0.9 μm [262]. Additionally, researchers developed an ultra-small neural stimulating implant (~0.009 mm^3) using inkjet printing and 130 nm CMOS technology [263]. This fully encapsulated microbead, measuring 200 μm × 200 μm × 80 μm, integrates wireless

powering, microelectronics, electrodes, and a coil. Minimally invasive implantation into the sciatic nerve of a rat model demonstrated successful elicitation of compound action potentials, validating the implant's functionality for potential central nervous system applications. Additionally, a recording microbead with wireless powering and backscattering telemetry was investigated, showcasing the versatility of this technology for future neural interfaces [263].

2.3.4.3 Electrohydrodynamic Printing

Compared to inkjet printing, electrohydrodynamic printing offers a higher resolution [264], which is attained by using a droplet formation approach involving the usage of an electric field between the substrate and miniature nozzles, typically with inner diameters ranging from about 100 nm to several micrometers [254, 265]. In this process, the ink is transported to the nozzle, and the application of an electric field causes a buildup of mobile ions at the nozzle tip on the ink's surface. This results in electromagnetic 'Maxwell' stresses at the nozzle tip, leading to the formation of a Taylor cone. When the electric field reaches a certain threshold, the stresses at the nozzle tip can surpass the opposing capillary stresses. Based on the electrical characteristics of the ink this can result in the ejection from the nozzle as a fine jet or droplets, also known as electrohydrodynamic jet printing or electrohydrodynamic nano-drip printing, respectively [254, 266], like presented in Figure 8. c. It has been shown that these methods have the capability of printing various materials with a precision of nanometer on both structured and flat substrates such as colloidal quantum dots [267], nanoparticles [268], Ag and Au [269], and polymers [270]. To demonstrate the feasibility of electrohydrodynamic printing for coil fabrication, a spiral-type inductor was printed [271]. The printed inductor, exhibiting an inductance of 9.45 μH, displayed approximately fivefold higher resistivity compared to bulk Ag following sintering. This method also has been employed to print a silver-based spiral inductor with micrometer resolution [251]. Thus, the electrohydrodynamic printing technique offers a promising avenue for fabricating microscale electronic devices, primarily due to its capability to produce high-resolution features and its versatility in accommodating a wide variety of functional inks [272]. As further evidence of the potential of this technology, researchers have demonstrated the successful printing of various passive electrical components, including capacitors, resistors, and inductors, with a minimum feature size of approximately 60 μm, achieved using a 110 μm nozzle [251]. This highlights the potential of electrohydrodynamic printing for the fabrication of complex electronic devices [273]. While it has been demonstrated that inks with a range of electrical conductivities can be printed using this method, the necessity for an electric field imposes certain limitations on the process concerning the characteristics of the ink and substrate compatibility [274]. For example, using a DC voltage the initiation and cessation of liquid

jetting cannot be precisely controlled. Additionally, when a pulse voltage is employed there exists a nonlinear relationship between the frequency of droplet deposition and applied voltage. Both scenarios affect the fine resolution of the printed structures [275].

2.3.4.4 Aerosol jet printing

Aerosol jet printing provides an enhanced line resolution, achieving widths as fine as 10 μm, which is an improvement over the capabilities of inkjet printing [276]. In this method, an ink containing the desired nanoparticles is subjected to ultrasonic atomization, creating a dense slurry of ink droplets with diameters ranging approximately from 1 to 5 μm. The size of the droplets in this process is dependent on the atomizer frequency [255, 277]. As Figure 8. d shows, an inert gas is used to carry the aerosolized droplets from the reservoir of the ink to the printhead. Within the printhead, a sheath gas stream collimates and speeds up the flow of microdroplets in a tapered nozzle. This action induces aerodynamic focusing, forming a precise jet that affects the substrate surface [277]. The independence of the deposition to the direction and ample spacing between the substrate and printer tip enable consistent material deposition on uneven and irregular surfaces, making it ideal for printing on non-planar substrates conformally [278, 279]. As a preliminary step towards realizing the potential of aerosol jet printing for micro-coil array fabrication, Ag nanoparticle-based human-sized coils were successfully prototyped using this technology [252].

These reproducibly fabricated coils demonstrated a diameter of 1800 μm, trace width and spacing of 112.5 μm, a thickness of 12 μm, and an inductance value of approximately 15.5 nH [252]. Another attempt focused on the process and characterization of printed inductors of polymer-matrix magnetic nanocomposites, comprising nickel-zinc ferrite ($Ni_{0.5}Zn_{0.5}Fe_2O_4$) nanoparticles in a polyimide matrix using multi-material aerosol jet printing. The results showed a 40% increase in inductance density in 1-mm², 4.5-turn microstrip spiral inductors printed with the composite, achieving an inductance density of 4.2 nH/mm² [280]. In a demonstration of aerosol-jet printing's versatility, high-frequency, tapered-solenoid inductors with wide bandwidth capabilities were successfully fabricated [281]. The design strategically incorporated a polymer support structure to minimize parasitic capacitance, a tapered solid core, and conductive windings. Two variants were produced, one featuring a printed polymer core and the other utilizing a non-printed iron core. Scattering parameter analysis confirmed that the polymer-core inductor achieved a usable bandwidth of up to 18 GHz, while the iron-core inductor extended to 40 GHz, both maintaining low insertion loss [281]. Additionally, researchers demonstrated the fabrication of a coreless flyback transformer using aerosol jet printing and electrodeposition techniques [282]. A two-layer secondary inductor was built on

top of a two-layer primary inductor, separated by UV-curable dielectric polymer layers. The transformer achieved a gain of 75.3x, converting a 17 V, 400 kHz input into a 1250 V output. Additionally, the study showcased the successful fabrication of 8-layer stacked inductors with low equivalent series resistance (0.6 Ω) and 1.7 μH inductance at 100 kHz [282]. However, despite the capability to deposit various kinds of inks, setting the optimal printing boundaries is often challenging. For example, the rheology of the employed ink is a crucial factor in this technique, determining the jet-ability of the ink and affecting the printing quality [283]. Achieving reproducibility and consistency is another challenge, often necessitating rigorous steps like ink replacement several times during the process, which can impede the scalability of the production [284-286].

2.3.5 Summary and Comparison of Microfabrication Technologies

In conclusion, the parameters, advantages, and limitations of diverse fabrication methods explored to produce coils for magnetic neurostimulation is shown in Table 5. Overall, the choice of fabrication method depends on the specific requirements of the neurostimulation application, balancing factors such as coil size, geometry, performance, and cost.

Table 5. Summary of the characteristics and comparison of microfabrication technologies.

Fabrication method	Geometry	Physical dimensions	Key characteristics	Limitations	Ref.
Through-Substrate Vias	Spiral/ Toroidal solenoid	100s nm to 100s μm	High aspect ratio/ free of voids/ substrate isolation by suspended windings.	Fragile coils/ complex process	[208-212, 287-296]
2D/3D micromachining	Spiral/ Toroidal/ Racetrack solenoid/ planar coils	100 nm to 100s μm	High precision/ CMOS compatible	Low quality factor (2D)/ eddy currents/ complex process (3D)	[297-301]
Lithography/ Two-photon polymerization	Micro-probes/ planar coils	10s nm to 100 μm	High precision	Wavelength limitation to size/ low processing speed	[234, 302-305]
Focused electron beam-induced deposition	Helical nanostructure	Sub-Å to 10s nm	High resolution/ direct deposition/ in-situ inspection/ compatible with non-flat substrates/ 3D structure efficient patterning	Low throughput/ conductive material limitation/ slow speed	[237, 239, 242, 246, 247, 306]
Screen printing	Micro-electrode	50-100 μm to large	Simple/ scalable/ cost-effective	Lowe resolution	[257, 307]
Inkjet printing	Solenoid/ Implantable micro-probes	20 to 100s μm	Low pressure and temperature/ multi-material capability/ technological flexibility/ scalable	Limited resolution and shape range	[261-263, 308]
Electrohydrodynamic printing	Spiral solenoid	100 nm to 1-10 μm	High resolution/ multi-material compatibility/ compatible with non-planar substrates	Challenges in parameter optimization/ reproducibility/ consistency/ ink, substrate compatibility	[271, 274]
Aerosol jet printing	Spiral solenoid	10 μm to several 100s of μm	High resolution/ versatile material compatibility/ conformal printing on non-planar substrates	Challenges in parameter optimization/ reproducibility/ consistency	[252, 276, 281, 283, 309-311]

2.4 Literature Review Summary

2.4.1 Non-invasive magnetic stimulation

The non-invasive method relies on Faraday's law to transmit stimulation signals by modulating magnetic fields. TMS stands as one of the earliest magnetic neurostimulation techniques and has thus matured into a well-established and widely used method. It benefits from extensive clinical experience. The primary advantage of TMS is its "non-invasive" nature, eliminating the risks associated with implantation, such as immune responses.

However, the non-invasive feature of TMS also poses certain challenges. Firstly, its focality has historically been less precise, although this has improved over time with the development of advanced coil designs, as discussed earlier. Secondly, TMS struggles to deliver robust stimulation to deep brain regions. Although the introduction of the H-coil has mitigated this limitation to some extent, DBS remains challenging for TMS. Thirdly, TMS applies stimulation to the entire head, making it difficult to achieve precise targeting of specific neurons or lesions. This results in lower selectivity and resolution. Consequently, TMS cannot provide highly accurate neurostimulation, and despite advancements in brain mapping, a definitive solution to this issue remains elusive.

The potential of TMS appears to be reaching a stable stage. While ongoing research in brain mapping and stimulation waveforms continues to yield incremental progress for TMS, it is unlikely to bring about fundamental changes in the technology. Although coil design remains a potential avenue for improvement, the pace of innovation in this regard has been slowing down. It is challenging to make precise predictions of TMS. However, it's essential to acknowledge that TMS has amassed a wealth of technical experience in coil design and a substantial clinical database. These resources can be leveraged in the development of next-generation magnetic neurostimulation techniques, such as nano-invasive magnetic neurostimulation coil designs. The convergence of this accumulated knowledge with emerging technologies may lead to breakthroughs in the field of magnetic neurostimulation.

2.4.2 Invasive magnetic neurostimulation

The invasive application of Faraday's law at a micro-scale represents the primary approach of μMS. Its proximity to the targeted lesion significantly enhances stimulation resolution, enabling the feasibility of magnetic DBS. The induced electric field in μMS is both computable and more controllable. When combined with μMS's spatial selectivity, it allows

for highly precise stimulation, particularly when targeting neurons with distinct spatial distributions. Additionally, μMS is advantageous due to its relatively low current requirements for stimulation, contributing to improved power efficiency. These features collectively position μMS as a promising technique for highly accurate and localized neural stimulation, particularly in scenarios demanding precise spatial targeting and chronic implantation.

A notable drawback of it is invasiveness, which might bring extra risks from surgery or inflammation. However, μMS, compared with other invasive methods as a magnetic neurostimulation approach, the coil does not contact tissue directly. The micro-coil, if encapsulated within biocompatible materials, can serve a dual purpose: protecting surrounding tissue from potential immune responses and other implant-related side effects while safeguarding the coil from degradation due to the tissue environment. This encapsulation supports the utilization of certain non-biocompatible materials in the fabrication of the coil.

μMS exhibits remarkable qualities such as precision, selectivity, compactness, low power requirements, and the potential for chronic implantation. In the short term, its high precision and selectivity for neurostimulation make it a valuable tool for advancing neuroscience research. This research experience can further inform and refine its applications. Looking to the long term, the additional attributes of μMS align well with the characteristics of mobile medical devices. Consequently, μMS could serve as a method for neurostimulation in telemedicine or at-home medical settings. However, it is essential to acknowledge that this technological avenue is still in its early stages and lacks extensive clinical experience. As an invasive technology, to realize its potential, concerted efforts should focus on *in vivo* testing to assess the safety and efficacy of invasive neurostimulation therapy. Additionally, system integration plays a pivotal role in bridging the gap between this emerging technology and its practical application in individuals' homes.

2.4.3 Nano-invasive magnetic neurostimulation

The nano-invasive method harnesses magnetic fields to manipulate nanoparticles for neurostimulation, representing a delicate balance between invasive and non-invasive approaches. The absence of mechanical implantation like what μMS does, which will significantly reduce the risk of side effects brought by implantation, and its high stimulation selectivity derived from specific ligand-receptor interactions can ensure accurate selection of

stimulation target or stimulation mode (activation or inhibition). Moreover, the biomolecules (ion channels) associated with thermal and mechanical methods are more widely distributed within humans, mitigating ethical concerns associated with genetic modifications.

These compelling advantages come at a cost: the process is marked by the complexity of particle coating and delivery to the targeted tissue. Achieving the requisite level of selectivity necessitates a meticulously designed particle coating to enable specific binding to receptors. However, the applications of MNPs in other areas like cancer treatment have accumulated rich experience for nano-invasive magnetic neurostimulation, which aids in the translation of this neurostimulation approach.

At present, the challenges in the field of nanoparticle-based neurostimulation include addressing the issues related to targeting and delivery of nanoparticles, for example, crossing the blood-brain barrier. One of the most significant gaps between the technology and practical application lies in the lack of suitable coils. It is imperative to design the miniaturized and wearable coil specifically for nano-invasive magnetic neurostimulation. Although, like μMS, clinical application is still not performed, with more *in-vitro*/*in-vivo* experiments and further suitable coil designs, this technology has the potential to lead the next-generation magnetic neurostimulation.

2.4.4 Project Strategies

Based on the review findings, the project strategy should adopt distinct approaches for these two next-generation stimulation technologies, as their respective coil development stages are markedly different. For invasive stimulation technology, the field has advanced to the point where various functionally specialized coils are already in production. Therefore, the focus will shift toward selecting specific coil paradigms for optimization and performance enhancement. Key aspects will include improving stimulation efficiency, spatial precision, and biocompatibility of existing designs. In contrast, nano-invasive stimulation technology remains at an earlier developmental phase, where research is still primarily exploring differently sized solenoids. Consequently, the priority here lies in testing diverse coil configurations to identify the most effective design before optimization can begin. This phase will involve systematic evaluation of electromagnetic performance, miniaturization feasibility, and ergonomic compatibility at.

3 Probe micro-Coil Optimization for Invasive Magnetic Stimulation (Micro-Magnetic Stimulation)

This Chapter highlights the selective invasive magnetic stimulation capabilities of probe micro-coil. The analysis will focus on three key factors:

1) The fundamental mechanisms of spatial selectivity of probe micro-coils.
2) Potential design innovations to probe micro-coil configurations.
3) The cleanroom-based fabrication process optimization and evaluation.

3.1 Introduction

As discussed in the literature review, invasive magnetic stimulation enables high-precision targeting of deep brain regions using miniaturized, implantable coils. Notably, Section 2.2.2.1.3 introduces a particularly innovative coil design, the probe micro-coil, which has the potential to achieve spatially selective neural activation, thereby further enhancing the accuracy of micromagnetic stimulation. These micrometer scale coils, encapsulated with biocompatible materials, depart from conventional spiral or multi-turn designs. Instead, they utilize intricate geometries (e.g., V-shaped, W-shaped, or semicircular designs; Figure 9. C) to generate specific magnetic field distributions which can activate axons in one direction while keep the axons in orthogonal direction inactivated [22, 41, 128, 129]. This unique characteristic renders the investigation of the underlying selectivity mechanisms and the optimization of coil geometry a compelling avenue for future research.

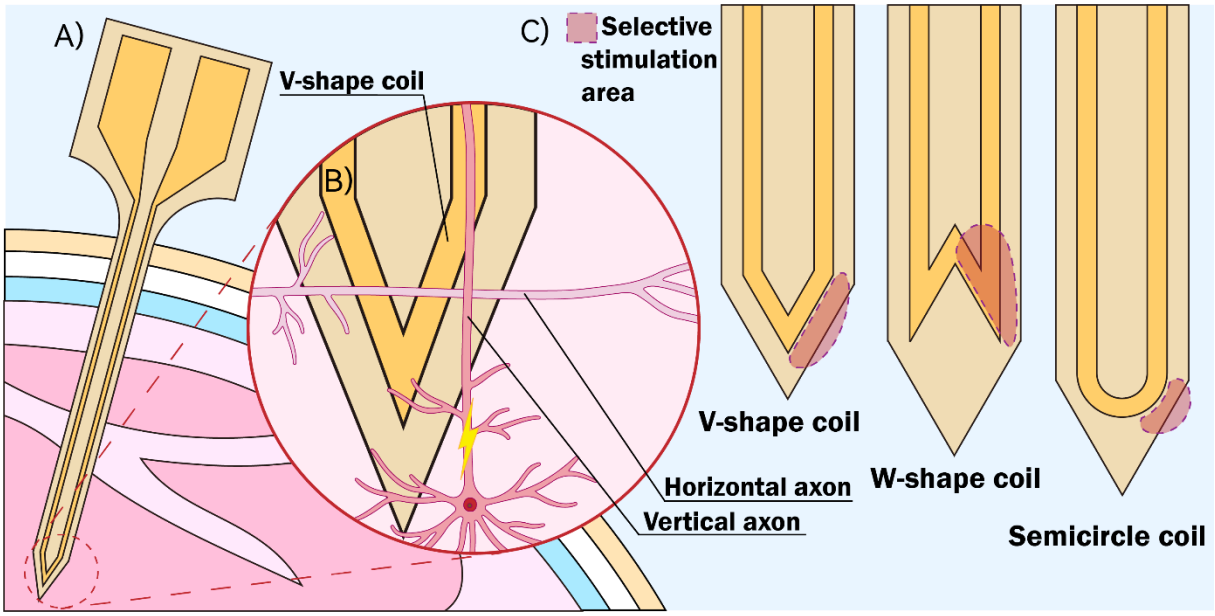

Figure 9. **A**) Probe micro-coil implanted in the brain. **B**) Zoomed-in view of the probe tip area, showing selective stimulation of vertical axons. **C**) Example designs of probe micro-coils and their corresponding selective stimulation regions.

3.2 Explore on Mechanisms of Spatial Selectivity

3.2.1 Mainstream Theory

Studies have demonstrated that micro-solenoids selectively activate neurons aligned parallel to the coil wire while sparing those in transverse orientations (Figure 9. B) [37, 39, 109, 115]. This phenomenon aligns with 20th-century findings demonstrating that parallel electric field gradients exert a stronger excitatory effect on axons than perpendicular fields [312, 313]. It has been tested that this fundamental principle extends to probe micro-coil configurations as well [41]. This geometric modification represents a promising approach for enhancing the spatial precision of μMS.

Neuronal activation requires suprathreshold stimuli capable of eliciting action potentials. The probe micro-coil design was developed based on the neural activation hypothesis proposed in [314], which establishes the electric field gradient (with a threshold exceeding 11 V/m²) as the primary driver of axonal excitation. This theoretical framework has been claimed to be substantiated through both computational modeling and experimental studies, demonstrating that incorporating an oblique segment in coil geometry induces field asymmetry along orthogonal axes, thereby bringing spatial selectivity [22].

Specifically, [22] revealed that the selective activation capacity of micro-coils stems from asymmetric electric field distributions between orthogonal directions. The study introduced innovative V-shaped and W-shaped coil configurations (Figure 9. C), demonstrating that oblique wire segments produce controlled field gradient imbalances between horizontal and vertical orientations. The angle of obliquity was found to correlate with how asymmetric the field will be: the more oblique, the more asymmetric.

3.2.2 Skepticism towards the Theory

Despite *in vitro* evidence supporting this selective activation principle, the theoretical basis of this mechanism has faced growing questioning. There are three main points:

1) Attempts to replicate the original simulations revealed minimal or absent field asymmetries, contradicting the reported results.
2) The 5 kHz stimulation frequency (comparable to invasive electric stimulation) used in [22] is insufficient to produce the claimed 11 kV/m² gradient (the activation threshold of pyramidal neuron).
3) If the imbalance occurs between horizontal and vertical orientations, the vertical neurons on both sides of the coil should be activated instead of one side.

Figure 10. (a) – (c)below are the simulation and experiment results of the V-shape coil in [22]. Analysis of the gradient distribution in Figure 10. a reveals an obvious directional asymmetry, with significantly stronger field gradients in vertical direction compared to horizontal (indicated by the more intense color). This observation is quantified in Figure 10. b, where the peak amplitude of the vertical gradient (red) exceeds that of the horizontal gradient (blue). To verify this simulation results, our COMSOL simulations of coils with same dimensions, geometry, and input current parameters (applied a much higher 13Mhz frequency used in [110] to make the results comparable to [22]) failed to reproduce the claimed field asymmetries. As reflected in Figure 10. f, there is not much difference between each peak values. This inconsistency is also questioned by other researchers like in [315].

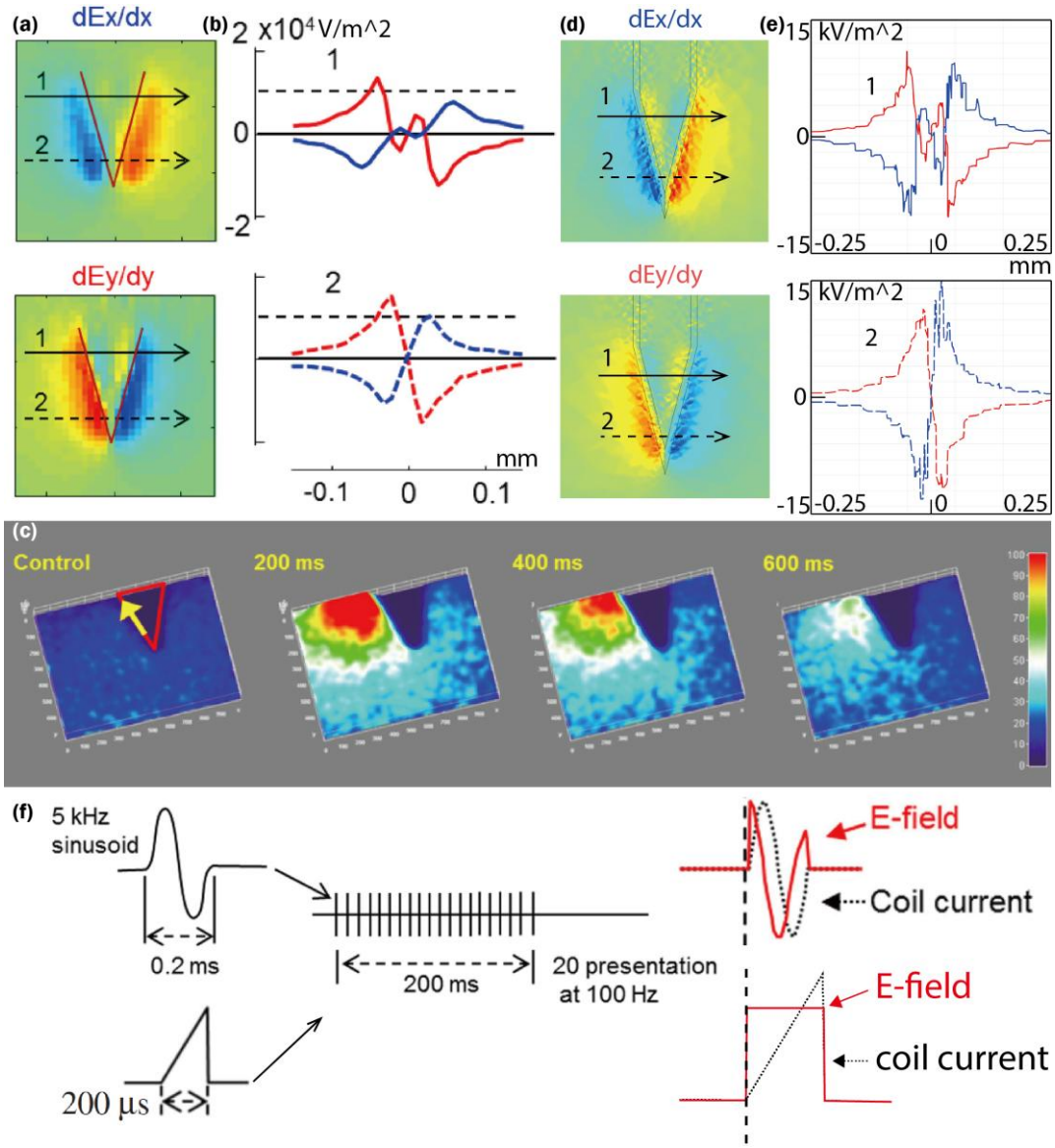

Figure 10. (**a**) Spatial distribution of the electric field gradient in horizontal (top) and vertical (bottom) orientations. (**b**) Quantitative comparison of electric field gradient magnitudes along the solid arrow (top) and dashed arrow (bottom) directions. (**c**) experimental results of V-shape coil in [22]. (**d**) - (**e**) Comparable simulation results to (a) and (b) by our work. (**f**) the input waveform, stimulation frequency, and corresponding induced electric field in [22] (top) and [131] (bottom).

To theoretically analyze this discrepancy, we modeled the electric field gradients generated by oblique conductors. As shown in the Figure 11. Abelow, consider a current-carrying conductor of length $2L$ in air, oriented at an angle θ relative to the y axis, carrying current I. For point P located at distance d along the central perpendicular axis. Assume the function of electric field at P is $\vec{E}(\mathrm{d})$. Then the function of electric field's x-component and y-component are $E_x(d) = sin\theta E(\mathrm{d})$ and $E_y(d) = cos\theta E(\mathrm{d})$ respectively. Assume gradient function at P is:

$$E'(d) = \lim_{\Delta d \to 0} \frac{E(d+\Delta d) - E(d)}{\Delta d} \tag{3.1}$$

Through appropriate model simplifications, we derive from Eq. 2.6 that the induced electric field maintains approximate parallelism with the conductor orientation. Thus, this simplified formulation suggests that the electric field magnitude remains effectively constant for all points equidistant from the conductor. Under these model assumptions, the electric field magnitude at a point displaced by Δd in both the perpendicular and parallel directions can be expressed as $E_{hor}(d+\Delta d) = E(d + cos\theta \Delta d)$ and $E_{ver}(d+\Delta d) = E(d + sin\theta \Delta d)$. Then the gradient of x-component of the electric field can be calculated by:

$$E_x'(d) = \lim_{\Delta d \to 0} \frac{E_x(d+\Delta d) - E_x(d)}{\Delta d} = \lim_{\Delta d \to 0} \frac{sin\theta [E_{hor}(d+\Delta d) - E(d)]}{\Delta d}$$
$$= \lim_{cos\theta \Delta d \to 0} \frac{sin\theta cos\theta [E(d+cos\theta \Delta d) - E(d)]}{cos\theta \Delta d} = sin\theta cos\theta E'(d) \tag{3.2}$$

arly, the gradient of y-component of the electric field can be calculated by:

$$E_y'(d) = \lim_{\Delta d \to 0} \frac{E_y(d+\Delta d) - E_y(d)}{\Delta d} = \lim_{\Delta d \to 0} \frac{cos\theta [E_{ver}(d+\Delta d) - E(d)]}{\Delta d}$$
$$= \lim_{cos\theta \Delta d \to 0} \frac{sin\theta cos\theta [E(d+sin\theta \Delta d) - E(d)]}{sin\theta \Delta d} = sin\theta cos\theta E'(d) \tag{3.3}$$

ield gradient components exhibit equal magnitude in both orthogonal directions, which is consistent with the results from COMSOL simulation.

To rigorously validate this theoretical framework, we conducted numerical simulations based on mathematical analysis. The initial step involves deriving the field function of the distance d, $E(d)$ from Eq. 2.6:

$$\vec{E}(\mathrm{d}) = -j\mu_0 fI \int_{-l}^{l} \frac{dx}{2\sqrt{x^2+d^2}} = -j\mu_0 fI \ln \left| \frac{l+\sqrt{l^2+d^2}}{-l+\sqrt{l^2+d^2}} \right| \tag{3.4}$$

Introducing the parameter k (where $d = kl,\ k > 0$), Eq. 3.2 simplifies to:

$$\vec{E}(k) = -j\mu_0 fI \ln \left| \frac{1+\sqrt{1+k^2}}{-1+\sqrt{1+k^2}} \right| \tag{3.5}$$

By applying the equations above, the difference between the horizontal and vertical field gradients can be calculated using MATLAB. Take the example of $\mu_0 fI$ equals 1 and θ equals 30°. As illustrated in Figure 11. B, the difference between horizontal and vertical gradient decreases rapidly as Δd approaches 0, which means the gradient in two directions are almost eaqual. Although this study examines a simplified model based on a specific oblique wire model, the conclusion holds for arbitrary field distributions. At any given point, the condition $E'_x = E'_y = sin\theta cos\theta E'$ is satisfied. Therefore, this result confirms that the oblique wire and its oblique angle do not contribute to any actual imbalance in the gradient distribution. Consequently, there is no basis for the claimed selectivity in Section 3.2.1.

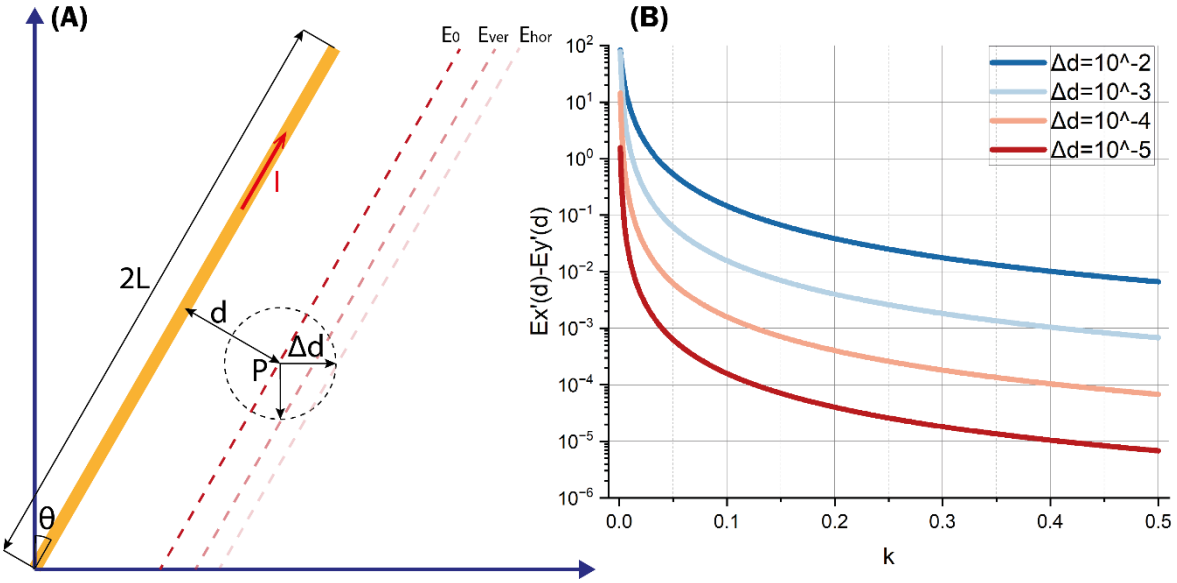

Figure 11. (**A**) Simplified model of calculating electric field gradient on an oblique wire. (**B**) The change in difference between the horizontal and vertical electric field gradient along Δd approaching 0, when $\mu_0 fI$ equals 1 and θ is 30°.

3.2.3 Hypothesis of Impulse-triggered Stimulation

Assuming the experimental results and data reported in [22] are valid and reliable, demonstrating selective activation of nerve cells, two critical questions require explanation. First, if a 5 kHz signal cannot generate a sufficiently large field gradient and no gradient difference exists between orthogonal direction, what underlies the observed axon activation? Second, why is activation restricted to one side of the probe rather than both?

The resolution to the first question emerges from analysis of the waveform described in [22]. The 5 kHz current signal employed in the study was not a continuous sinusoidal wave, but a single-cycle sinusoidal pulse (Figure 10. f top left, above) delivered at 100 Hz (Figure 10. f mid). Since in a sinusoidal signal there is a 90° phase difference between the induced electric field and the current, thus, the resulting electric field formed a single-cycle cosine function during each activation period (Figure 10. f top right). This configuration produces a rising

edge in the electric field, creating a pulse-like differential in time domain. In the authors' follow-up work [131], they replaced the sinusoidal waveform with a periodic triangular signal, which transformed the induced electric field into a unipolar square wave (Figure 10. f bottom waveform). The experimental results obtained with this modified waveform were fundamentally consistent with those from the V-shape coil with sinusoidal input. This consistency suggests that the rising edge should be a necessary requirement for activating neurons, which explains how neural activated despite the 5 kHz is too low to have large enough gradient.

For the second question, we need to look at the unique characteristics of the experimental setup. The authors employed pyramidal neurons which have a distinct unidirectional orientation, and hence the majority of axons are lying in same direction (e.g., from top somas to bottom axons). The difference between the gradient at two sides is the direction (reflected in value, half positive and half negative). Only the MEPs travel from axon to soma will induce the response, but only one side will satisfy this situation while the other side will evoke MEPs travelling in opposite direction from soma end to axons. This explains why only neurons on one side is activated.

As shown in Figure 10. c, the stimulated area superpositions with high gradient area, which suggest the gradient still involves in the evoking process. Therefore, this hypothesis believes that there are three bases for the spatial selectivity shown in [22]:

1) Only a sudden applying of induced electric field can trigger MEPs.
2) The magnitude of the gradient of the electric field determines if can induce MEPs, while the direction of it determines the direction of transmission of the MEPs.
3) Only the MEPs transmit from the axon to soma can truly activate the neurons.

Therefore, the following conclusions can be drawn: the imbalance of the gradient is still important, as it is the basis for selectively activating neurons in a certain direction; the selective activation in experiment [22] is not the result of imbalance but the result of the characteristics of the selected experimental pyramidal neuron’s properties; imbalance alone is not enough, a sudden change in the electric field is also required to induce action potentials.

3.3 Probe micro-Coil Designs for Invasive Magnetic Stimulation

Based on the theoretical framework and analysis of selective neural stimulation, here propose multiple optimized probe micro-coil designs based on above theoretical explanation.

3.3.1 Double Loop Rectangular Coil

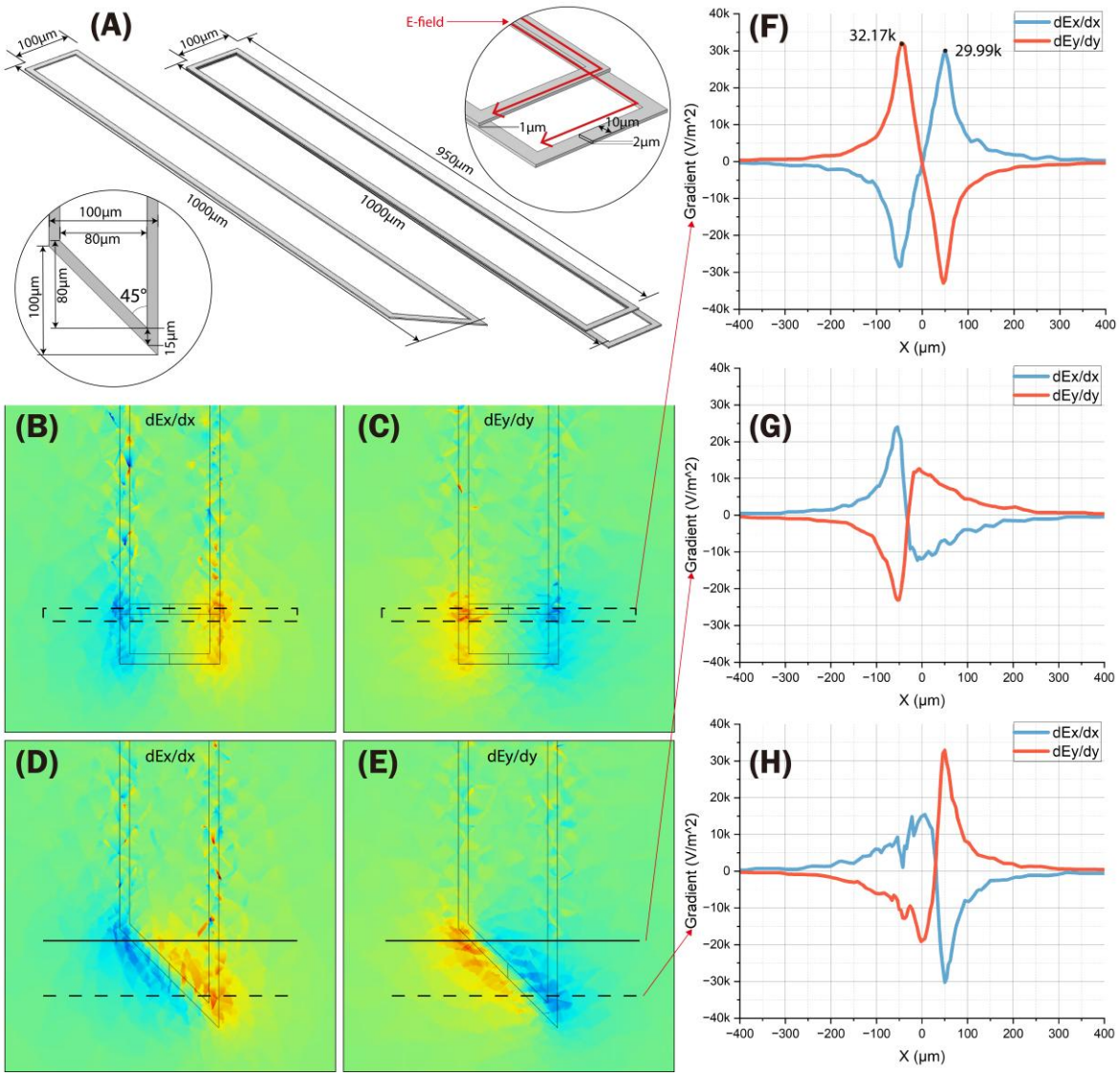

Figure 12. (**A**) The design of double loop rectangular and half-V shape coil. (**B**) and (**C**) Ther horizontal and vertical electric field gradient of double loop coil. (**D**) and (**E**) Ther horizontal and vertical electric field gradient of half-V shape coil. (**F**)The average gradient value of vertical and horizontal direction between the dashed line in C and D. (**G**) Horizontal gradient of induced electric field. (**H**) Vertical gradient of induced electric field.

As proved in previous section, the oblique design does not provide imbalance of gradient in orthogonal direction. This double loop rectangular configuration aims to bring true gradient imbalance. In contrast to the previously discussed V/W-shape coil configurations, the current approach does not employ specialized geometric shaping. Instead, it strategically utilizes the spatial arrangement of two coils to control the field distribution. The design is shown in Figure 12. A. As described by Eq. 2.6, the induced electric field principally aligns with the current flow (red arrows in Figure 12. A). In this configuration, the superimposed field separates, and the field diverges into two components: one maintaining vertical orientation, while the other turns to horizontal direction. Then a discontinuity forms in the vertical field

component, while the parallel field component has more spatial uniformity because of the limited separation between the horizontal wires.

The resulting field distribution produces a substantially enhanced vertical gradient compared to the parallel gradient as shown in (Figure 12. B and C). The numerical results (Figure 12. F) provide clear visual confirmation of this gradient imbalance, with the region between the dashed markers in Figure 12. B and C. Quantitative evaluation of this region demonstrates the vertical gradient has an average 7.3% magnitude advantage over the parallel gradient, providing evidence of the gradient asymmetry. However, possible concerns of this coil design may include narrow stimulation region and complex coil structure which increase difficulties for fabrication.

3.3.2 Half V-shape Coil

As previously noted, selectivity is inherently linked to the pursuit of asymmetry. Consequently, asymmetry can be more explicitly incorporated into the coil's geometric design to strengthen, for example, one-side stimulation. In this approach, half of the V-shape coil was adopted and shift the oblique segment to a single side (Figure 12. A). As illustrated in Figure 12. D and E, this design results in an asymmetric field gradient distribution across the coil. Specifically, local extremal regions form at the angles where the wire change direction. By extracting the field gradient values along horizontal lines passing through the centers of these regions (solid and dashed lines) shown in Figure 12. G and H. By comparing these diagrams, the field gradient magnitude near the obtuse-angle bend is markedly smaller than that near the acute-angle bend. Meanwhile, the value of gradient in two directions are roughly oppositely equal, therefore, there is still no imbalance between them as proved in previous sections.

3.3.3 Smooth Wire Coil

According to the hypothesis in Section 3.2, neural stimulation will still concentrate in regions where the gradient exceeds the threshold. Consequently, reducing the spatial extent of these regions can enhance stimulation resolution. Taking the V-shaped coil as an example, Figure 13. C reveal that the primary stimulation focus lies on the exterior of the V’s left side, while a secondary focus emerges on the interior of the V’s right side (marked with red line). This secondary focus may induce unintended neural activation, thereby compromising the overall stimulation precision of the coil. A method is proposed here to eliminate the secondary stimulation focus that inherently arises along straight conductors. As demonstrated in Figure 13. A and B, when comparing circular and square coils under identical conditions, replacing the square configuration with a circular geometry yields two significant improvements:

1) The gradient magnitude inside the circular coil is much weaker.
2) The external gradient field exhibits greater spatial concentration with higher average intensity (indicated by deeper color).

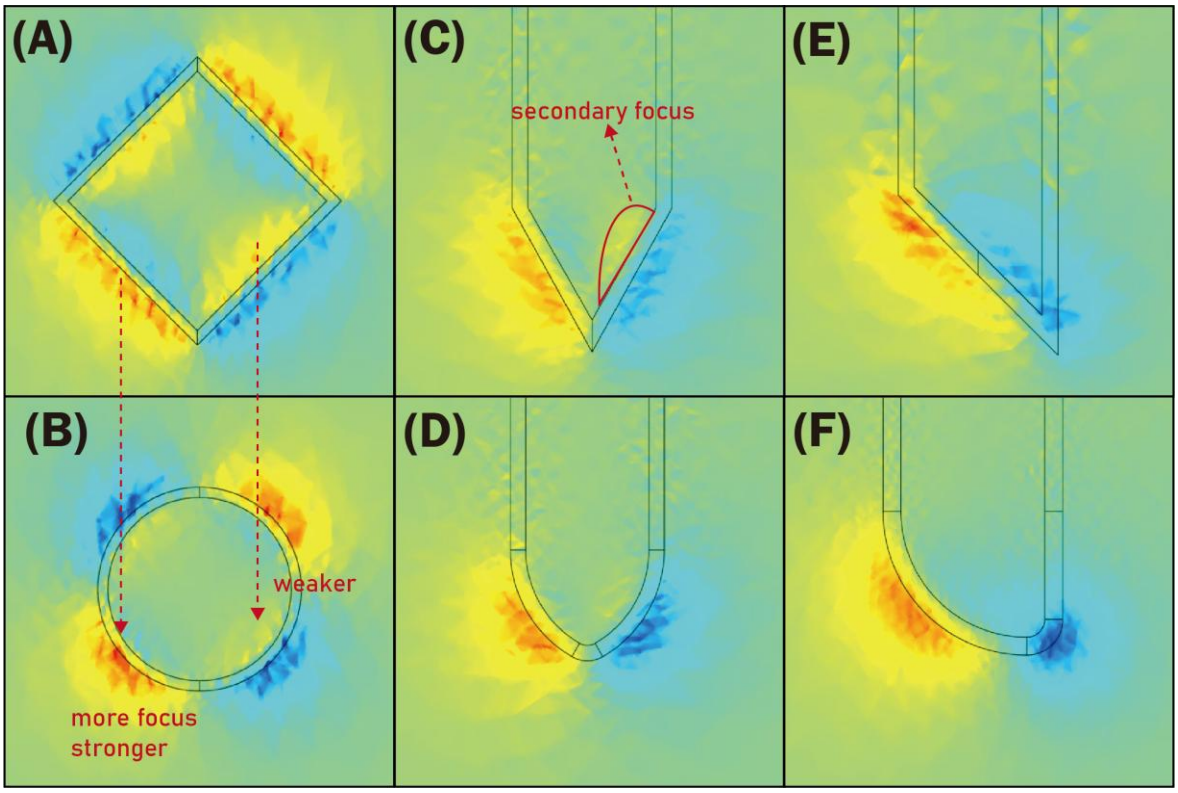

Figure 13. The vertical electric field gradient (dEy/dy) distribution of various coil shape designs before and after smooth wire optimization.

These observations suggest that round conductors effectively suppress the formation of side stimulation center within coil interior region while simultaneously producing more focused and intense stimulation center externally. Perform smooth optimization on both the original V-shape and half V-shape coil configurations. Using dEy/dy as an example, the simulation results are presented in Figure 13. C-F. As predicted, comparison between Figure 13. C and D demonstrates that smooth modification of the V-shape coil successfully produce its more concentrated and enhanced gradient distribution as intended. Similar effects were observed for the half V-shape configuration: the internal gradient magnitude was globally reduced while the external gradient distribution became more concentrated (especially for blue part) and exhibited with stronger asymmetry, which means this design can realize very constrained stimulation increasing the accuracy.

3.4 Fabrication of PROBE micro-Coils.

After designing, the next step is to transform the design from digital to physical. Considering the coil's properties (particularly its size and layer-by-layer structure), cleanroom would be the most suitable fabrication strategies. Based on fabrication recipe from [30, 316], after

proper modification, a fabrication process and a updated version combined with laser process used to fabricate this type of coil are illustrated in Figure 14. There are four main steps: substrate preparation (Figure 14. A-B), coil circuit deposition (Figure 14. C-G), encapsulation (Figure 14. H), probe shaping and pad exposure (Figure 14. I-J/ K).

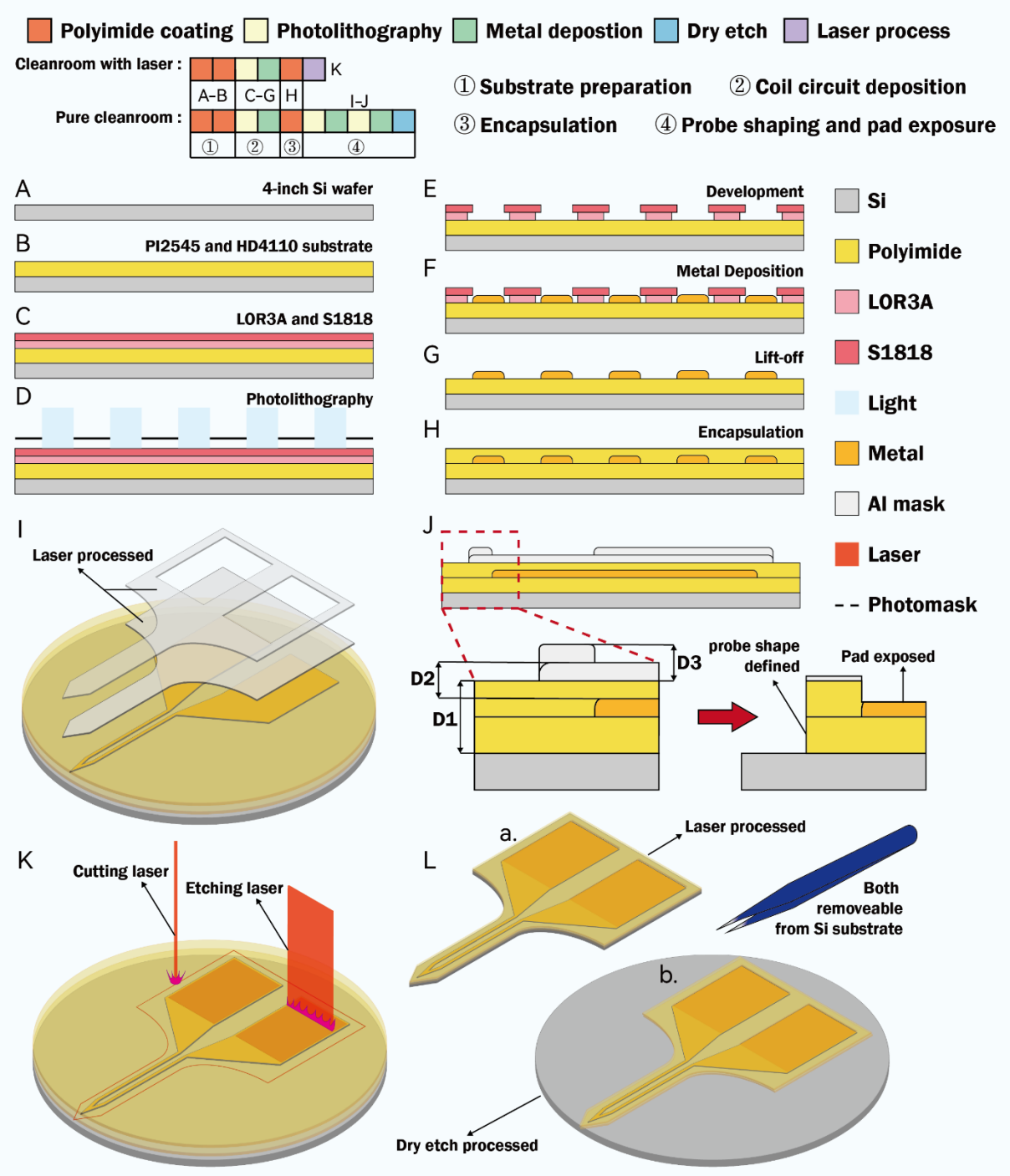

Figure 14. Brief timeline comparing the pure cleanroom and cleanroom-laser approaches. **A-H.** Common fabrication steps: substrate preparation, coil circuit deposition, and encapsulation. **I.** Dry etch cover mask structure. **J.** Etching via dry etch. **K.** Laser processing of the sample. **L.** Final probe processed by **a.** Laser; **b.** Dry etch.

3.4.1 Pure Cleanroom Strategies for Probe micro-Coil Fabrication

In the substrate preparation process, on a cleaned Si wafer, PI-2545 was spin-coated at 1000 rpm for 30 seconds, soft-baked at 140°C for 5 minutes, and then cured for two hours in a nitrogen oven at 300°C. Following this, HD-4110 substrate was spin-coated at 2000 rpm for 30 seconds, soft-baked at 110°C for 5 minutes and subjected to the same curing process as described above. In the coil circuit fabrication process, photolithography is used to define the coil shape, followed by metal deposition using a plasma evaporator. The photolithography process is carried out as follows: LOR3A and S1818 are sequentially spin-coated at 4000 rpm and 3000 rpm for 30 seconds and soft-baked at 185°C for 5 minutes and 115°C for 75 seconds. The substrate is then exposed to 18 mW/cm² power under film photomasks by Micro Lithography Services, UK, for 2.5 seconds. After photolithography, S1818 is developed for 70-75 seconds in Microposit Developer Concentrate, while LOR3A is developed in MF-319 for 3 minutes then. After development, the coil metal is deposited, and the coil shape is finalized through an overnight lift-off process in SVC-14. Then repeat the process of PI-2545 above to complete the encapsulation step. The thickness of the encapsulation would be around 25-30 μm (5 μm PI-2545/ 15-20 μm HD-4110/ 5 μm PI-2545).

As last step will encapsulate all the metal in polyimide, wiring pads need to be exposed. This is completed simultaneously with the shaping of the probe by dry etch. This step relies on the different etching rates between polyimide and metal in etching. Given that polyimide etches at a much faster rate than metal, aluminum (Al) can be used as a masking layer to protect the parts of the probe that need to be retained, and Al mask covering the wiring pad area should be thinner to allow the polyimide above the wiring pad etched away. To achieve this, the previous photolithography process is repeated twice to cover the top of the probe with two layers of Al mask. The first layer is designed to cover the entire probe area and the second layer will cover the same area except the wiring pad part (Figure 14. I). Based on the experimental-measured etching rates (polyimide: ~0.7μm/min, Al: ~2 nm/min), the required mask thickness must satisfy the following relationship: time to etch 30 μm of polyimide (D1 in Figure 14. J) ≤ time to etch 5 μm polyimide + time etch first layer mask (D2) ≤ the required to etch both masks (D3). This setup ensures that no residue remains after the probe is finalized, the wiring pad is fully exposed, and the probe body is protected from etching. After the etching process, any remaining unetched mask above the probe can be removed using an Al wet etching solution. The final product is illustrated in Figure 14. L. a. Once the mask is removed, the flexible probe can be easily detached from the wafer.

Overall, the limitations of this method can be summarized as follows:

- The highly complex fabrications process, and in particularly the final exposure and shaping steps, which require multiple rounds of lithography alignment and dry etching

process. The use of hazardous chemicals, such as TMAH, introduces safety risks into the production process, further increasing the overall complexity. This complexity increases the likelihood of errors.

- The high fabrication cost and effort associated with parameter optimization for dry etching are substantial.
- The performance of dry etching exhibits considerable variability, making precise quantitative analysis challenging. The etching rate can only be estimated through repetitive experiments, further complicating calculation considerations and increasing uncertainty.
- Due to the properties of dry etching equipment in JWNC, many commonly used materials, such as Au and Cu, cannot be processed. Al cannot be used for the coil either, as it is employed solely as a masking material and is ultimately removed at the end of the process. Consequently, this limitation demands the use of other metals, such as Pt, which often have lower conductivity, thereby compromising the overall performance of the coil.
- Finally, the production process is highly time-consuming. For instance, steps such as lithography, development, and deposition require significant time and effort. Even with proficient skills and efficient time management, completing a single layer of masking typically takes at least an entire day. Besides, since each test run necessitates repeating all preceding steps aggravates the problem.

3.4.2 Laser Processing Strategies for Probe micro-Coil Fabrication

From the above analysis of the pure cleanroom strategy, it is evident that more than half of the workload is concentrated in the fourth step, which involves exposure and shaping. If this step could be replaced by a more efficient and flexible method, it would significantly enhance production efficiency. Laser-based processing emerges as one of the most effective solutions. Lasers can effectively address the limitations of dry etching in several ways:

- **Faster iteration.** Laser Parameters optimization is significantly faster and cheaper compared to dry etching. Since lasers can selectively target individual probes or specific areas rather than processing the entire wafer simultaneously, multiple testing can be conducted on a batch of products on one wafer. This approach enables rapid iteration.
- **Material flexibility**. Standard lasers are material-insensitive, offering a broader range of material options. This flexibility allows for the use of materials that are incompatible with dry etching, expanding design possibilities.

- **Rigid substrate compatible**. While cleanroom steps are primarily suited for flexible electrodes, the laser-based strategy proposed here can be applied to manufacture both probe with rigid substrate also, increasing its versatility.

The laser-based production process is highly time-efficient and enhances the safety of the production process by reducing reliance on hazardous chemicals and complex cleanroom procedures. This makes it a more practical and scalable solution for advanced manufacturing. However, on the other hand, the challenges rising from the laser-based solution. Since there is not sufficient accumulated data on laser etching and cutting processes, it is necessary to have extensive testing for optimal parameters. Besides, developing an effective interface algorithm to integrate the cleanroom and laser strategies is critical. Such an algorithm would enable the laser instrument to accurately locate, etch, and cut specific areas, ensuring precision and consistency in the manufacturing process.

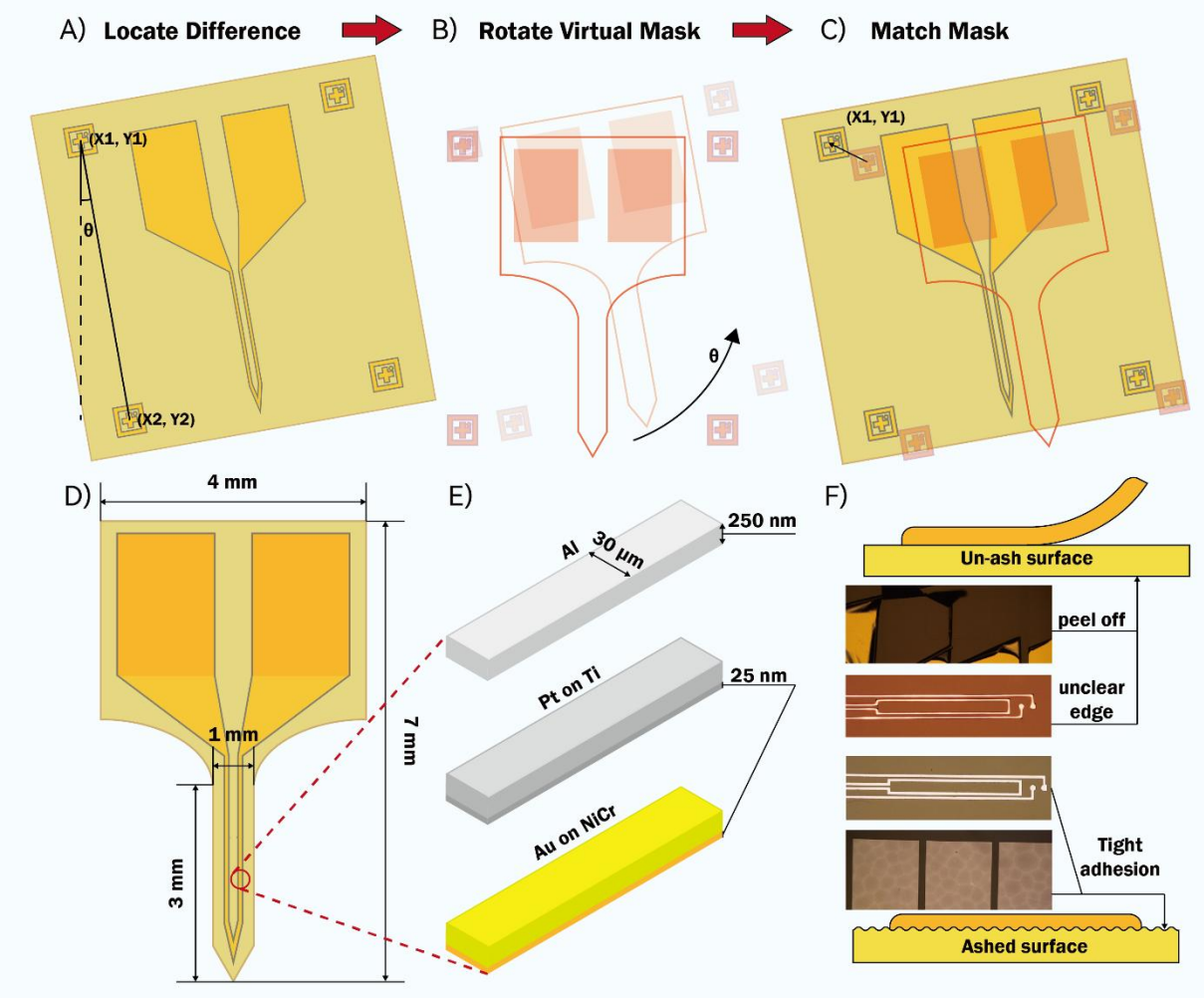

Figure 15. **A**)-**C**). Alignment strategies for laser machine. **D**). Dimension of micro probe. **E**). Dimension of metal track in deposition. **F**). Effect of surface roughness.

The performance tests were conducted on MicroLine2000, LPKF, Germany. Since polyimide is very delicate under laser, the optimized etching parameters for 5 µm PI-2545 were 0.05W 300mm/s 2repetition without isolation step, while the optimized cutting parameters for 0.3

mm thick Si wafers were 4.8W 200mm/s 70repetition (details on how these parameters influence processing will be discussed in Section 4.1.2). The alignment strategies are illustrated in Figure 15. The idea of aligning virtual masks with samples in laser machine is inspired by the experience on aligning physical masks with samples in lithography. The most critical information required for alignment is determining the positional discrepancy between the mask and the sample, which can be described by two variables: the angular difference of the corresponding edges and the positional difference of the corresponding points. Since the default input state of the virtual mask is vertical, alignment can be achieved by identifying the angle between the sample and the vertical direction, as well as the coordinates of the sample within the software. The alignment process involves the following steps:

1) Use the camera of the laser instrument to locate two alignment marks on the sample and record their coordinates (Figure 15. A).
2) Calculate the angular difference between the sample and the virtual mask based on the alignment marks (Figure 15. A).
3) Rotate the virtual mask in the software to match the calculated angle (Figure 15. B).
4) Align any two corresponding points between the sample and the virtual mask to complete the alignment (Figure 15. C).
5) Once aligned, proceed with the laser processing. After processing, the probe is like Figure 14. L a. The probe can be removed from Si substrate as flexible probe or keep Si substrate as rigid probe.

3.4.3 Probe Fabrication and Challenges

Based on the methodology outlined in Section 3.4.1, this section provides more details about the design, material selection, potential challenges, and corresponding solutions. The entire fabrication process is conducted on a 4-inch Si wafer. The probe micro-coil is designed with dimensions of 4 mm × 7 mm, featuring the probe part that is 3 mm long and coil wires 30 μm wide (Figure 15. D and E). This reduced size (compared to the probe used in DBS) is more suitable for prototype optimization and animal test, as it allows for more samples to be fabricated on a single wafer, thereby reducing both time and financial costs. A total of 124 probe micro-coils are arranged on one 4-inch wafer like shown in Figure 16. A. Three types of metals were selected for deposition, each with a thickness of 250 nm: Platinum (Pt, on 25 nm Ti), fabricated using the dry etch method; Au (on 25 nm NiCr) and Al, fabricated using laser cutting. Pt was selected due to its suitability for dry etching, as previously discussed. Au, a commonly used material with excellent stability and electrical properties, was chosen for its proven biocompatibility. Although Al is not typically considered suitable for implantable applications, it was included to test the biocompatibility of the probe's encapsulation.

Additionally, Al's low cost and abundant availability offer unique advantages for this application.

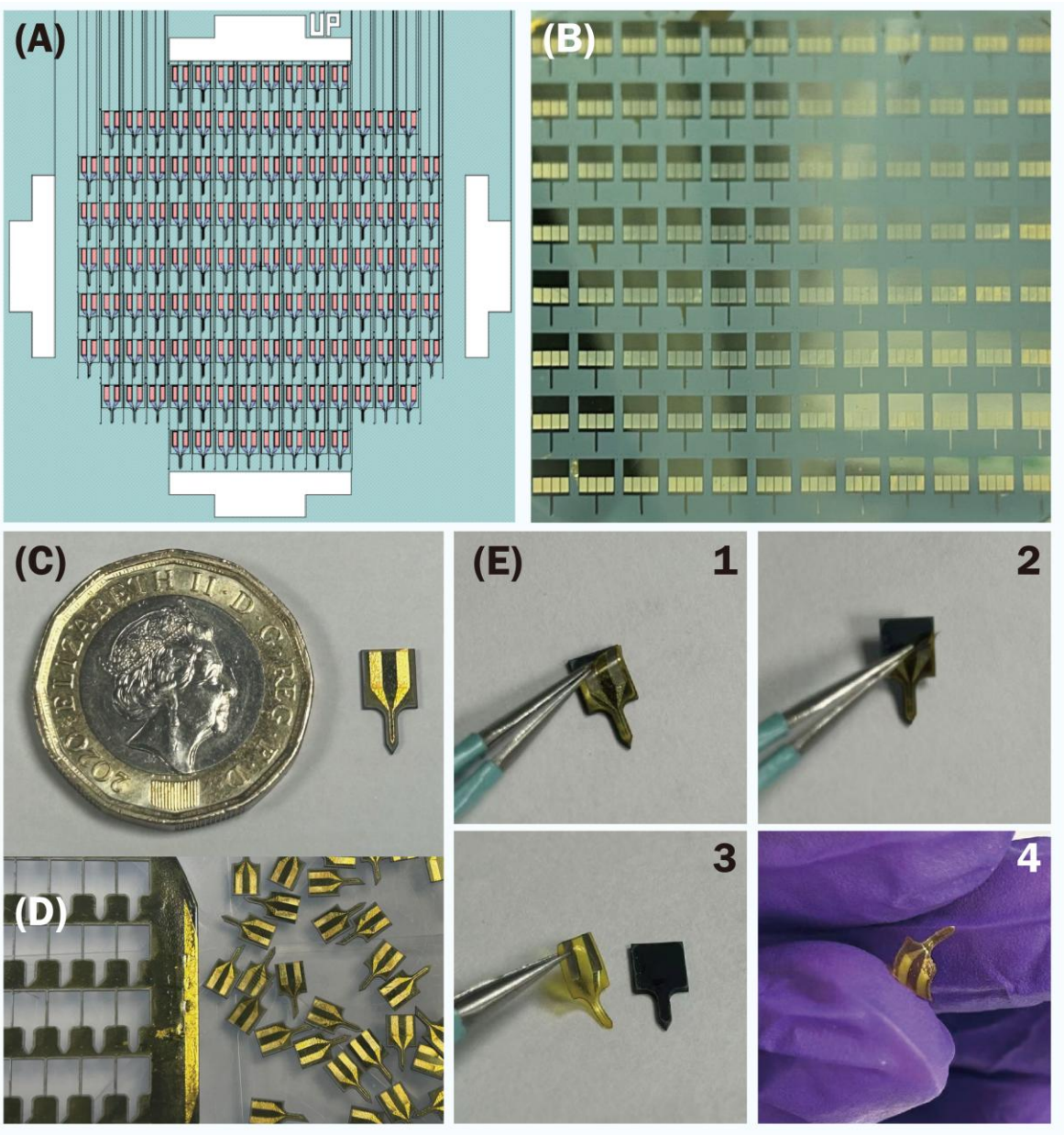

Figure 16. (**A**). Photolithography mask design. (**B**). The probe after dry etching before removing aluminum. (**C**). Rigid probe after laser processing. (**D**). Large scale manufacturing of probe micro-coil. (**E**). Flexible probe micro-coil and its pealing-off from Si substrate.

For challenges, metals, particularly Au and Pt, may detach from the polyimide after the lift-off process. To address this, one can either introduce an adhesion-promoting layer, such as Ti or NiCr, between the metal and polyimide to enhance bonding, or roughen the polyimide surface before metal deposition to improve adhesion by asher (Figure 15. F). However, this approach is less preferred as increased surface roughness can elevate the wire resistance, potentially affecting performance. Therefore, only apply after observing adhesion problems. Besides, after wet etching of Al, the probe maybe detaches from the wafer directly. If

detachment does not occur naturally, soaking the wafer in clean water for several hours can facilitate the process.

3.4.4 Fabrication Results and Electric Characteristics Performance

Coils fabricated from all three materials were successfully produced, with the resulting probes shown in Figure 16. This achievement validates the stability and reliability of the two production methods in large scale, as illustrated in Figure 16 B and D. Additionally, the laser-based fabrication strategy was demonstrated to be compatible with both rigid and flexible substrates, with examples of the final products for each substrate type presented in Figure 16 C and E. Resistance measurements were conducted on three different metal materials. At a metal deposition thickness of 250 nm, the average resistances of the Au, Al, and Pt circuits were measured to be 24 Ω, 33 Ω, and 118 Ω, respectively. The ratio of these resistances aligns with the inverse ratio of the electrical conductivities of the three metals. Variations in resistance may arise from non-uniform metal deposition during fabrication, as well as the roughness of the substrate. Obviously, the Pt coil is not suitable for this application because of its high expense, complex fabrication, and low electrical performance. Therefore, the fabrication method containing laser processing is a better choice and the following biocompatible experiments will be applied to Au and Al coils only.

3.5 Biocompatibility of Laser-assisted Fabrication of Probe micro-Coil

To demonstrate the biocompatibility of this laser-assisted coil fabrication process, both Au and aluminum coils were tested cell viability assay. The setup details are provided in appendix 7.1. Three images from each well were taken using bright field, Fluorescein isothiocyanate, and Texas Red channels of the Olympus IX71 microscope. The monomeric binding of acridine orange to DNA results in green fluorescence). On the other hand, even though propidium iodide is also DNA-intercalating dye, it is excluded from cells that still contains their plasma membrane integrity and can only stain cells that already lost their membrane functions. It is still possible to detect apoptotic cells through PI, but at the same time PI can stain necrotic cells as well. This combination of different dyes therefore makes them suitable for viability assay where different colors can be used to distinguish viable cells from others (Figure 17). One-way ANOVA showed no significance between the experimental groups and control, and it is still possible to observe a higher percentage of necrotic cells in the control group compared to experimental groups. Figure 17 still demonstrates that both Al and Au based probe micro-coil has no significant impact on the cellular growth even in instances where Mouse aorta smooth muscle cells (MASMCs) were in direct contact with the probe micro-coil as can be seen in Figure 17. B1 and C1. Therefore, both probe micro-coils

are biocompatible and suitable for *in vivo* studies. Especially, the Al coil result proves that it is possible to use cheap materials in this technique (Al is free in JWNC metal deposition while Au cost hundreds of pounds for one time deposition), which will significantly decrease the cost of fabrication.

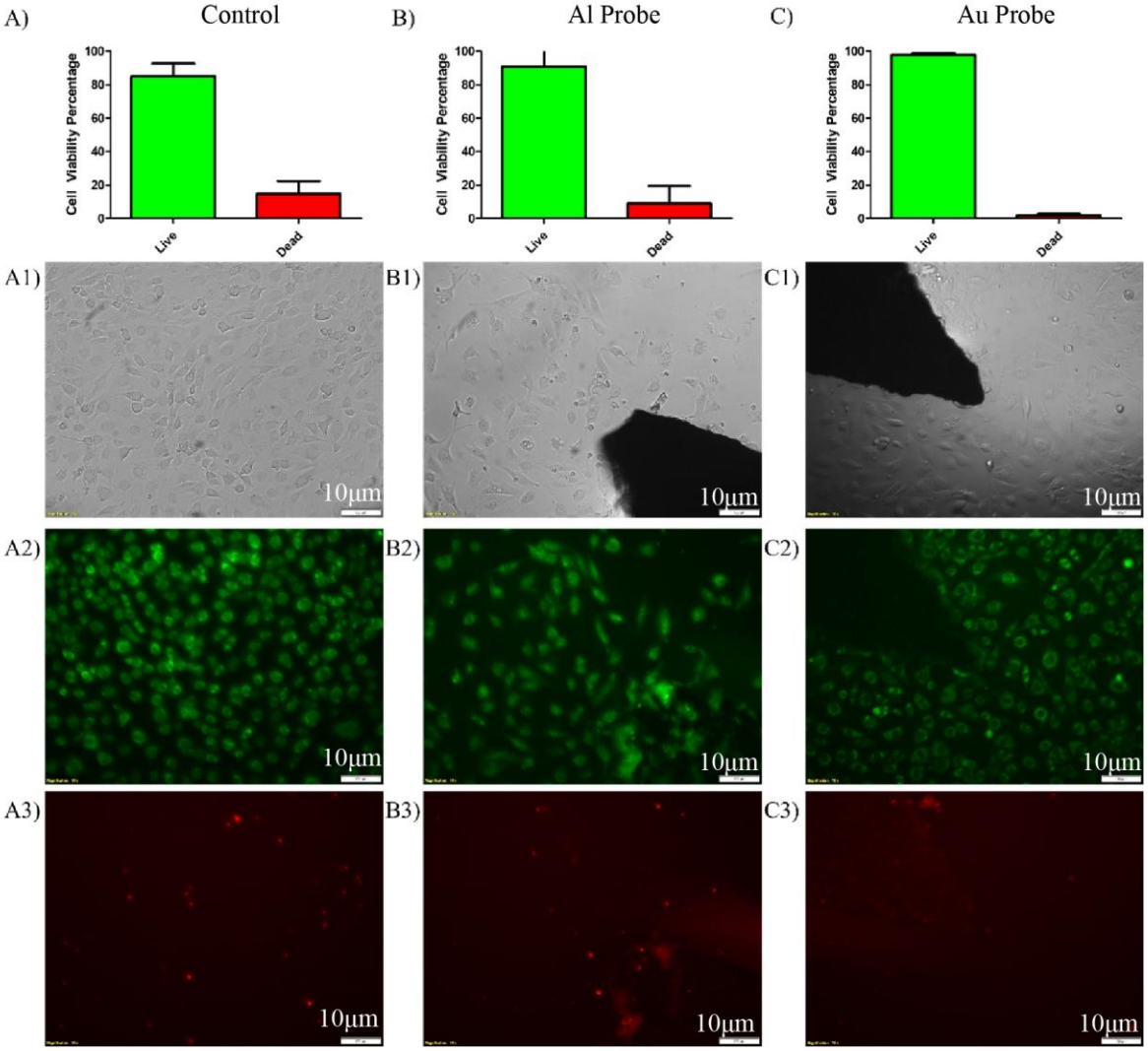

Figure 17. Cell viability results of different material implants of **B**) Al and **C**) Au showing strong cell viability with no significant difference to **A**) control experiments when compared with one-way ANOVA (p 0.1850, ns, Tukey post-test, n=3). In each group, **A1**), **B1**) and **C1**) represents brightfield images of the well containing its respective material whereas **A2**), **B2**) and **C2**) represents live SMCs stained by acridine orange, and **A3**), **B3**) and **C3**) dead/necrotic SMCs stained by propidium iodide.

4 Coil Design and Optimization for Nano-invasive Magnetic Stimulation

As discussed in the literature review, current coil designs for nanoscale invasive magnetic stimulation remain limited to conventional solenoids. While solenoid configurations offer simplicity, they present two critical limitations:

1) Poor ergonomic compatibility for human applications
2) Low spatial precision that limits targeted stimulation of specific brain areas.

These fundamental constraints necessitate the development of novel coil architectures specifically tailored for nano-invasive magnetic stimulation. An ideal design should address three key requirements: wearability, localized stimulation capability, and power consumption. One potential solution involves deploying an array of miniature coils integrated into a helmet platform. Through selective activation of specific coil, this configuration could simultaneously address all three requirements. Based on this idea, given the limited prior work in this research direction, this section systematically explores mini-coil (cm scale) designs by referencing some configuration of TMS and μMS. Two coil design configurations (planar spiral coil and mini slinky coil) are selected, and their fabrication processes are optimized. Through this investigation, we aim to achieve an optimal balance between three key objectives: electromagnetic performance, cost-effectiveness, and rapid fabrication iteration capability. As clinical translation remains premature, the present design focuses primarily on preclinical applications, with specific optimization for animal studies using rat models. The system targets following technical specifications: the capability to generate around 25 mT magnetic fields at an approximate 1 cm (around the thickness of scalp and skull of rats) working distance from the coil across both low (5 Hz for magneto-mechanical stimulation) and high (100 kHz for magneto-thermal stimulation) frequency ranges, meanwhile minimizing the coil heating effects during operation. All subsequent design iterations and evaluations will be conducted with these fundamental performance requirements.

4.1 Mini-Planar Spiral Coil

The proposed coil design draws inspiration from planar coils previously introduced in μMS section, as identified in literature review. While micro-stimulation applications emphasize miniaturized, implantable planar coils at sub-millimeter scales, we adapt this concept by scaling the design to centimeter-level dimensions for wearable applications. This planar coil architecture offers three distinct advantages for applications: its centimeter-scale dimensions

are ideally suited for animal-wearable devices; it can be integrated with flexible substrates to achieve skin contact; and it permits straightforward assembly into multi-coil arrays for spatially targeted stimulation. Beyond its primary application in nanoparticle actuation, this coil design demonstrates significant potential for translational adaptation to other biomedical and engineering applications. As illustrated in Figure 18, implementations include direct neural magnetic stimulation and wireless power transfer for miniaturized implantable devices etc.

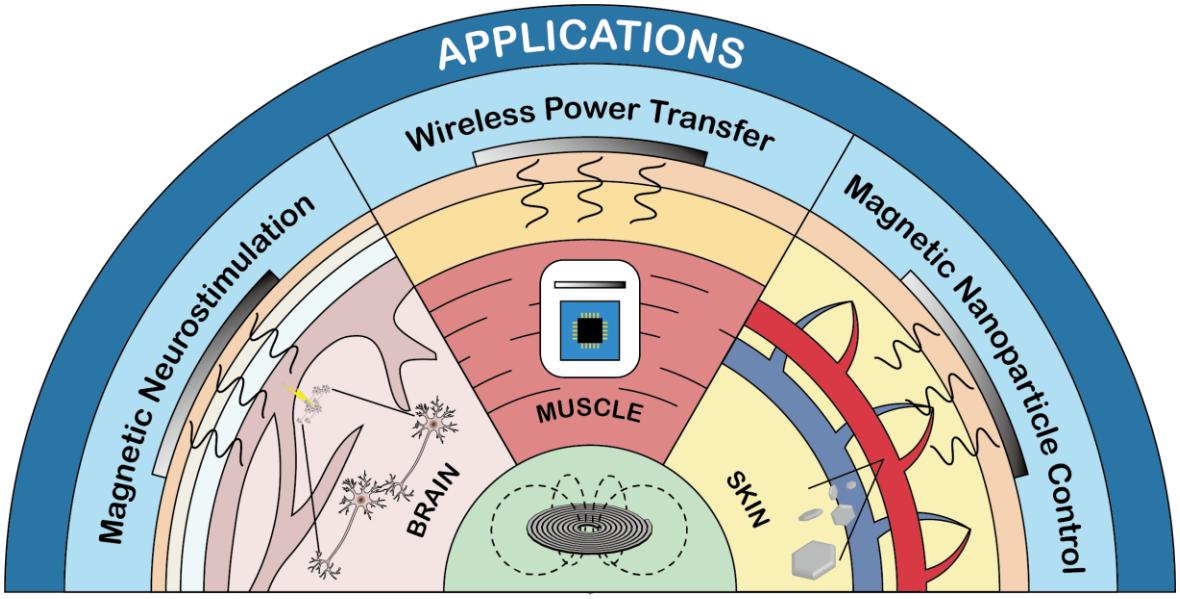

Figure 18. Conceptional figure for mini-planar spiral coil applications.

4.1.1 The Prototyping of Spiral Planar Coil

The initial planar coil prototype employed a conventional circular spiral design with 9 mm diameter coils with 20 turns considering the resolution of laser fabrication. COMSOL simulations demonstrated that when arranged in a figure-8 configuration and driven with 100 mA current, these coils could generate magnetic fields on the order of hundreds of μT, confirming their potential for further optimization. For physical realization, we selected laser fabrication to fabricate the first prototype (the same system in probe micro-coil fabrication mentioned previously). The prototypes were fabricated using standard PCB materials: FR4 laminate substrates with 0.5 oz (17.5 μm) Cu cladding, processed using the laser system's default PCB parameters. As shown in Figure 19. A, a prototype 3×3 coil array with polyimide flexible PCB routing excitation signals to individual coil units while maintaining mechanical flexibility for wearable applications, which give the feasibility of coil array configuration.

The fabricated coils first underwent thermal characterization to establish their maximum operational temperature thresholds. This measurement was programmed using an Arduino

microcontroller system, as shown in Figure 19. C. The Arduino code is included in Appendix 7.2. The coil was connected to a power source, with a MOSFET employed as a switch. When the Arduino output was set to high, the switch turned on, and when the output was set to low, the switch turned off. Temperature measurements were obtained using an NTC 10 kΩ 3950 thermistor. This type of sensor adheres to the following relationship between temperature and resistance:

$$R = R_0 \cdot e^{\beta \cdot \left(\frac{1}{T} - \frac{1}{T_0}\right)} \tag{4.1}$$

where T_0 is the reference temperature (25°C), R_0 is the reference resistance at T_0 (10 kΩ), β is the temperature sensitivity coefficient (3950), and e is the base of the natural logarithm. The temperature was derived mathematically from the measured sensor resistance. The resistance of the sensor was determined by measuring the voltage across a voltage divider circuit, which consisted of a 10 kΩ resistor connected in series with the sensor. In summary, the Arduino calculates the resistance by acquiring the divided voltage through an analog input and subsequently computes the temperature based on the measured resistance. The data were transmitted to a computer via serial communication for recording and analysis. This system will be also used in following measurement of updated version coils.

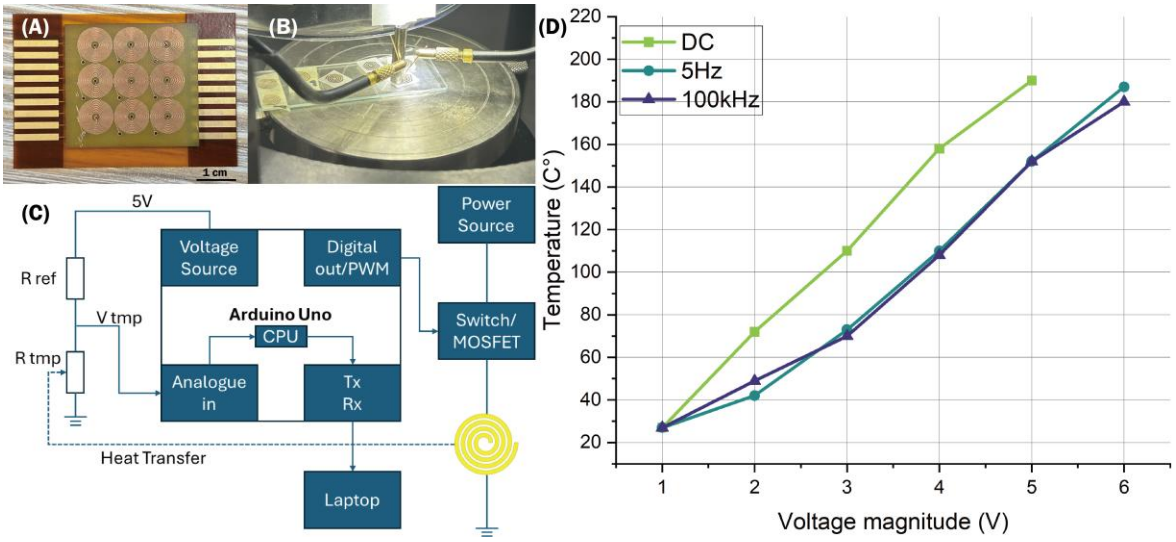

Figure 19. (**A**) Planar coil array prototype with flexible PCB connector. (**B**) Thermal sensor placed on a coil. (**C**) Diagram of the thermal measurement system. (**D**) Temperature of prototype coil with different voltage input under DC, 5 Hz, and 100 kHz frequency signals.

During thermal measurement, the temperature sensor was positioned above the coil center as illustrated in Figure 19. B. We recorded stable measurements under three excitation conditions: (1) DC input, (2) low-frequency AC (5 Hz), and (3) high-frequency AC (100 kHz). The results (Figure 19. D) reveal significantly faster temperature rise under DC excitation compared to AC conditions, consistent with the theoretical greater equivalent thermal power dissipation in DC operation. Meanwhile, within this frequency band the

frequency does not influence heat dissipation with AC source, which is the reason why 5 Hz and 100 kHz signals share the similar temperature curve. All samples ultimately reached critical burning when their temperature reached a range between 180-190°C.

Based on the experimental results, the thin metal layer leads to an increased coil resistance, thereby exacerbating Joule heating. To limit this issue, it is important to minimize the coil resistance by increasing the metal layer thickness. To achieve this objective, three technical approaches were explored: laser processing, photolithography combined with electroplating, and physical cutting.

4.1.2 Laser Processing

Laser technology demonstrates significant advantages in the fabrication of such coils. It offers high precision, making it particularly suitable for fabricating fine micro-devices. Then, the process exhibits a high degree of automation—once the digital design and substrate material are prepared, the final product can be directly fabricated without intermediate processing steps. Besides, a wide variety of commercially available substrates can be utilized, ranging from a few oz to over ten oz in Cu thickness, enabling convenient testing and optimization. After comprehensive evaluation, a 3oz (105μm) copper-clad substrate was selected for fabrication. While thicker Cu layers can further reduce resistance, the etching difficulty and processing time increase disproportionately. The 3oz thickness represents an optimal compromise between these competing factors.

However, since non-standard PCB substrates were employed, the laser parameters required re-optimization. Preliminary adjustments based on estimations failed to achieve the desired results (as shown in Figure 20. A). Specifically, incomplete Cu etching was observed (Figure 20. B and C), indicating the need for a more systematic parameter evaluation, and thus the following experimental study was conducted:

As mentioned earlier, three main parameters affect laser etching: laser power, scanning speed, and number of repetitions. Higher power, slower speed, and more repetitions result in deeper etching. A baseline etching parameter set of 1W, 500mm/s, and 5 repetitions was established (Figure 20. E). The tested pattern is 3 short lines within a square, where the lines correspond to the coil width, while their gap matches the gap width between coil wire. Based on this, while keeping the other two parameters constant, the power was gradually increased to 5W, the speed to 2500mm/s, and the repetitions to 25. Before this, the effect of the isolation step (using high-energy 5W laser to ensure separation between etched and retained portions) was

tested at 5-30 repetitions to confirm if this step is necessary. The comparative results are shown in Figure 20.

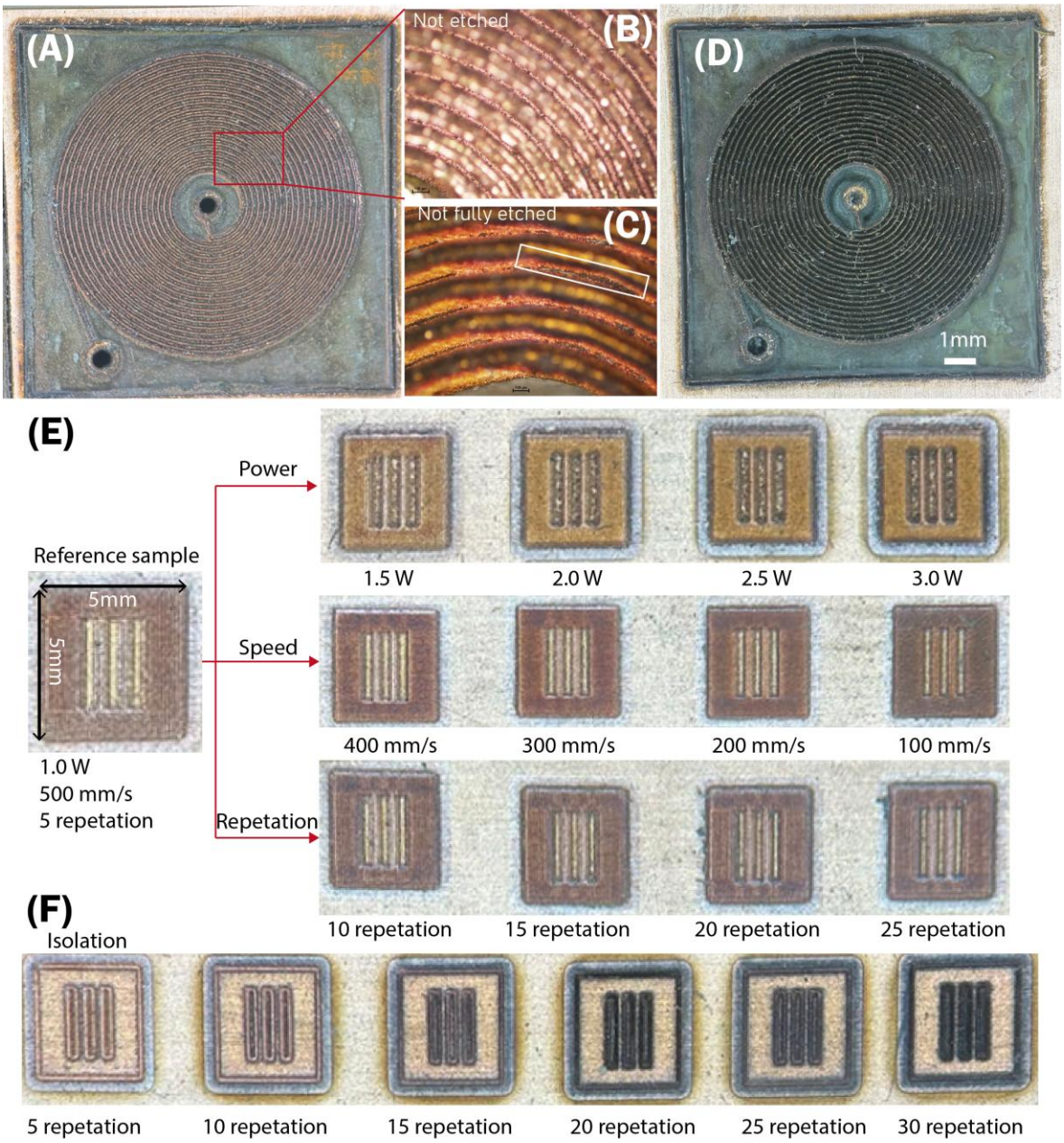

Figure 20. (**A**) Sample before optimization. (**B**)-(**C**) Not/under etched Cu between wire gaps. (**D**) Sample after optimization. (**E**) Comparison etching optimization on parameters of power, speed, and repetition. (**F**) Isolation optimization on parameter of repetition.

From Figure 20. F, two potential issues with the isolation step can be observed: isolation fail and the low resolution. Due to the high-energy laser at low repetition counts, the laser fails to achieve proper isolation, while high repetition counts cause upper layer Cu burning. In addition, the process etched part of the original line width, leading to narrower wire and resistance reduction. Therefore, the isolation step was abandoned in subsequent procedures. From Figure 20. E, a comparative analysis of power, speed, and repetition revealed that power exerted the most dominant influence on the etching process. Substantial enhancement

of etching effectiveness could be achieved by increasing the power level. Scanning speed demonstrated a secondary yet significant effect, primarily governing etching precision, where excessive speeds led to insufficient Cu removal. Repetition count exhibited the most modest impact, showing an approximately linear correlation with etching depth. Based on these findings, the optimized laser processing parameters were established as follows: 2.5 W power was utilized to ensure robust etching performance; a scanning speed of 200 mm/s was selected to maintain an optimal balance between etching quality and processing efficiency; and through systematic testing, 15 repetitions were determined to be the most suitable count. This parameter combination successfully achieved the required equilibrium between etching effectiveness, dimensional accuracy, and operational productivity. The comparison between before and after optimization is shown in Figure 20. A and D.

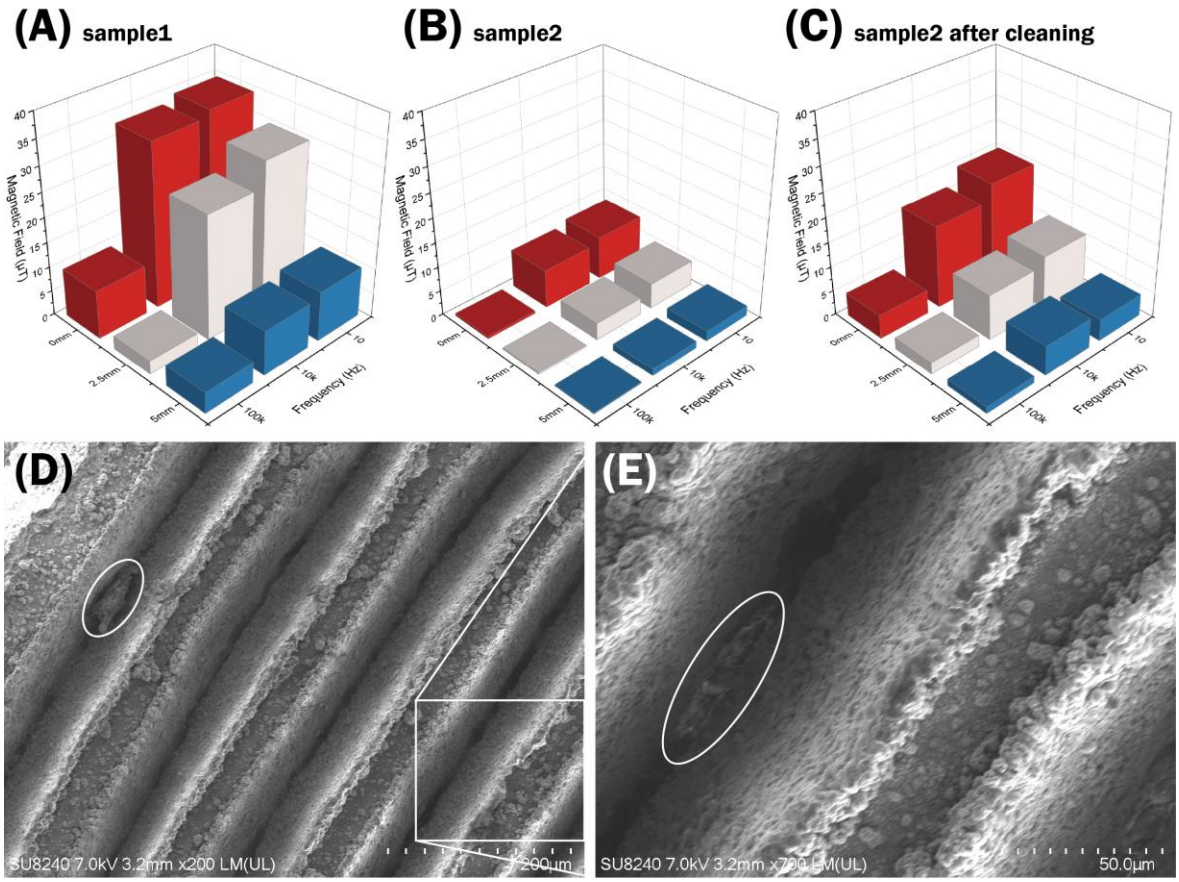

Figure 21. (**A**)-(**C**) Magnetic field measurement results of two sample 1, 2 and sample 2 after acetone-cleaning. (**D**)-(**E**) The SEM picture of coil containing cooper debris that shot the coil.

Multiple sample coils were fabricated using the parameters, and their magnetic fields were measured using TMR sensors. Under 100mA 10Hz, 10kHz, and 100kHz current, using a tunnel magnetoresistance (TMR) sensor (TMR2104, sensitivity 0.0445 mV/nT) 1cm above the coil moving from the coil center (0 mm) to its outer edge (5 mm) yielding the results in Figure 21. A-C. The measurements revealed inconsistencies between individual coils, with significantly lower field strengths in some samples (Figure 21. B). Subsequent examination

via scanning electron microscope (SEM) demonstrated that while the optimized etching process successfully removed most of the Cu material, it simultaneously generated numerous microscopic Cu debris particles that remained trapped within the inter-wire gaps as circled in Figure 21 D and E. These conductive remnants created unintended short-circuiting between adjacent windings, effectively reducing the number of active turns and consequently diminishing the magnetic field output. An attempt was made to eliminate the debris through acetone cleaning, however, as presented in Figure 21. C, although this increased the performance, it was not as high quality as in Figure 21. A, showing this method ineffective. It was, then, ultimately determined that this manufacturing approach may not be suitable to produce this coil design.

4.1.3 Photolithography

Given the limitations identified in the laser cutting approach, we transitioned to a cleanroom-based fabrication method utilizing photolithography and electroplating to produce thick planar coils. The most significant technical challenge in this alternative method involves optimizing the processing steps for ultra-thick photoresist layers. While conventional photoresists, including specialized thick-film materials like SU-8 and HD-4110, typically struggle to achieve thicknesses beyond 25μm. This necessitated a comprehensive re-evaluation of both photoresist materials and processing parameters. The optimization process focused on four interdependent variables: spin-coating speed, which directly controls photoresist thickness and uniformity; soft-baking conditions that govern solvent evaporation and film stability; exposure duration critical for achieving complete cross-linking throughout the thick resist layer; and development time that determines feature definition quality. Each parameter requires precise calibration not only individually but also in relation to the others, as they collectively influence the final resist profile. Through comprehensive investigation, we identified AZ6090 photoresist as particularly suitable for this application due to its capability of achieving 90μm thickness while maintaining properties like the well-characterized AZ4562 photoresist. The following sections will review how to find the most suitable the processing parameters for this photoresist, which also could be a case for general ultra-thick photoresist optimization.

4.1.3.1.1 1st Round Optimization

Among the various process parameters involved, exposure time was identified as the most critical factor governing photoresist patterning quality. Insufficient exposure prevents complete photochemical conversion of the resist, leading to development failure, while excessive exposure causes unwanted dissolution of protected areas and subsequent feature distortion. To systematically optimize this key parameter, an initial screening experiment was

conducted using strategically selected exposure durations of 10s, 20s, 40s, and 60s. This wide interval approach enabled efficient identification of the approximate optimal range. All other process conditions were carefully controlled: spin coating at 1000 rpm for 30 seconds, a precisely programmed soft bake with gradual temperature ramping from 60°C to 105°C over 30 minutes (increasing 15°C every 10 minutes), and after exposure, developing in MF319 for 3 minutes.

The resulting patterns, shown in Figure 22. A-D, demonstrate distinct quality variations across the tested exposure spectrum. The 10s condition showed very vague development with residual resist, while 40s and 60s exposures exhibited noticeable feature degradation. 20s gives the best results. After measuring the thickness variation of the resist (Figure 22 E), as there is still no flat wafer surface occur and the expected thickness should be 80-90μm, while the developed thickness is 60 μm only, the resist is still not completely removed. This might result from under-development or suggest the optimal exposure likely lies within 20s to 40s.

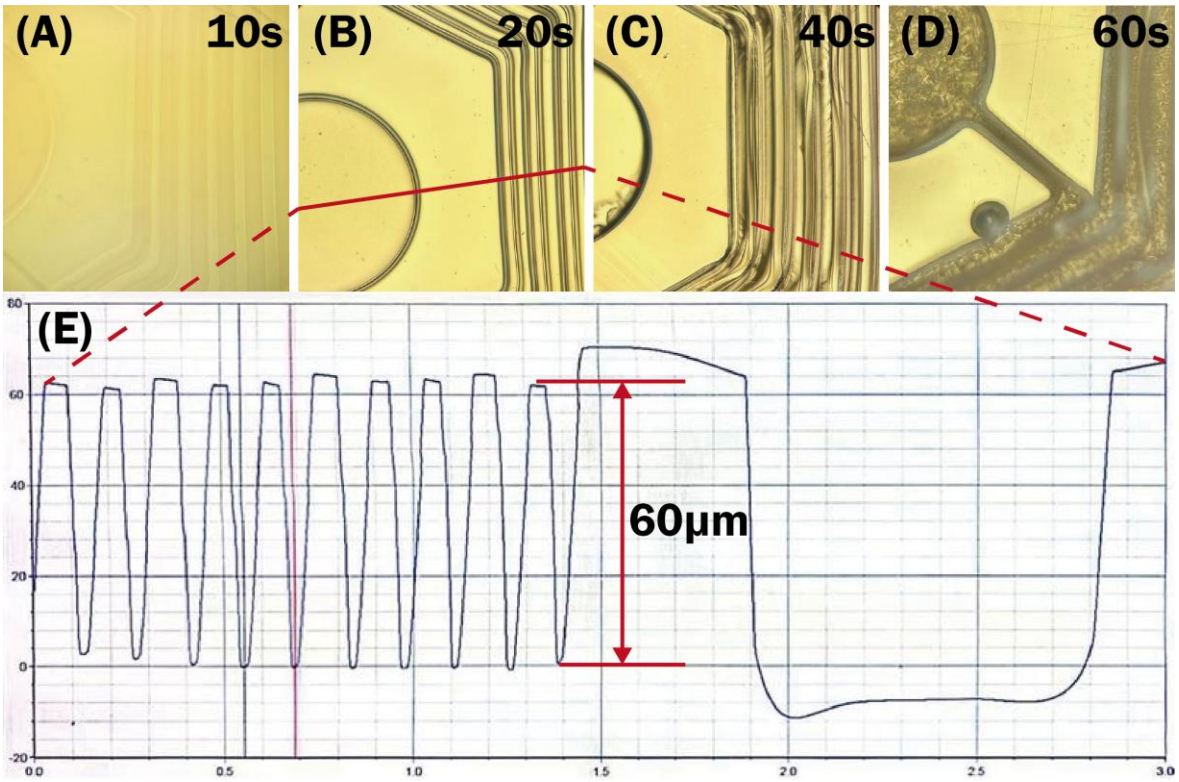

Figure 22. (**A**)-(**D**) Samples after development with 10s 20s 40s and 60s exposure. (**E**) The thickness measurement of 20s sample.

4.1.3.1.2 2nd Round Optimization

To rule out the possibility of photoresist residue caused by insufficient development time, we tested the 20s-exposed samples with different development durations of 5, 7, and 10 minutes. The results are shown in Figure 23. Optical microscopy examination revealed no significant

deformation. However, thickness measurements of the photoresist demonstrated that the 5-minute development yielded the optimal outcome. The smooth surface at the pad areas (wafer surface) indicated complete photoresist removal, while the jagged profiles at the bottom of coil trenches, elevated above the wafer surface, suggested incomplete resist removal - characteristic of underdevelopment. In the end there was still 15 µm or so of photoresist left.

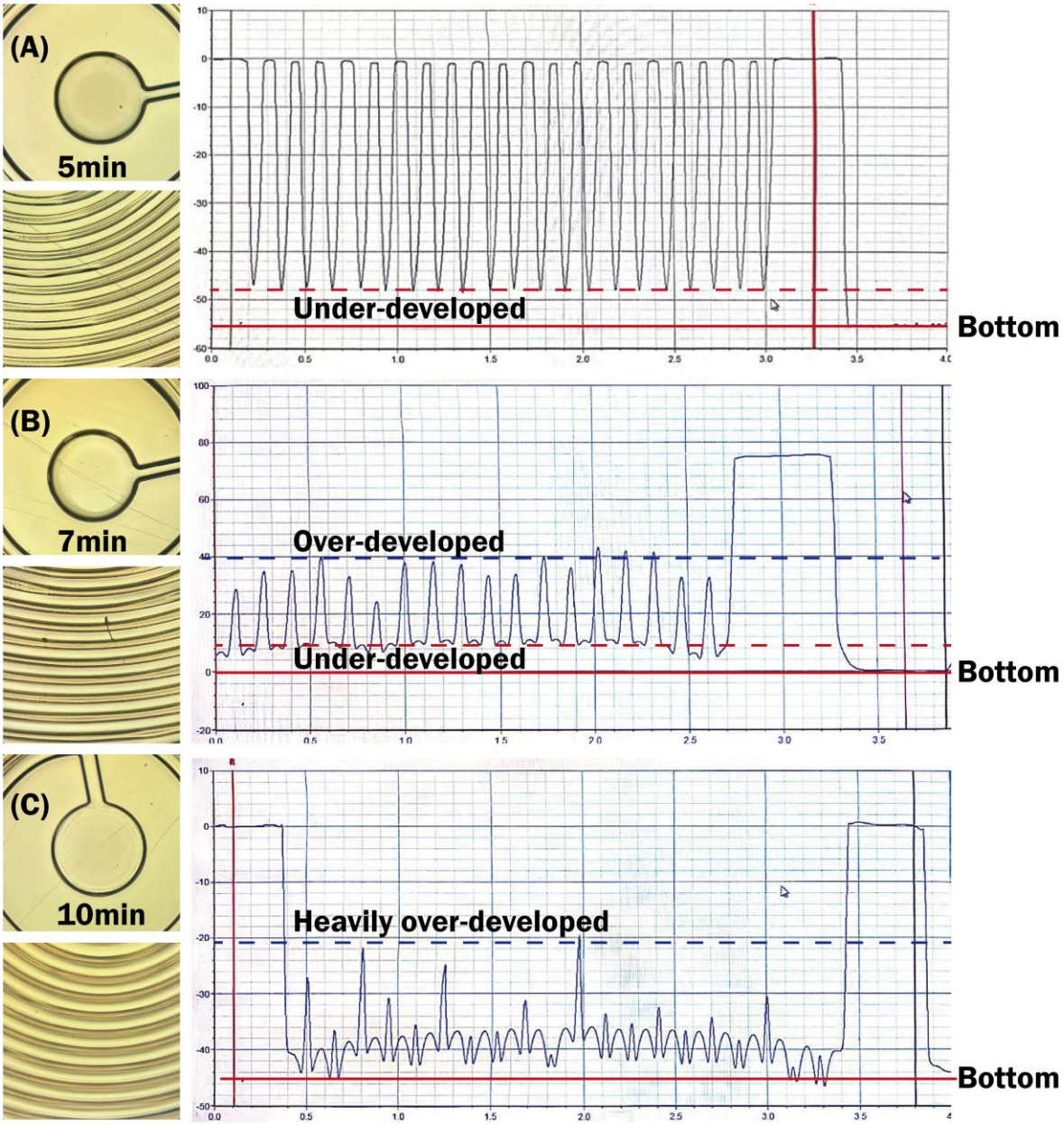

Figure 23. (**A**)-(**C**) Picture results and thickness measurements of samples with 5-, 7-, and 10-min development.

In contrast, the 7-minute development showed clear signs of overdevelopment. The upper portions of photoresist that should have remained in the coil trenches were eroded, while the bottom portions still exhibited underdevelopment like the 5-minute results. This phenomenon likely indicates that the original 20-second exposure duration remained insufficient for complete photochemical conversion throughout the entire resist thickness. In 10-minute

sample, this phenomenon is more serious. The measurements suggest the need for increase of exposure time.

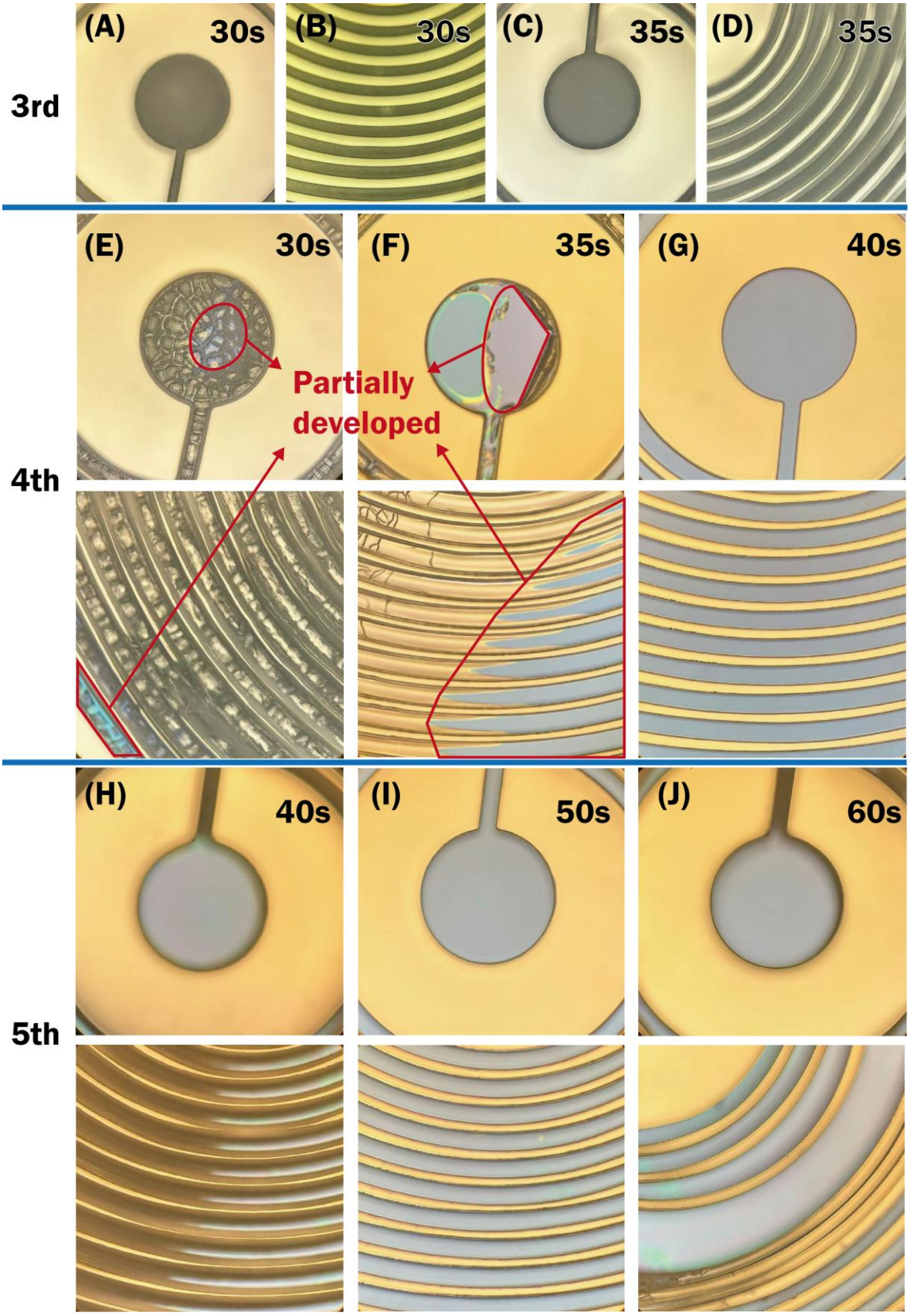

Figure 24. (**A**)-(**D**) 3rd round results of sample with 30s and 35s exposure. (**E**)-(**G**) 4th round results of sample with 30s, 35s, and 40s exposure. (**H**)-(**J**) 5th round results of sample with 40s, 50s, and 60s exposure.

4.1.3.1.3 3rd Round Optimization

To enhance observation clarity, the original gold-coated Si wafers were replaced with Si dioxide substrates, which exhibit a characteristic blue-purple coloration. This modification creates a distinct visual contrast between fully developed areas (revealing the substrate color) and regions with residual photoresist. Using identical spin-coating and soft-bake parameters as the first-round experiment, new samples were exposed for 30s and 35s followed by 5-minute development. As shown in Figure 24. A-D, the 30s-exposed sample showed faint substrate coloration indicating partial but incomplete resist removal, while the 35s exposure resulted in clear overdevelopment. This outcome suggests none of the previously discussed factor is the reason for this underdevelopment. A possible explanation is the soft-bake temperature profile, where insufficient solvent evaporation from the photoresist may have compromised its structural stability during subsequent process. The incomplete solvent removal likely caused the resist to swell or deform upon contact with the developer solution, preventing consistent pattern transfer across the entire thickness.

4.1.3.1.4 4th Round Optimization

The soft-baking process was modified by extending the duration to approximately 40 minutes while maintaining a gradual temperature increase. The revised protocol began at 60°C with incremental 10°C rises every 5 minutes until reaching 130°C, which was maintained until completion. To enhance solvent evaporation efficiency, the spin-coating speed was increased to 1500 rpm, resulting in a reduced photoresist thickness to approximately 60μm.

The samples were tested under three different exposure times: 30s, 35s, and 40s, each followed by a 5-minute development. As illustrated in Figure 24. E-G, the 40s exposure yielded optimal results, while both 30s and 35s exposures achieved partial development success. This success results from thinner resist thickness around this area, which is normal in small samples. Notably, the unremoved photoresist in the 30s and 35s samples exhibited cracking patterns, potentially attributing to the much higher soft-baking temperature. Building upon these successful outcomes, the subsequent experimental phase will employ a 1000 rpm spin-coating speed to achieve a thicker photoresist layer of about 80μm.

4.1.3.1.5 5th Round Optimization

To accommodate the increased photoresist thickness, the exposure time was correspondingly extended to 40s, 50s, and 60s. The soft-baking protocol was slightly modified to initiate at 55°C, followed by incremental 10°C increases every 5 minutes until reaching 125°C, which was maintained until completion. With a constant 5-minute development time, the results are shown in Figure 24. H-J. The 50s exposure yielded optimal patterning quality, while the 40s

samples exhibited underdevelopment. The 60s exposure, likely due to excessive exposure energy combined with the 5-minute development duration, resulted in poor photoresist adhesion to the wafer surface (Figure 24. J).

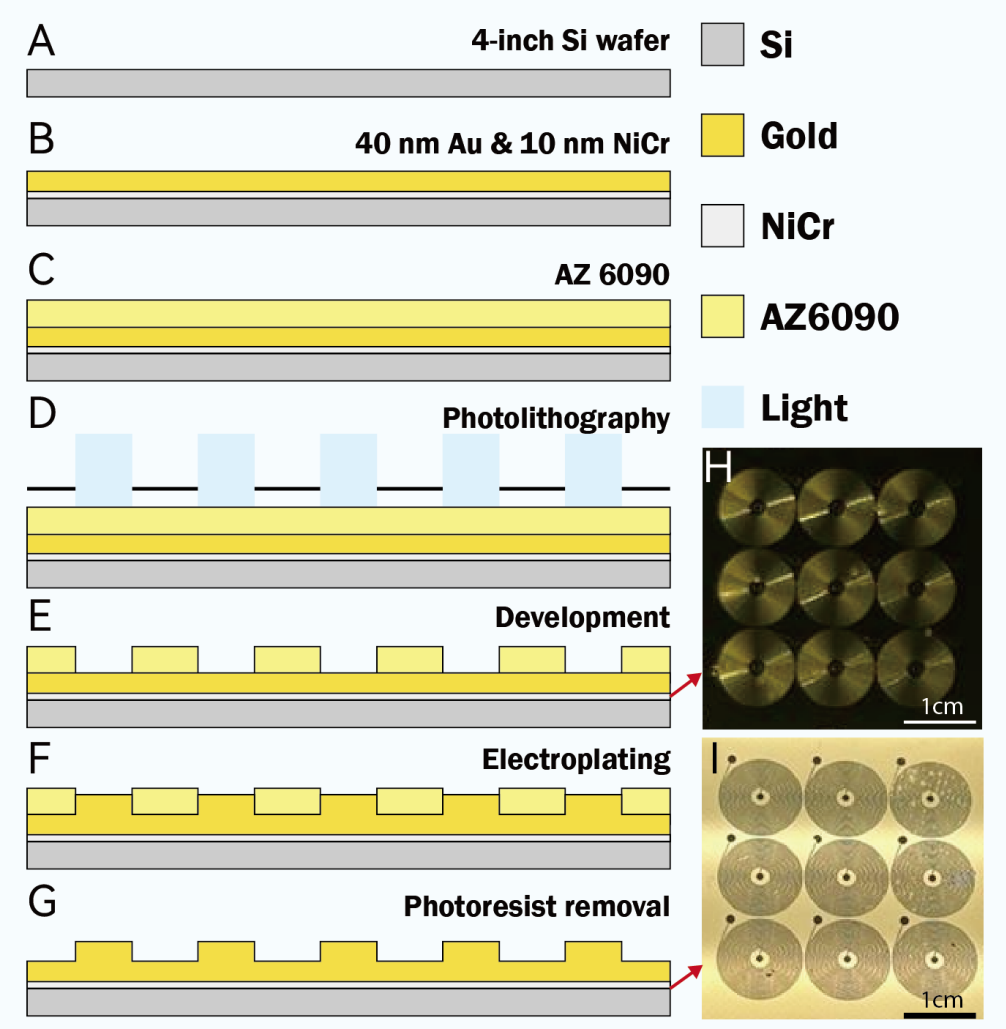

Figure 25. **A-G** The schematic fabrication process of cleanroom strategies. **H** Samples after development. **I** Samples after photoresist removal after electroplating.

4.1.3.1.6 Final Recipe

Based on these findings, the optimized fabrication process (Figure 25. A-G) for the 1000 rpm spin-coating strategy (80µm thickness) are determined to be:

1. Prepare the substrate. Deposit Gold seed layer (20-40 nm Au, on 10 nm NiCr).
2. Pour the resist on the sample slowly.
3. Spinning with 1000rpm for 30s. (*To avoid bubbles, the baking temperature should increase slowly to let the solvent evaporate gradually. Start with 55°C, increase 10°C every 10min until 125°C and keep this temperature with 5 min.)
4. Clean the edge and back of the sample with acetone-dipped cotton bud.
5. Soft bake on a hotplate.

6. Expose using soft contact mod for 50s.
7. Post-exposure-bake on a hotplate at 100°C for 1-2 min.
8. Develop in MIF319 for 5min according to current results we have.

4.1.3.1.7 Electroplating

After obtaining the optimized lithography parameters, batch production of samples was attempted for electroplating. However, the electroplating results proved unsatisfactory, revealing several critical limitations:

1) **Metal Adhesion Failure**: The deposited metal exhibited poor adhesion stability. During post-processing steps like photoresist removal, rinsing, and drying, the metal frequently detached from the metal or substrate, creating lower thickness and open circuits that fail entire coils nonfunctional. Figure 26, A-C illustrate three types of adhesion condition. In B and C, the thickness measurement results are like Figure 26. D and E. In D, the metal detached from the metal under it, while in E, the metal almost detached directly from the substrate surface.

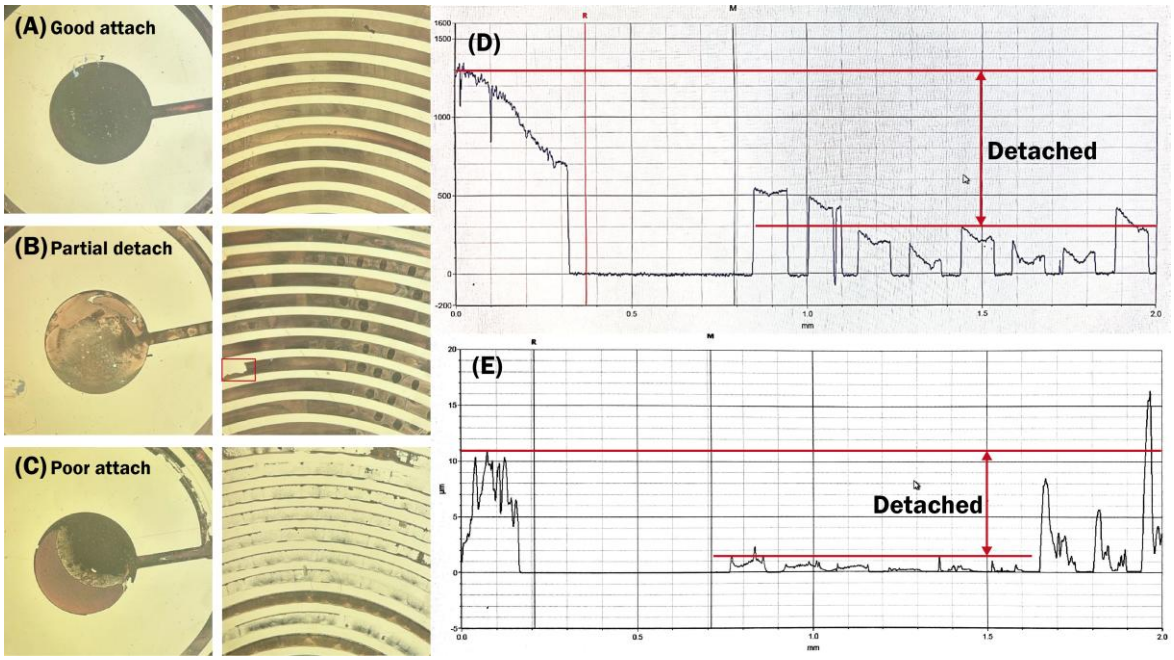

Figure 26. (**A**)-(**C**) Samples with different attach quality after photoresist removal. (**D**)-(**E**) Two thickness measurement results showing the detach of metal.

2) **Photoresist Degradation During Plating**: The extended immersion in warm ionic solutions (required for electroplating) combined with mechanical stresses from metal deposition caused detach of photoresist. As the resist barriers failed, the plated metal bridges formed continuous shorts between intended isolated features. Figure 27 exactly shows the situation. By comparing A and B, the deformation of resist is

obvious, and in D, after removing the resist, the metal connected clearly. Besides, E and F thickness measurements illustrate that although the bottom shows connections, the top part still isolated. It can be assumed that the resist partially peeled off from the wafer surface, which only make the bottom part connect. This phenomenon can also be observed in other relative successful samples like shown in Figure 28.

3) **Insufficient Thickness Achievement**: Even in relatively successful samples avoiding the above failures, the maximum achievable Au thickness (15-30μm, Figure 28) remained far the target ~80μm requirement.

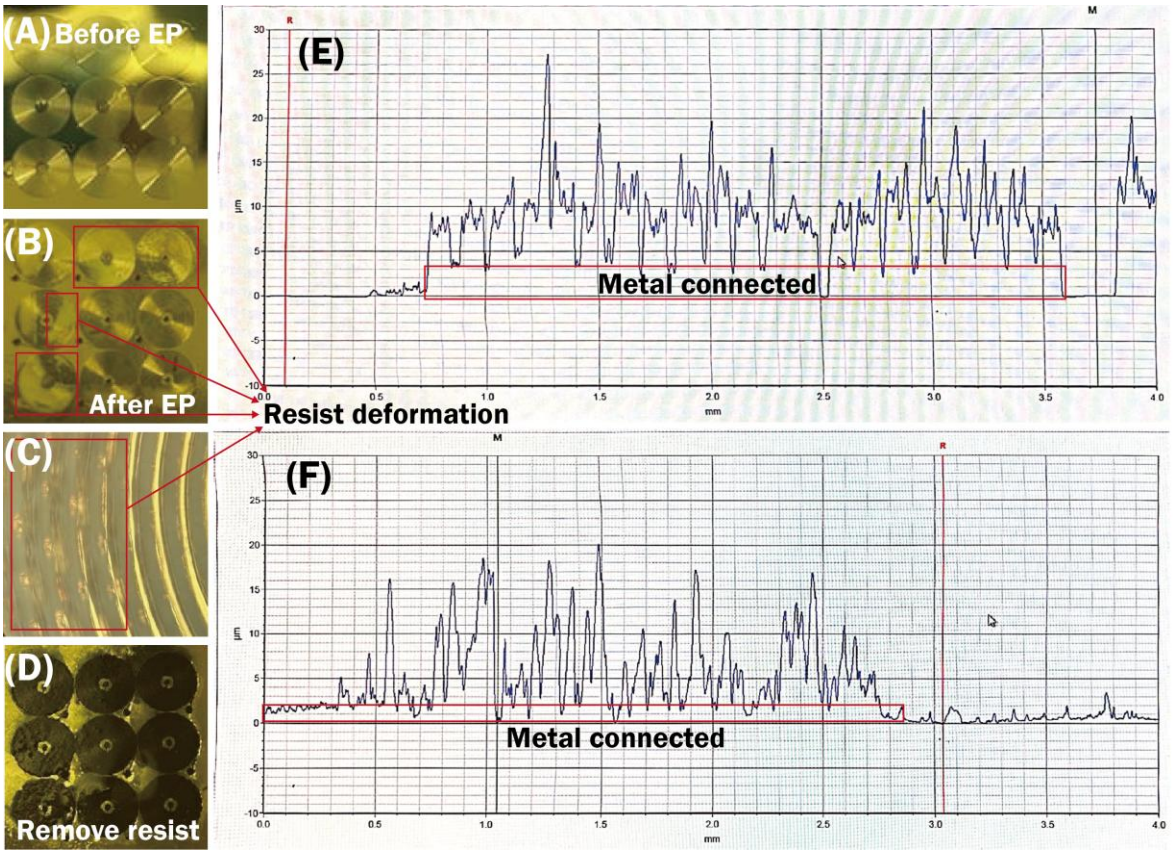

Figure 27. (**A**) Sample before electroplating. (**B**) Sample after electroplating. (**C**) Photoresist deformation under microscope. (**D**) Sample after photoresist removal. (**E**)-(**F**) Two thickness measurement results showing metal connections caused by photoresist deformation.

4) **Ununiformed metal growth**: There is a 2h-electroplated sample in Figure 28. A. The deposited metal surface is very fluctuated and rough. In another sample with longer 3h electroplating, the more exceeded part at the beginning will grow faster because it will have larger surface catching irons from the solvent which will lead to the results in Figure 28 B. This can also be found in Figure 26. E and Figure 27. E and F. The metal looks like mountains with different height will lead to poor electric properties of coils.

These fundamental limitations, encompassing adhesion chemistry, structural stability during processing, and thickness scalability, collectively demonstrate that this photolithography/electroplating approach cannot reliably produce high-performance coils at scale. Consequently, this fabrication route has been deemed unsuitable for the current coil design specifications.

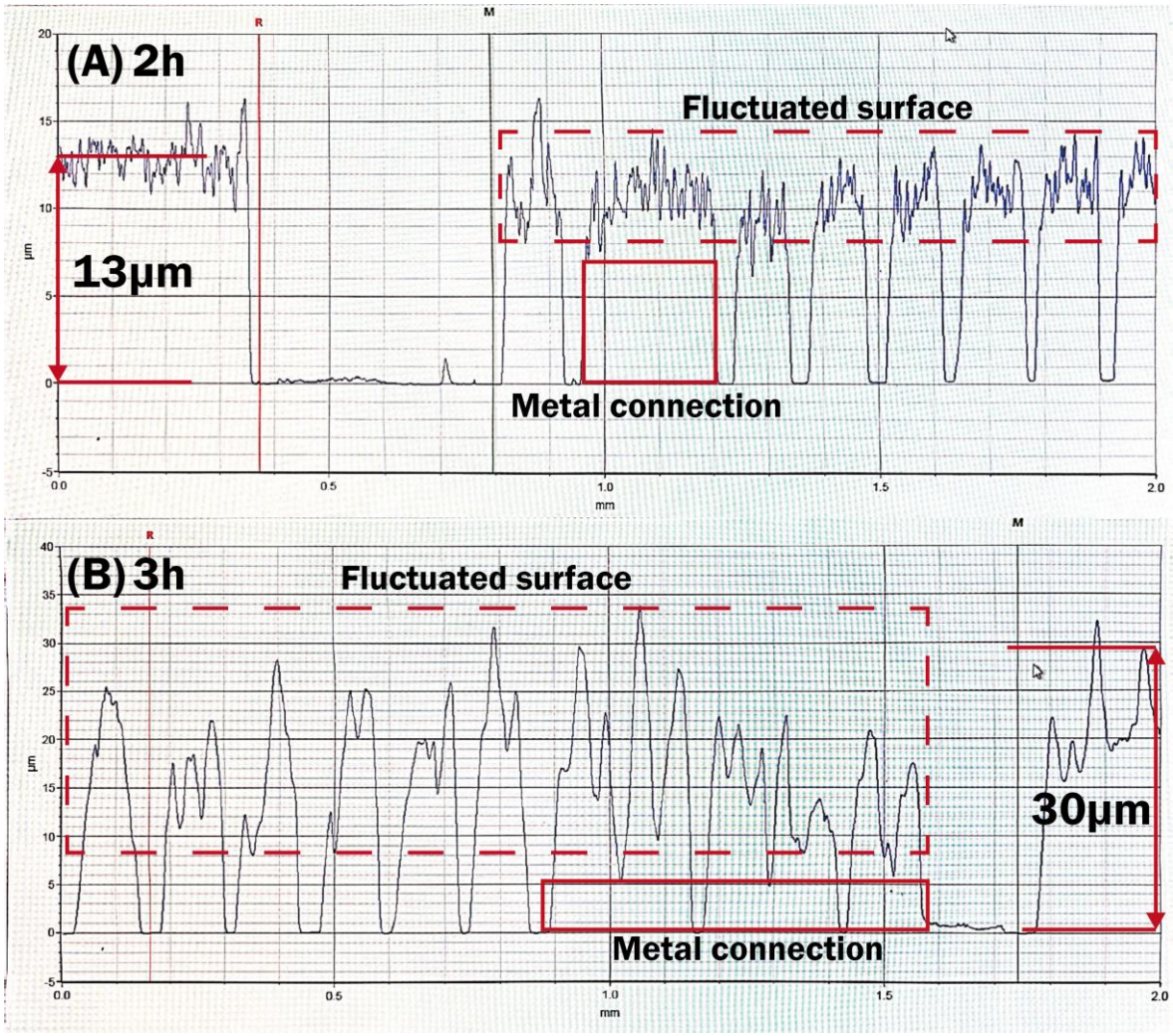

Figure 28. Two thickness measurement results of relatively well-electroplated samples with (**A**) 2-hour electroplating, and (**B**) 3-hour electroplating. Dashed boxes contain the fluctuated surfaced, and solid line boxes contain metal connection parts.

4.1.4 Craft Blade Cutter

Due to the fabrication defects identified in the previous two sections, the reliance on specialized environments such as cleanrooms, and the use of high-cost equipment, particularly considering that wearable devices have significantly lower requirements for materials and fabrication precision compared to implantable devices, here proposes an economical and efficient mini-coil production method: physical cutting. A comparison of consumption between the method with a conventional cleanroom photolithography fabrication process is given in Table 6.

Table 6. Comparison between cutter fabrication, laser fabrication and cleanroom photolithography fabrication method.

Property	Cleanroom fabrication	Lazer fabrication	Cutter fabrication
Fabrication Environment	Cleanroom	Cleanroom free	Cleanroom free
Equipment cost	Cleanroom, photolithography, deposition etc. ($1,000,000s level)	Laser equipment ($100,000s level)	Cutter ($100s level)
Material cost	Metal deposition ($10s / nm), photoresist ($100s / L)	Laser-processible substrate ($10-100s / slice)	PVC sheets & Metal tapes ($10s)
Fabrication Time scales	2-4 days / 1 wafer (10s – 100s of samples)	20-60 min / sample	5-10 seconds / sample
Processing Speeds	No (re-make photomask needed)	Yes (programable design)	Yes (programable design)
Risk	Toxic chemicals used (e.g. TMAH)	Laser hazard	Low risk
Resolution	100s nm - μm level	10s μm	100-150 μm

4.1.4.1 Design and Fabrication

To fit with this fabrication method, a design method based on Python programming (code is given in Appendix 7.3) with geometry variables is proposed: inner and outer radius (r_i and r_o), number of turns (n), and wire width (w) as shown in Figure 29 a. The fabrication process was done using a digital blade cutting machine (Silhouette Cameo Cut) as illustrated in Figure 29. This machine has a blade tip size of approximately 100 μm and a resolution of around 150 μm. As shown in Figure 29, conductive Al tape (60 μm thickness), was attached to flexible, thin, and transparent PVC sheets (80 μm thickness, A4 size: 154 mm × 242 mm), which was the substrate. Then cut the Al layer using the digital blade cutter to form the flexible coils. To ensure precise cutting, the Silhouette Studio software was used to adjust parameters including blade depth, cutting force, cutting speed, and the number of passes. The optimized software-settings included a blade depth of 3, a force of 24, and a speed of 3, as slower speeds and slightly higher forces were found to improve accuracy. Al was chosen for its availability and cost-effectiveness, but the technique can also be translated to other conductive metal foils, such as Cu. The parameters can be adjusted for thicker films to enable higher current capacities, by increasing the cutting force and number of passes, making the technique versatile for diverse applications in flexible electronics. Various coil configurations were fabricated, including different number of turns (5, 10, 15, Figure 30. d, e, f and Figure 29. a), and shapes (circular, rectangular, hexagonal, Figure 30. e, b, c, and Figure 29. b). Circular

coil is the most used design, while angles will bring more dynamic distribution patterns and two common polygon shapes (rectangular and pentagonal) are selected.

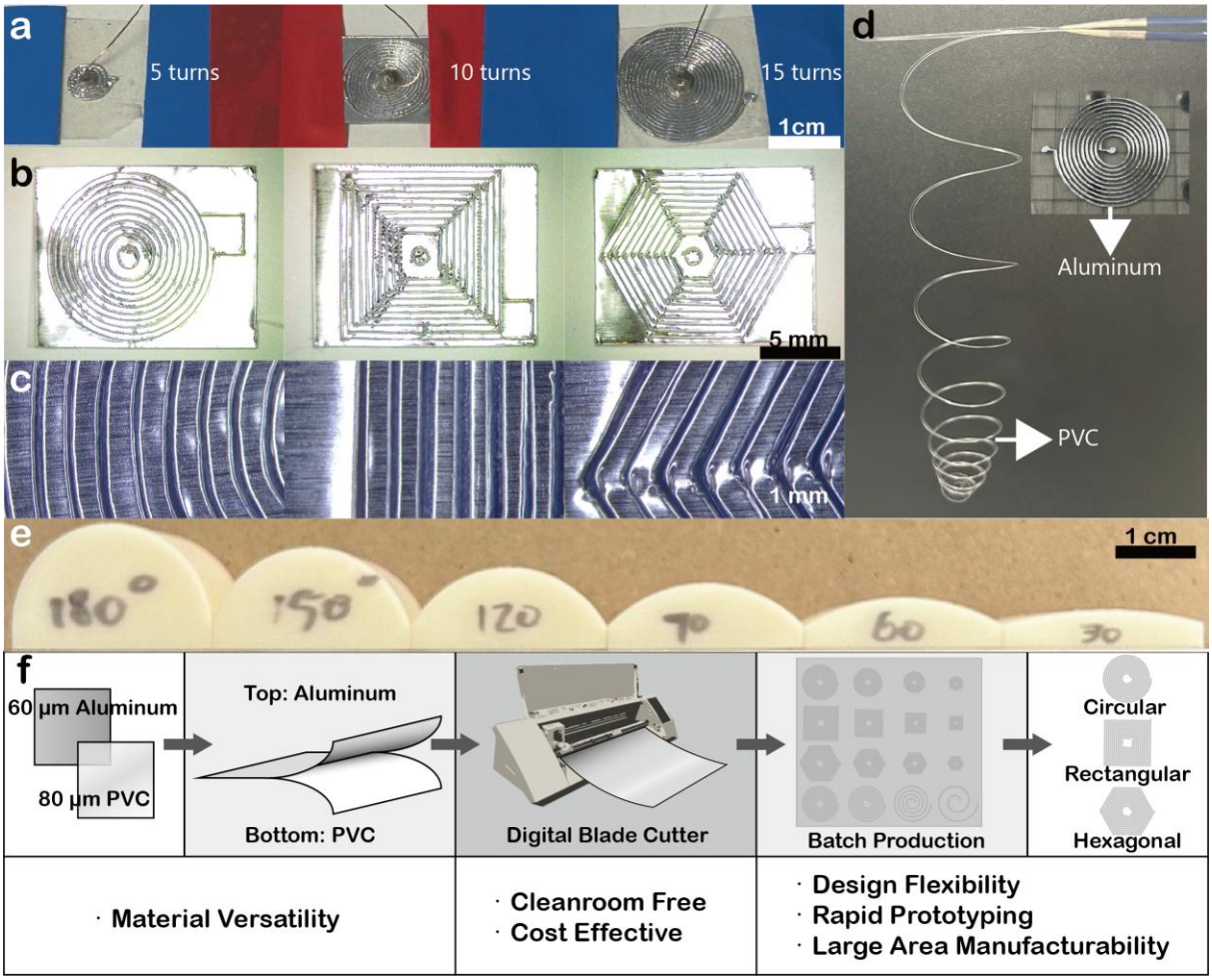

Figure 29. **a**) circular coil with 5, 10, and 15 turns, **b**) 10-turn coil with circular, rectangular, and hexagonal shapes, **c**) zoom-in microscope picture of cut edge from each shape coil, **d**) the first test of cutting with only PVC and only Aluminium. **e**) The arches with different angles. **f**) Fabrication process and advantages of this method.

In following sections, the inductance, resistance, and magnetic field strength for prototype (circular shape) coils with different turns were evaluated to determine the optimal number of turns first, and then coils with this number of turns were fabricated in three shapes: circular, rectangular, and hexagonal. The three coil shapes were then evaluated based on key performance metrics, including intrinsic parameters such as inductance, resistance, and factor and external characteristics, such as heat generated and magnetic field strength. The intrinsic parameters directly influence the electromagnetic behavior and efficiency of the coils. For instance, inductance determines the frequency response, particularly in the higher frequency of 10 kHz to 1 MHz range, which is critical for applications like magnetic hyperthermia and wireless power transfer [317, 318].The Q-factor reflects the coil's efficiency and energy loss rate, while resistance impacts energy dissipation and heat generation. External metrics, such as temperature rise during operation and magnetic field strength, are critical for wearable

applications to ensure safety, stability, and functionality. Since wearable coils often come into direct contact with the skin, temperature control is particularly crucial, while maintaining a stable magnetic field strength is essential for medical applications. Additionally, given that wearable devices frequently undergo bending and flexing during use, the coils were tested under various bending angles (on 3D printed arch with 30° to 180°) and repeated bending cycles (up to 1,000 cycles). These tests simulated real-world conditions to assess the durability and reliability of the coils. All these tests are performed by 3 repetitive experiments on 3 samples randomly selected from different batches to see how their average acts.

As a result, the measurements focused on five key areas: optimizing the number of turns, coil performance under different bending angles, performance after multiple bending cycles, temperature rise under different current inputs, and magnetic field strength across varying current inputs. To ensure reliability, all measurements were averaged across three samples and were used to validate the proposed coil design while also offering valuable insights for future optimization and practical applications.

4.1.4.2 Optimization of the Number of Turns

Circular coils with 5, 10, and 15 turns, all featuring the same line width and spacing, were fabricated and evaluated. Three key parameters were analyzed and shown in Figure 30. g, h, and i: inductance (averaged over the 10 kHz–1 MHz frequency range), serial resistance (measured under DC conditions), and magnetic field strength at the coil center (measured with a 10 Hz, 100 mA sinusoidal input).

As shown in Figure 30. g, the average inductance increased with the number of turns but only modestly, rising from approximately 6 μH for the 5-turn coil to 7 μH for the 15-turn coil across the frequency range. Resistance, on the other hand, rose sharply with additional turns due to the linear growth in the outer diameter and the progressively greater wire length required for each subsequent turn (Figure 30. h). Magnetic field strength at the coil center also increased with more turns, but the incremental gain diminished as the number of turns grew (Figure 30. i). This diminishing return occurs because turns farther from the center contribute much less effectively to the central magnetic field, limiting the overall increase. Therefore, the 10-turn coil emerged as the optimal configuration for wearable applications. While inductance varied only slightly, resistance and magnetic field strength were the decisive factors. The 10-turn coil strikes a balance between strong magnetic field generation and manageable resistive heat, making it the most suitable choice for further testing and analysis of different coil shapes.

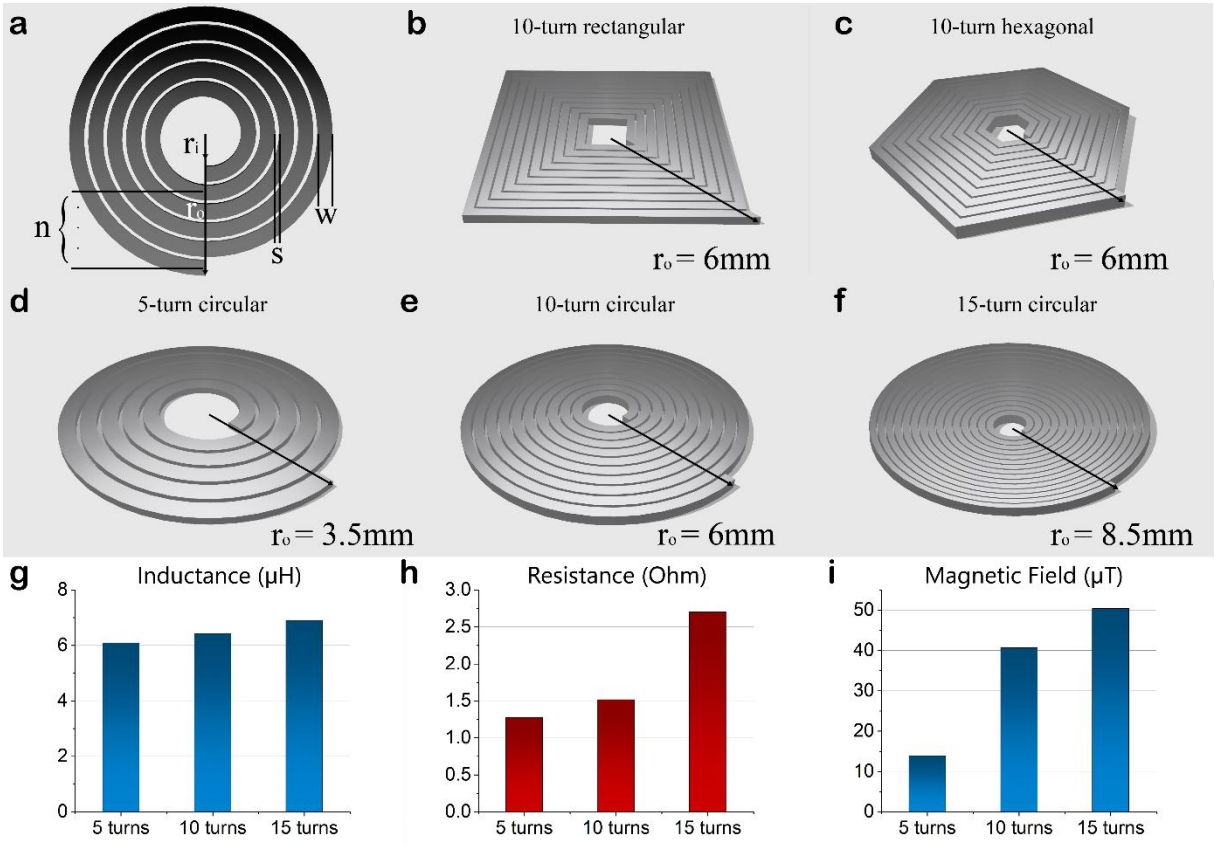

Figure 30. **a**) The editable parameters of a coil. 3D schematic diagram of a **b**) 10-turn rectangular coil, **c**) 10-turn hexagonal coil, **d**) 5-turn circular coil, **e**) 10-turn circular coil, **f**) 15-turn circular coil. **g**) The average inductance value in 10 kHz-1 MHz band of 5, 10, 15-turn circular coil. **h**) The serial resistance of 5, 10, 15-turn circular coil. **i**) The magnetic field of 5, 10, 15-turn circular coil under 10 Hz 100 mA current input.

4.1.4.3 Coil Characteristics at Different Bending Angles

For wearable applications, it is essential to evaluate coil performance under varying degrees of bending, as these devices must adapt to the contours of the body. To simulate such conditions, coils were taped onto 3D-printed modules with varying curvatures (Figure 29. e), representing potential use cases from the wrist to the thigh. The performance of three coil shapes—circular, rectangular, and hexagonal—was analyzed under different bending angles. Key parameters, including inductance, quality factor, and resistance, were measured, and are presented in Figure 31.

Figure 31. a-c illustrates the variation of inductance with frequency (10 kHz to 1 MHz). Across all three shapes, inductance remained relatively consistent under bending. For angles 150°, the inductance showed a sharp increase in the lower frequency range (10 kHz–100 kHz), stabilizing at 12–14 μH above 100 kHz. Beyond 150°, the inductance curves were steady, with minimal deviation, indicating high stability despite increased curvature. Figure 31.d-f highlights the Q factor variation with frequency. The Q factor increased with frequency,

characteristic of inductors with low parasitic resistance. At bending angles 150°, a noticeable dip in the Q factor was observed between 15 kHz and 30 kHz, likely due to resonance caused by parasitic capacitance. As the bending angle increased, the effective inductance increased, shifting the resonant frequency lower and increasing the dip's impact. Angles exceeding 150°, resulted in a smoother Q factor curve.

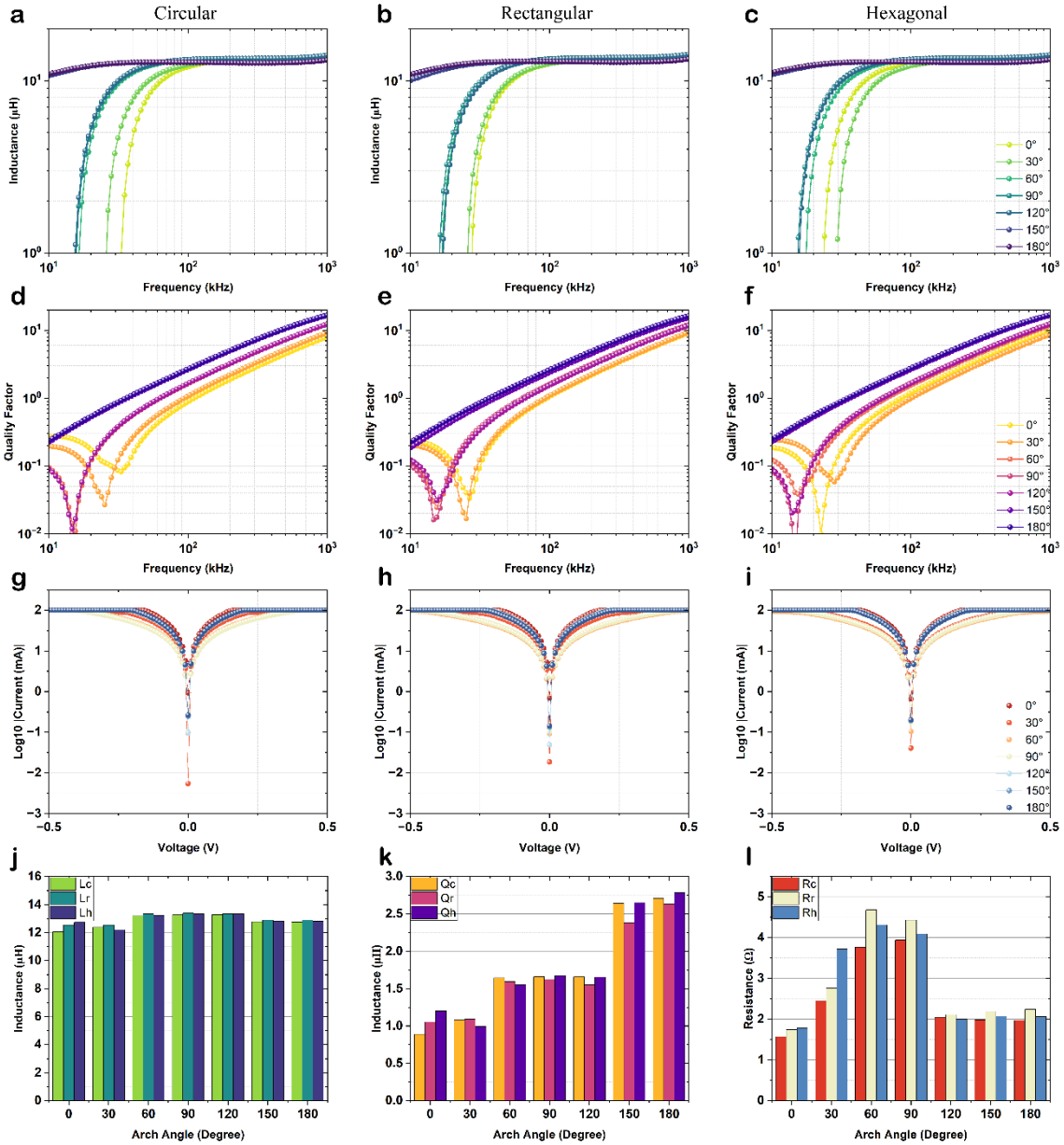

Figure 31. The coil characteristics under different bending angle. **a**) - **c**) Inductance value of circular, rectangular, and hexagonal coil over 10kHz – 1MHz. **d**) - **f**) Quality factor of circular, rectangular, and hexagonal coil over 10kHz – 1MHz. **g**) - **i**) I-V curve of circular, rectangular, and hexagonal coil. **j**) Inductance value of circular, rectangular, and hexagonal coil at 100 kHz. **k**) Quality factor of circular, rectangular, and hexagonal coil at. **l**) Serial resistance of circular, rectangular, and hexagonal coil.

Given the significance of 100 kHz for applications like wireless power transfer, Figure 31. j-l compares the inductance and Q factor for each shape at this frequency under different bending angles. Inductance remained stable across angles for all shapes, with the rectangular

coil (Lr) showing slightly higher values than the circular (Lc) and hexagonal (Lh) coils. In terms of Q factor, all shapes displayed a consistent trend of improvement with larger bending angles. However, the rectangular coil (Qr) typically exhibited a marginally lower Q factor associated to its higher resistance.

Figure 31.g-i show the current-voltage (I-V) responses and resistance values under DC input across bending angles. The I-V curves were symmetrical, with moderate bending angles (60°–90°) exhibiting broader current ranges. Resistance values varied significantly with bending, peaking at approximately 4.0–4.5 Ω for moderate angles, more than double the flat-state resistance (0°). The rectangular coil consistently exhibited resistance values 5–10% higher than the other shapes, correlating with its slightly lower Q factor despite its higher inductance. Overall, the inductance of the coils remained stable across all bending conditions, while the Q factor improved with larger angles, and the resistance exhibited the most variation, peaking at moderate bending angles. Among the three shapes, the rectangular coil demonstrated the highest inductance but faced trade-offs in Q factor due to increased resistance. These results confirm the robustness of the coils under bending conditions and their suitability for wearable applications.

4.1.4.4 Coil Characteristics after Different Bending Cycles

In wearable applications, devices are subject to repeated folding due to the wearer's movements, making it critical to understand the impact of these bending cycles on performance and durability. To simulate such conditions, electrical characteristics were recorded after every 100 times bending until 1,000 bending cycles for circular, rectangular, and hexagonal coil shapes. Each bending cycle began with the coil in a flat state, followed by bending to a 180-degree arch, and returning to the flat state. Key metrics—inductance, quality factor, and resistance—are presented in Figure 32.

Figure 32.a-c illustrates the inductance variation with frequency (10 kHz to 100 kHz) across different bending cycles. All coil shapes exhibited similar frequency response, with inductance values decreasing slightly as frequency increased. Initially ranging from 7.0–7.5 µH at lower frequencies, inductance dropped to 5.5–6.0 µH at higher frequencies. Repeated bending cycles caused a gradual decrease in inductance, with reductions of approximately 0.7 µH for circular coils, 0.4 µH for rectangular coils, and 0.5 µH for hexagonal coils. The circular coil exhibited the most pronounced decline. Figure 32.d-f shows the variation in the quality factor with frequency for the three coil shapes under different bending cycles. The

quality factor increased with frequency for all shapes. The quality factor improved during first 200–300 cycles.

Figure 32.g-i depict the current-voltage (I-V) relationships and resistance values for the three coil shapes under different bending cycles. The resistance value exhibited minor fluctuations, remaining within 1.5 to 2.0 Ω across all cycles. Among the three shapes, the rectangular coil demonstrated the most stable resistance, while the circular and hexagonal coils showed slightly greater variations.

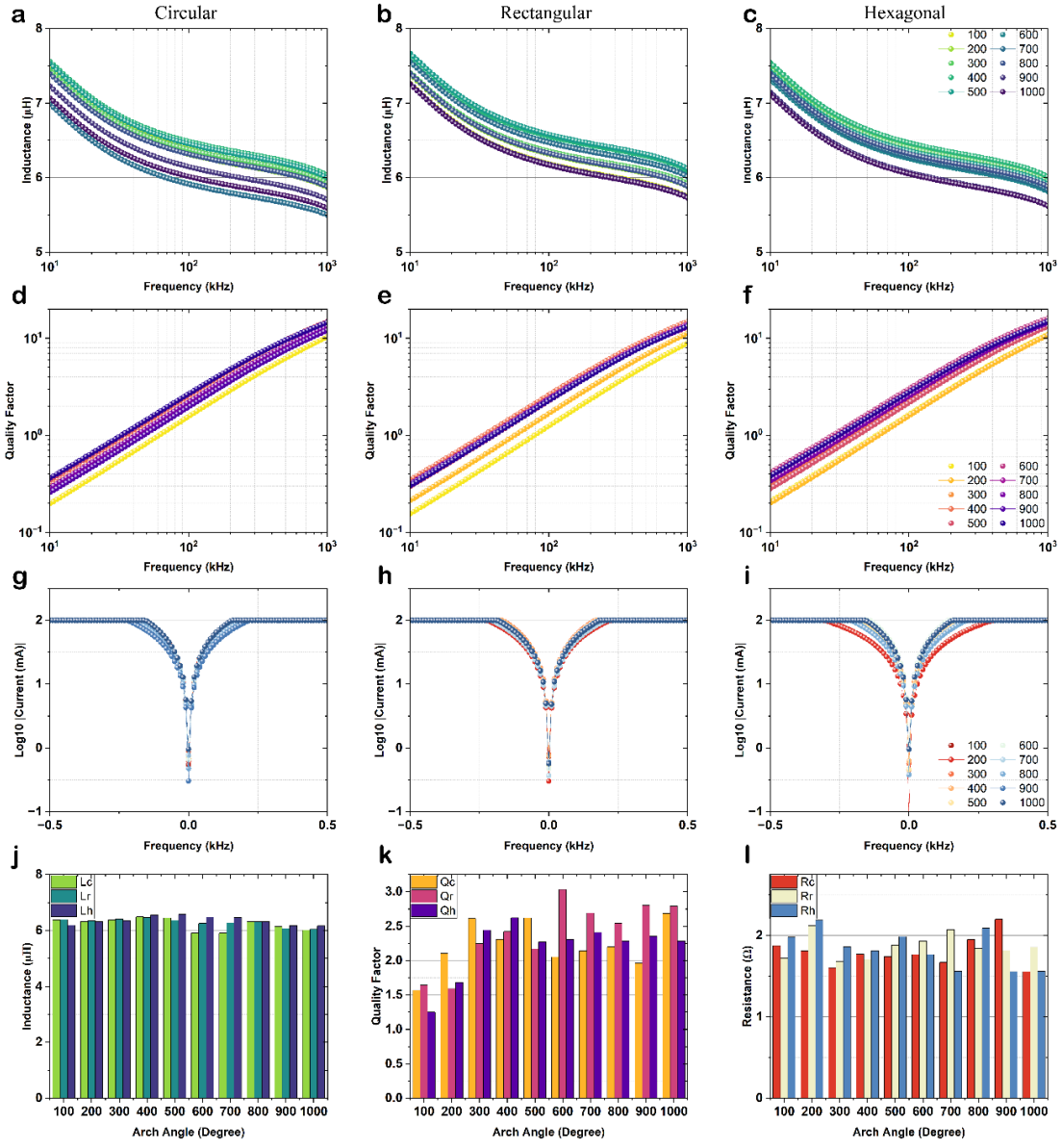

Figure 32. The coil characteristics under different bending cycles. **a**) - **c**) Inductance value of circular, rectangular, and hexagonal coil over 10kHz – 1MHz. **d**) - **f**) Quality factor of circular, rectangular, and hexagonal coil over 10kHz – 1MHz. **g**) - **i**) I-V curve of circular, rectangular, and hexagonal coil. **j**) Inductance value of circular, rectangular, and hexagonal coil at 100kHz. **k**) Quality factor of circular, rectangular, and hexagonal coil at. **l**) Serial resistance of circular, rectangular, and hexagonal coil.

At 100 kHz, the electrical characteristics of the coils revealed minimal differences in inductance across the three shapes. Inductance showed a slight initial increase, reaching approximately 6.5 μH, before gradually declining after 500 cycles and stabilizing around 6.0 μH. The quality factor exhibited an initial rise from 1.5 to 2.25 within the first 300 cycles. Beyond 400 cycles, different trends emerged: the circular coil's quality factor decreased slightly to about 2.0, the rectangular coil rose above 2.5, peaking at 3.0 around 600 cycles, and the hexagonal coil stabilized near 2.25 with minor oscillations.

Compared to the newly manufactured coils described in previous section, the inductance initially dropped significantly, from 12 μH to 7.5 μH within the first 100 cycles but is comparable to the result in number of turn optimization and remained stable and consistent through 1,000 cycles. The quality factor not only exceeded its initial value under unbent conditions but also improved steadily with repeated cycles, likely due to changes in resistance and parasitic capacitance effects. Compared to the results in Section 3.2, repeated bending cycles may enhance the coil's performance within this frequency range by mitigating resonant effects. Resistance showed minimal variation and stayed comparable to that of the newly manufactured coils, further confirming the durability of the designs.

Overall, these results suggest that the coils are highly reliable under repeated bending cycles, maintaining stable electrical characteristics with minimal degradation, making them suitable for long-term wearable applications.

4.1.4.5 Coil Application as Filter Component

To verify the stability of the coil inductance in the previous measurements, a high-pass filter was designed to reflect its characteristics as an inductor. The filter was designed and simulated using LTspice (The circuit included a 1 Ω source resistance in series with a 50 Ω resistor and an inductor of 7 μH with an internal resistance (Rs) of 2 Ω. AC sweep analysis was performed to evaluate frequency response characteristics. Figure 33. a illustrates the schematic of the, consisting of an input AC voltage source (Vs), a resistor (R) and an inductor (Ls) in series. The performance of the high-pass filter was evaluated using a SPICE-based simulator to analyze its frequency response. Two key parameters, gain (G) and cut-off frequency (fc), were considered critical for assessing filter performance.

$$G = 20log_{10}\left(\frac{Vo}{Vi}\right) \tag{4.1}$$

$$f_c = \frac{R}{2\pi L_s} \tag{4.2}$$

The hardware was tested with a function generator providing a sine wave input of 1V amplitude (2V peak-to-peak). The output was measured across a 10-turn circular coil connected in series with a 50 Ω resistor, using a digital storage oscilloscope. Figure 33. b and c compare the frequency response characteristics from simulations and experiments, plotting gain vs. frequency over a range of 10 kHz to 10 MHz.

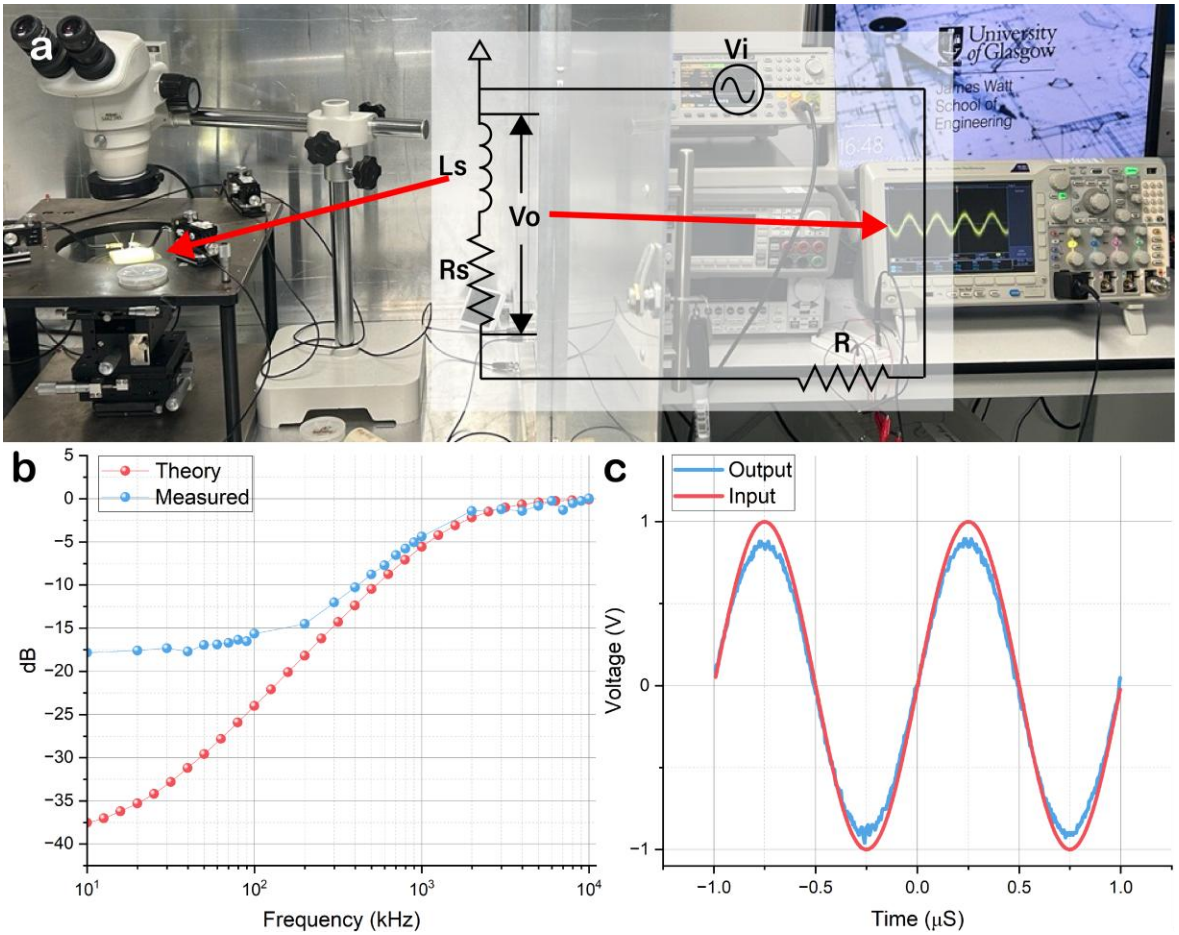

Figure 33. **a**) The experiment set up and corresponding equivalent circuit of RL filter. **b**) The frequency response curve from theoretic simulation and measured data. **c**) the theoretic input and recorded output voltage signal at 1MHz.

Approximately 0 dB at high frequencies in the MHz range was recorded. f_c is around 1.1 MHz, closely matching the theoretical value from Eq. 4.2. Experimental results closely aligned with theoretical simulations. The transfer function of the RL circuit was used to calculate the rise time of the high-pass filter, which was determined to be 23 ms, indicating a quick response to signal excitations. A slight deviation in gain at lower frequencies was observed, attributed to the white noise, parasitic capacitance, and inherent series resistance of the mini-coil, as discussed in previous sections.

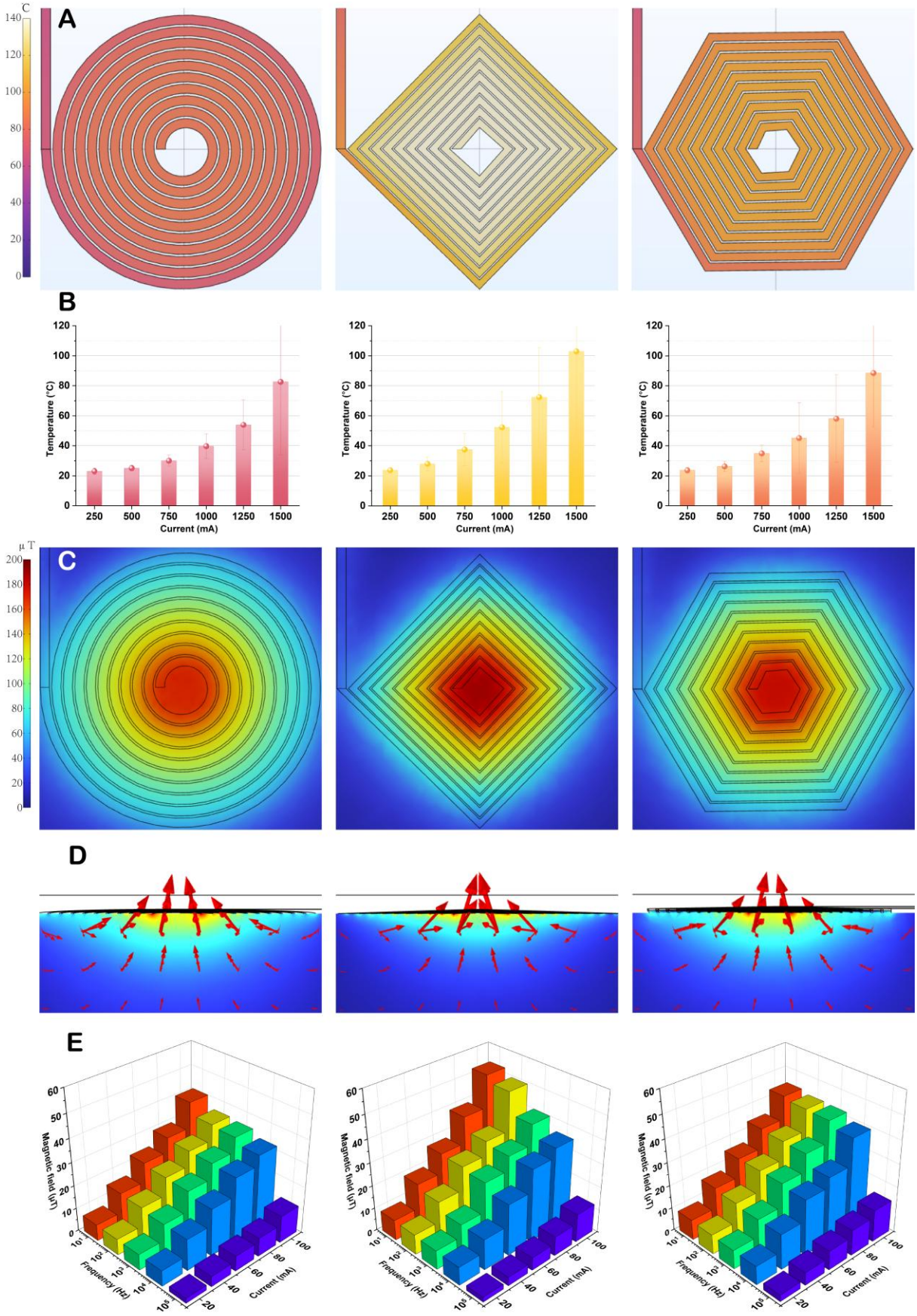

Figure 34. **A**) The surface temperature distribution in COMSOL with 1.5 A current input **B**) The measured temperature in IR camera **C**) The magnetic field distribution at plane 4 mm above coil. **D**) The magnetic field distribution in human tissue **E**) The measured magnetic field strength by TMR sensor under different current input.

4.1.4.6 *Temperature Response to Current*

The temperature response is a critical metric for wearable devices due to its direct impact on safety. This study investigated the thermal performance of the coils under extreme conditions, particularly resistive heating when the input current exceeded 1 A. Figure 34. A present COMSOL simulations of surface temperature distribution for the three coil shapes under 1.5A and for 3seconds. Across all shapes, the highest temperatures were observed near the center of the coils, reflecting the concentration of current density. The circular coil demonstrated the lowest surface temperature, ranging from 70°C to 80°C, followed by the hexagonal coil for temperatures between 90°C to 110°C. The rectangular coil exhibited the highest temperature, ranging from 120°C to 140°C, likely due to its higher resistance.

Figure 34. B show experimental temperature measurements using an infrared (IR) camera for different current levels. The temperature increased consistently with higher input currents across all coil shapes. The experimental results closely aligned with the simulations: the rectangular coil exhibited the highest average temperature, exceeding 100°C at 1.5 A; the hexagonal coil reached around 90°C; the circular coil maintained the lowest temperature, around 80°C. While the trends in the experimental and simulation data were consistent, slight discrepancies were observed. These differences are likely due to the IR camera measuring surface temperatures indirectly, which may result in slightly lower recorded values compared to actual coil surface temperatures.

The findings highlight the significant influence of coil geometry on thermal performance. The circular coil exhibited superior thermal behavior, with lower temperatures. In most practical applications, AC signals are the primary choice, and the heat generation is significantly reduced, expanding the safe operational range of these coils.

4.1.4.7 *Magnetic Field Response to Current and Frequency*

The magnetic field, as the primary factor interacting with tissues, directly determines the device's effectiveness. To evaluate magnetic field strength, the coils were tested using the TMR sensor mentioned before under various frequencies and amplitudes of sinusoidal input signals. Measurements were taken on a plane 4 mm above the coil surface, approximating typical skin thickness.

Figure 34. C illustrate the COMSOL simulation results for magnetic field distribution 4 mm above the coil surface with a DC input of 100 mA. Each coil shape exhibited distinct magnetic field characteristics: the circular coil produced a relatively uniform field distribution

with a larger coverage area but the weakest central field strength (150–160 μT); the hexagonal coil showed slightly higher field concentration and moderately stronger central field strength (160–170 μT); the rectangular coil demonstrated the highest field convergence, generating the strongest central magnetic field (180–200 μT).

Figure 34. D gives the cross section of human skin tissue when placing the planar coils on the top of it. As shown in the figure, the vertical field of the circular coil is the most able to penetrate the tissue. Although the square coil has the strongest field strength in the center, its field is not penetrating enough in the vertical direction and decays quickly. While the performance of the hexagonal coil is better, the circular coil may be still the most suitable option for human applications.

Figure 34. E presents 3D bar charts of experimentally measured magnetic field strength for the three coil shapes, illustrating the relationships among current, frequency, and field strength. Across all coil types, magnetic field strength increased with higher input currents and lower frequencies. The field strength increased almost linearly with current, while frequency had a nonlinear influence. Magnetic field strength declined negligibly between 10 Hz and 10 kHz but dropped significantly from 10 kHz to 100 kHz.

At low frequencies (100 Hz), the rectangular coil outperformed the others, producing a magnetic field approximately 20% stronger. However, its magnetic field decreased more rapidly with increasing frequency. In contrast, the circular coil exhibited better performance at higher frequencies, with a slower decline in field strength. The hexagonal coil showed the greatest stability, maintaining minimal decline across the frequency range. Between 10 Hz and 10 kHz, the magnetic field strength decreased by approximately: 40% for the rectangular coil, 25% for the circular coil, and 10% for the hexagonal coil. The discrepancies from the simulation results may stem from the directional limitations of the TMR sensor, which can only focus on the main component of the magnetic field.

4.1.4.8 Magnetic Nanoparticles Actuation

The most important test is whether this coil can interact with MNPs. The driving capability of circular micro-coils on MNPs was evaluated. These MNP coated with poly (maleic anhydride-alt-1-octadecene) (PMAO) of 110 nm in diameter (Figure 35. a and b) exhibit vortex magnetization in their ground state which aligns in plane with the direction of the magnetic field when applied, allowing for generating torques on a pN scales. In the experiment, a circular coil was placed beneath a glass slide with a water-based droplet

containing a relatively high concentration of MNPs (1 mg/mL). A maximum current of 1A was applied using an EL302RD current source. By manually switching the current, the magnetic field from the coil was alternately applied and removed to observe mechanical response of the nanoparticles to these field changes.

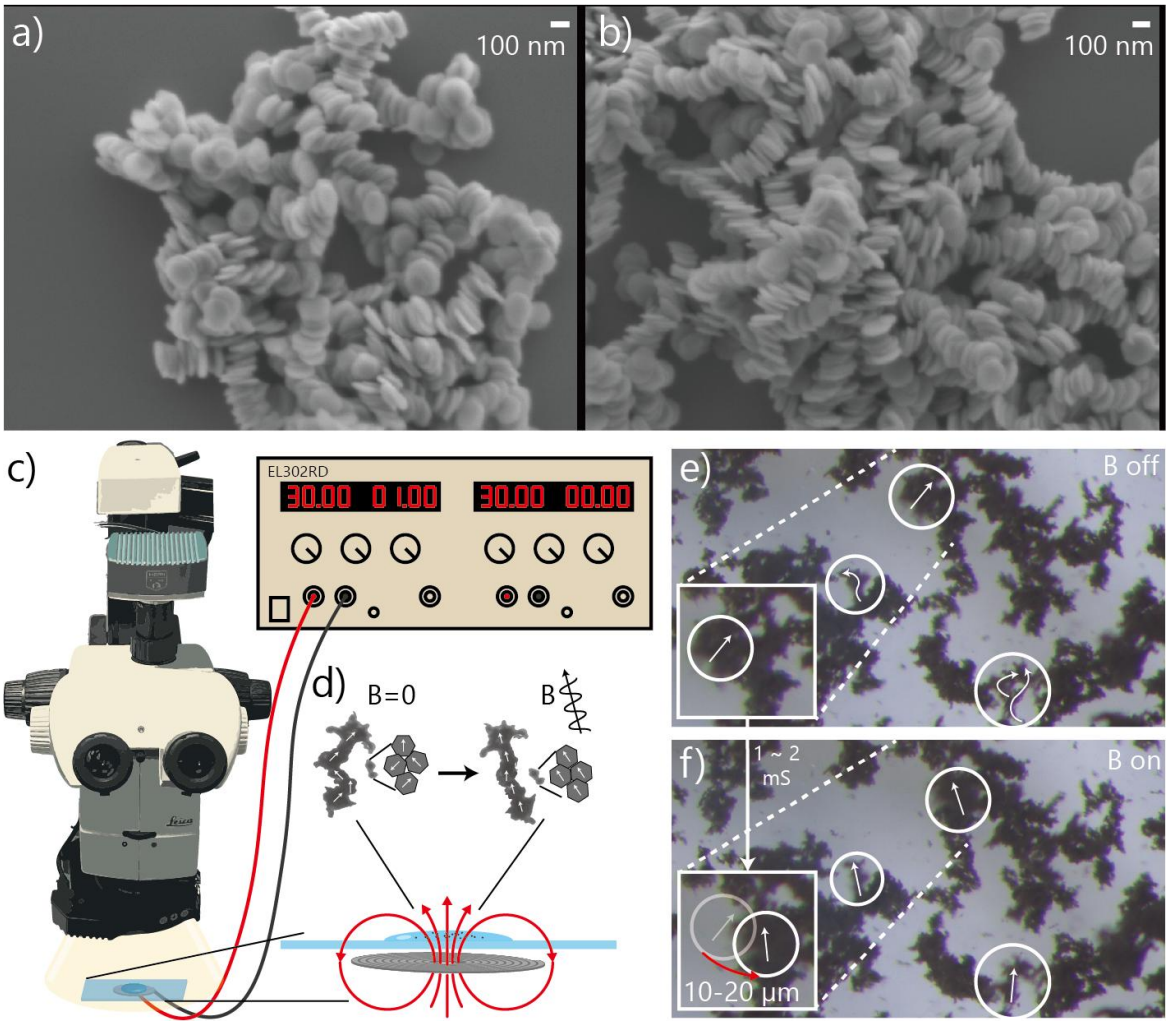

Figure 35. **a**) and **b**) Nanoparticles under scanning electron microscope **c**) The set up of tuning experiment. **d**) The mechanism of MNPs tuning. **e**) and **f**) are optical microscope pictures of MNPs before and after magnetic field applied through mini-coil with response time and displacement distance marked.

The experimental setup, as shown in Figure 35. c. Place the coil beneath a glass slide and connecting it to a 1A current source. A water-based droplet containing MNPs is dipped near the center of the coil and left undisturbed for a period to allow the MNPs to stabilize at the glass surface. The power source is then toggled on and off, and the MNPs' responses at the moments of switching are observed under a microscope. The MNP motion is depicted in Figure 35. d. Initially, MNPs are randomly aggregated and oriented due to their magnetic properties in concentrated solutions. However, when an external magnetic field is applied, the MNPs generate an alignment to maintain consistency with the direction of the external field, hence driving the movement of the MNPs, causing a spatial shift.

Figure 35. e, f demonstrates that MNPs exhibit clear and significant responses to the current source on or off. This confirms that coils fabricated using this method can effectively drive nanoparticles. However, from Figure 35. e and f, it can be observed that the most obvious movement occurs in the smaller branches of the MNP clusters. This is because the larger aggregated clusters (like Figure 35. b), though also move, have higher mass, and more complex interactions between particles, which limits their motion. Additionally, the movement amplitude gradually diminishes over time, because of the unidirectional current input which generates a magnetic field in only one direction. When the current is applied, particles align with the external magnetic field from their initial random orientations. When the current is turned off, the magnetic field is removed, eliminating the aligning torque. Consequently, the particles tend to remain stationary rather than returning to their original positions. As a result, with repeated application and removal of the magnetic field, more particles stay aligned, leading to a reduction in the overall movement amplitude. This experiment proved the basic potential of this coil on MNPs control.

4.2 Experiments with Biointerface Lab, University of Erlangen–Nuremberg (FAU), Germany

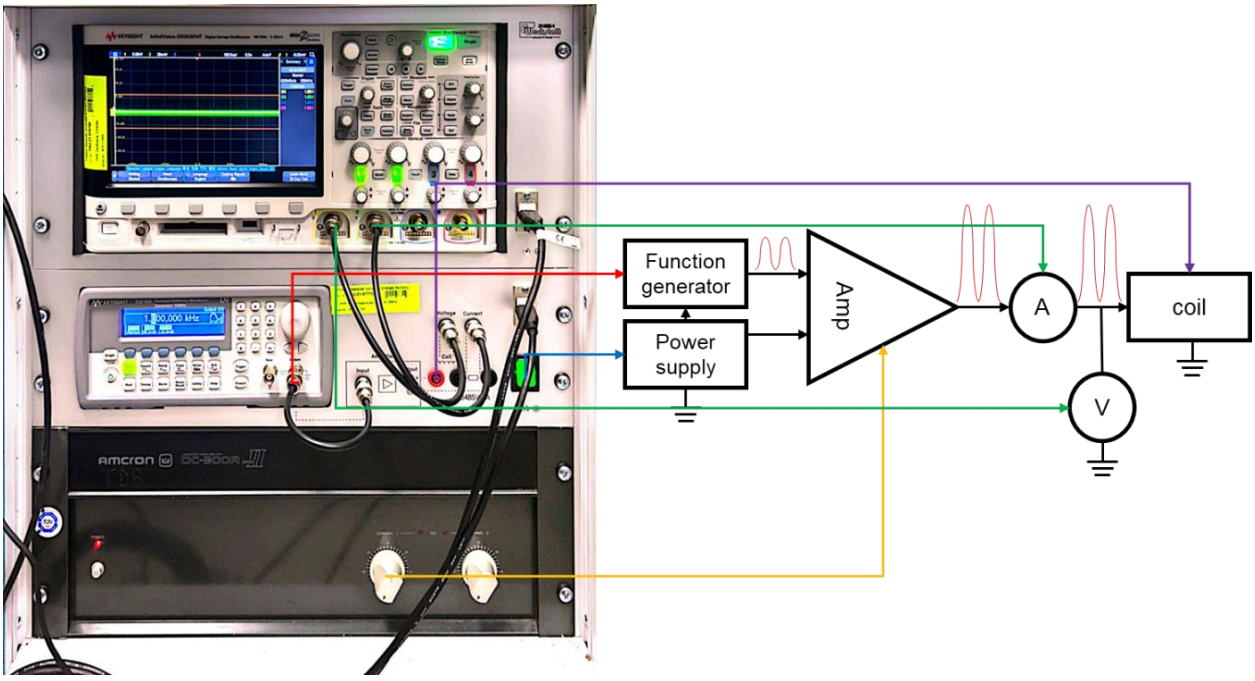

Figure 36. The power system structure.

Have this coil fabricated and successfully interacted with MNPs. The coil was carried to Germany partner's lab for experiment on cell stimulation, observing by calcium imaging. The coil will be powered by the system shown in Figure 36: Oscillator: Keysight InfiniiVision

DSOX3014T, Function generator: Keysight 33210A, and Amplifier: AMCEON DC-300A. Coil is connected to amplifier which enlarge the signal from function generator, and oscillator will monitor the current flows in the coil.

Figure 37. The magnetic nanoparticles under micro-scope and the rotation under 1Hz field from coil in one period.

The same MNPs were used to conduct the previous experiment to verify whether this current source could also achieve MNP control. Since the MNPs used in the experiment were newly fabricated and underwent 5 minutes of ultrasonic dispersion, they were primarily distributed in small clusters. The oscillation of MNPs in response to the signal could be observed under an optical microscope. (Figure 37)

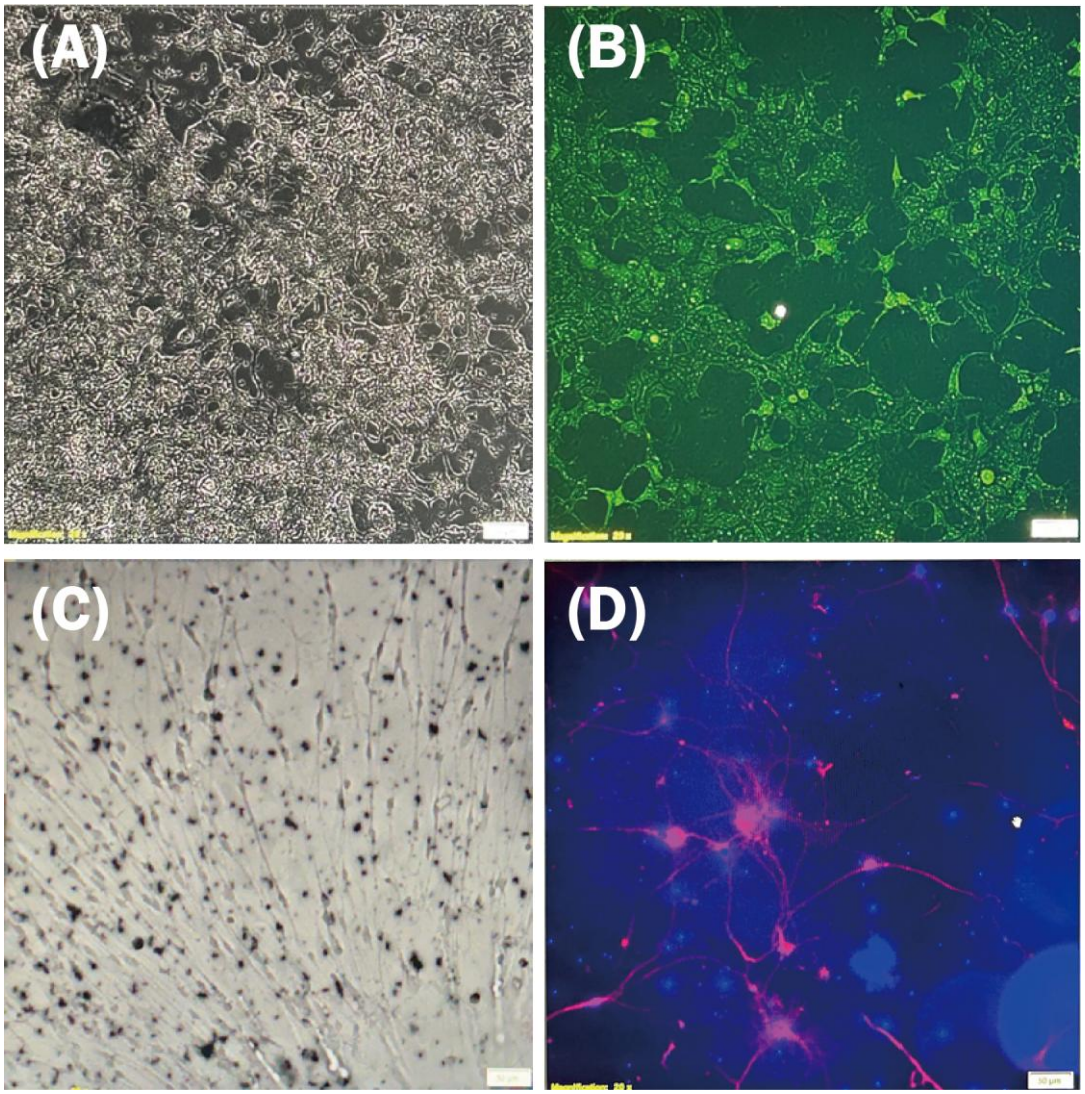

Figure 38. The kidney cell under microscope (**A**) without and (**B**) with fluorescence. The neurons under microscope (**C**) without and (**D**) with fluorescence.

Once confirmed the coil performance, the cells are prepared for *in-vitro* experiment as follow. The kidney cell preparation begins with detachment of the parental cell generation from the culture vessel. Following isolation, the cells are immersed in nutrient medium before being transferred to a fresh culture container. The prepared cells are then maintained at a constant temperature for subsequent experimental applications. (Figure 38. A, B) Neuronal cells are obtained from neonatal rats immediately following birth. The dissection process involves extraction of both brain and spinal cord tissues. The spinal cord tissue is mechanically separated into cellular aggregates, while the hippocampal region undergoes enzymatic digestion to achieve single-cell suspension. These neuronal preparations are cultured under controlled temperature conditions. During the culture period, spinal neurons exhibit process extension from the cellular aggregates, while hippocampal neurons require over one week of cultivation to reestablish synaptic connections and functional networks. (Figure 38. C, D)

The configuration of the fluorescence imaging system is illustrated in the Figure 39. The laser beam emitted from the source follows the green optical path in A, propagating vertically downward to illuminate the cells positioned on the holder shown in B. After passing through the transparent holder, the laser enters the objective lens and is subsequently captured as digital images by the computer.

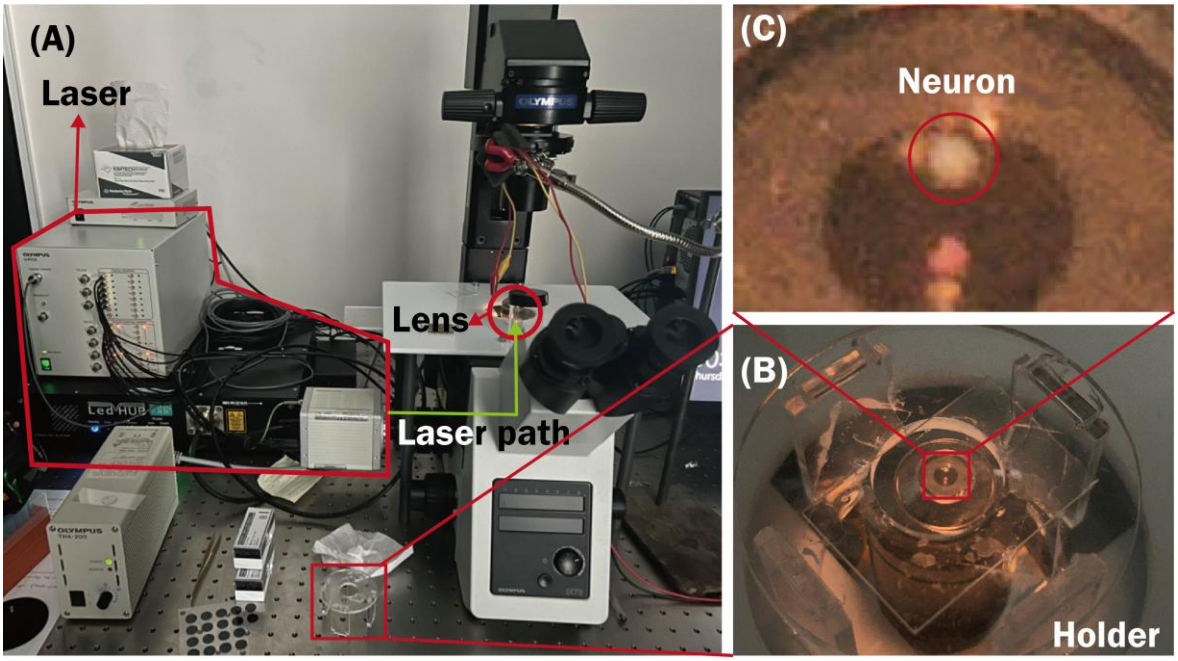

Figure 39. (**A**) Calcium imaging system setup. (**B**) Transparent holder placed upon the lens (**C**) Neuron tissue in the holder.

Based on this experimental setup, tests were conducted on the coil, but the expected phenomena were not observed. The experimental failure may be attributed to two primary factors:

1) There is an incompatibility between the coil and the calcium imaging system. As illustrated in Figure 39, the system relies on the specific optical properties of calcium

ions for cellular imaging. When the coil is positioned above the holder, it reflects or scatters the laser beams that should normally transmit through and exit the system, significantly degrading the final imaging quality (Figure 40).

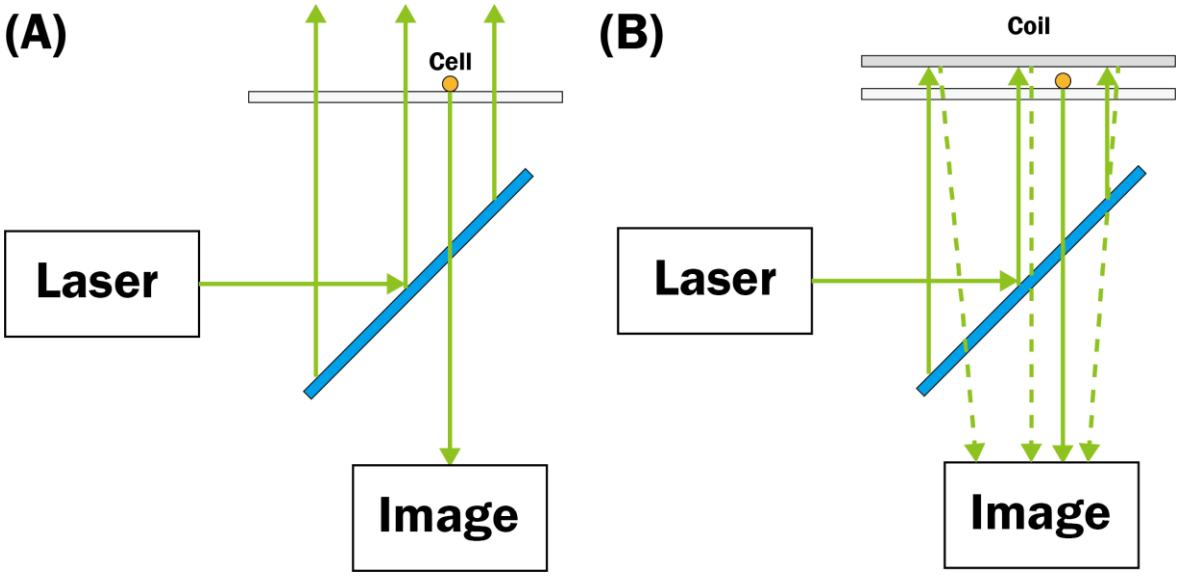

Figure 40. The laser performance (**A**) before and (**B**) after placing a coil.

2) The magnetic field strength generated by the coil may still be insufficient to effectively activate the target cells because the current source cannot generate too large current (e.g. 10A).
3) Although the movement of nanoparticles was observed, when applied to cells, the movement resistance will increase significantly because of the exist of cells. Therefore, the magnetic field strength might be not enough without larger current.

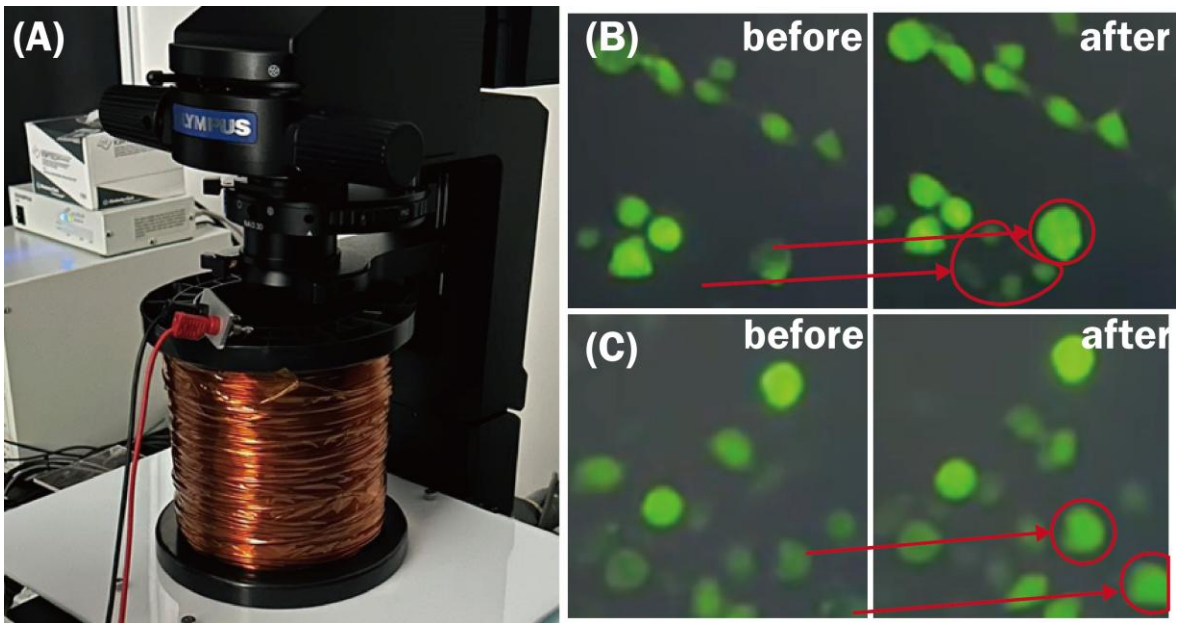

Figure 41. (**A**) Setup of large solenoid coil. (**B**)-(**C**) Two observed examples of activation of cells by calcium imaging.

This inadequate field intensity could explain the lack of observed cellular response despite proper experimental conditions and hence the traditional bulky solenoid (Figure 41. A) was used instead. The cells are successfully activated by MNPs under large coil's magnetic field. This exchange experience directs three crucial factors needs to be considered:

1) The coil design should not only consider *in vivo* but also *in vitro* equipment.
2) Current limits should be a more primary consideration.
3) One possible barrier is heat management under tens of Ampere current even high current source available.
4) The design might need more turns for larger magnetic field and less current.

4.3 SLINKY COIL

Based on the improvement direction obtained above, the design should be compatible with *in vivo* and *in vitro* experiments and does not require too much current. By referencing the relatively coil designs used in TMS technology and incorporating the unique characteristics of magnetic nanoparticle neural stimulation, the slinky coil was identified as a suitable coil configuration (Figure 42. a and c). This design can solve the problems met in previous experiment chapter. The coil's shape makes it be able to be placed beside instead of top of the scope, so it will not block the light route. The coil reduced the current requirement from tens of Ampere to several Ampere by increasing the number of turns.

4.3.1 Wearable coil configuration and design considerations

Introduced in Section 2.2.1.3.3, this design concentrates the magnetic field at a focal area, thereby enhancing stimulation in the target region while minimizing field effects in surrounding areas. Additionally, the slinky coil can be paired with a magnetic core to further concentrate the magnetic field. Due to its enhanced focal precision and stimulation intensity, the slinky coil has been utilized in TMS for DBS applications. However, for MNP stimulation, modifications to the slinky coil design are necessary. Specifically, the slinky coil, originally designed for human head-sized applications, should be scaled down to the cm level to meet the precision requirements of MNP stimulation. Additionally, the possible integration of multiple coils into an array capable of covering the entire brain is being explored to enable programmable selection of stimulation regions, thereby enhancing the flexibility and specificity of the stimulation process.

This initiative represents the first effort to miniaturize the slinky coil while maintaining its ability to produce a strong magnetic field across multiple operating frequencies. Key considerations include determining the optimal size for miniaturization, ensuring the scaled-

down coil can generate a sufficiently powerful magnetic field, managing heat dissipation, and achieving compatibility with both *in vitro* and *in vivo* experimental systems. These issues are interconnected, forming a complex optimization problem that requires multi-dimensional balancing and validation through experiments conducted from various perspectives. Addressing these factors is critical to the successful development and application of the device.

4.3.2 Coil Fabrication and Feasibility Proof

The fabrication process is much simpler than the other coils mentioned above. Start with designing a holder for wire to wind through Fusion 360. Then, use 3D printer to print the holder and manually wind the wire on it. A prototype coil with 250 turn 0.22 mm copper wire wound on PLA holder is shown in Figure 42. c.

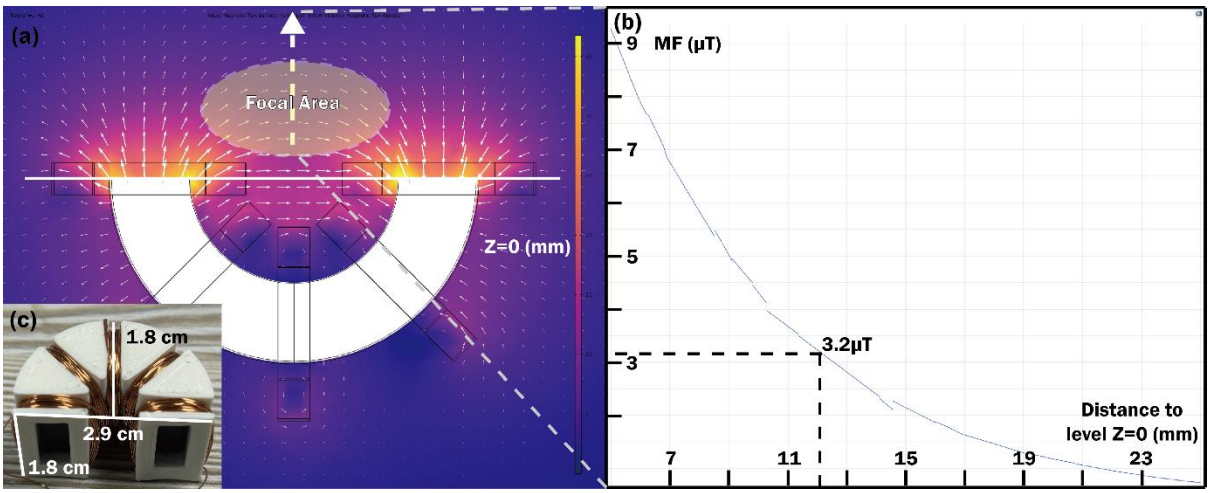

Figure 42. (**a**) Simulation result of magnetic field distribution map. (**b**) Magnetic field drop along the red line in (a). (**c**) Prototype sample of slinky coil with 250 turns.

The feasibility of the slinky coil was evaluated through a combination of COMSOL simulations and prototype fabrication. Considering the size and weight suitable for a mouse wearable application. A coil holder measuring 2.9 × 1.8 × 1.8 cm (Figure 42. c) was developed, based on the dimensions of the magnetic core (μ_r is 500). Because the magnetic field will attenuate along distance, the magnetic core will gather the field and strengthen the magnetic density which will decrease the attenuation. 250 turns of enamel-coated 0.11 mm radius Cu wire are selected as 50 turns in each batch will roughly fill the space of the holder, which also simplifies the calculation. In the COMSOL simulations, the Magnetic and Electric Fields (MEF) physics module was used to model the magnetic field strength generated by a 5 by 50-turn slinky coil when supplied with a 5 Hz, 1 mA current. The simulation results, along with images of the coil, are presented in Figure 42. To validate the simulations, experimental measurements of the magnetic field were conducted under the same input conditions, reading

the magnetic field 12 mm away from coil is 2.85 μT, while the field strength the same position from simulation result is 3.2 μT. Although the experimentally measured magnetic field strength was 10% lower than the values obtained from simulations, the results were generally comparable. The difference might come from the sensor which can only measure magnetic field in one direction. Based on these observations, it is estimated that a magnetic field on the mT scale can be achieved with an input current on the order of amperes.

4.3.3 Parameter optimization for low-frequency application

While there is no fixed formula to describe the spatial distribution of the magnetic field generated by this coil configuration, general principles of coil-generated magnetic fields can be applied for estimation. Two primary factors directly related to the current must be considered: the magnetic field strength and Joule heating. For a coil of fixed size and shape, the magnetic field strength is proportional to the product of the current and the number of turns (Eq. 4.3). Meanwhile, the power dissipated as Joule heat is proportional to the product of the current squared and the resistance. Since the resistance is proportional to the number of turns (assuming each turn requires an equal length of wire), Joule heating is also proportional to the product of the current squared and the number of turns (Eq. 4.4). It follows that, under the condition of maintaining a constant magnetic field strength (i.e., keeping the product of current and turns, NI, constant), increasing the current I rather than the number of turns N would result in significantly higher Joule heating. Therefore, the primary modification to the coil design should focus on maximizing the number of turns to minimize power dissipation while achieving the desired field strength.

$$B \sim NI \tag{4.3}$$

$$P_{heat1} = I^2R \sim I^2N \tag{4.4}$$

However, the N value cannot be increased indefinitely, as it is ultimately constrained by the coil's physical dimensions and consequent parasitic capacitance. When available space is fixed, there will be a trade-off between wire thickness and number of turns. Specifically, the available winding cross-sectional area S is equal to the product of the wire's cross-sectional area S_0 and the number of turns N (Eq. 4.5). When using wire of the same material, the total resistance of the coil is proportional to the product of N and $\frac{1}{S_0}$. Since N is inversely proportional to S_0 the total resistance is proportional to the $\frac{1}{S_0{}^2}$ or N^2(Eq. 4.6). For instance, halving the wire's cross-sectional area allows the number of turns to double, but the resistance increases by a factor of four. Therefore, the optimal design should aim to minimize N while using the thickest possible wire to balance these trade-offs. According to Eq. 4.3, the power of Joule heat will not change when generating same magnetic field (Eq. 4.7).

$$S = NS_0 \tag{4.5}$$

$$R \sim \frac{1}{{S_0}^2} \sim N^2 \tag{4.6}$$

$$P_{heat2} = I^2R \sim I^2N^2 \sim B^2 \tag{4.7}$$

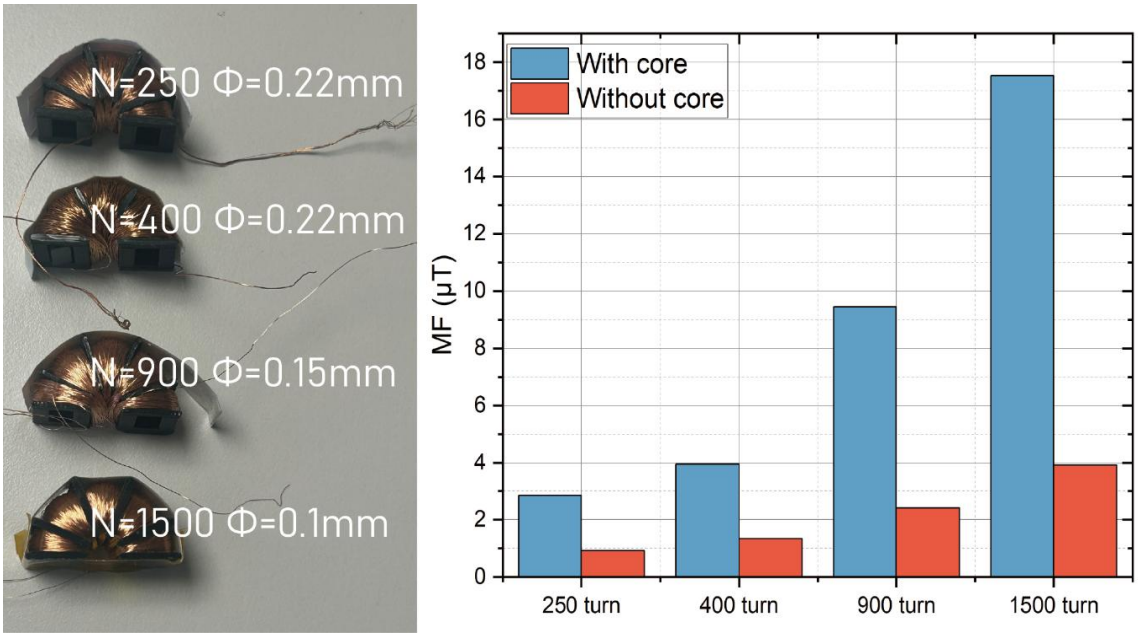

Figure 43. Four prototypes made by different kind of wires with different number of turns and the measurement results of magnetic field generated by them with/without a core under 1mA input.

Based on the principles outlined above, four coil samples (Figure 43 left) were fabricated with the following parameters: 250-turn (0.22 mm wire), 400-turn (0.22 mm wire), 900-turn (0.15 mm wire), and 1500-turn (0.1 mm wire). The magnetic field strength generated by these coils was measured at 1.2 cm under a 1 mA, 5 Hz current input, both with and without a magnetic core. The results, presented in Figure 43, reveal an approximately linear relationship between the magnetic field strength and the number of turns. With a magnetic core, each 100 turns produced a magnetic field of approximately 1 μT, while without a core, the field strength was reduced to 0.25 μT. This confirms the necessity of a magnetic core for low-frequency operation.

Using the principle that the magnetic field scales linearly with current, the required current to achieve the target field strength of 25 mT (with core) was estimated, as shown in Figure 44. The low-frequency resistance of the coils was measured to be 5.4 Ω, 8.9 Ω, 46 Ω, and 161 Ω, respectively, allowing for the calculation of the required power supply voltage and corresponding maximum Joule heating power, as illustrated in Figure 44. These results align closely with the theoretical predictions, by comparing N=250 turns and N=400 turns, before

using up more space, it is important to increase N as much as possible (Eq. 4.4). As for the 400, 900, and 1500 number of turns, it has been demonstrated that when the available cross-sectional area is fully utilized, the thermal power does not increase with N (Eq. 4.7). However, a higher N requires higher driving voltages, placing greater demands on the source and introduce significant inductive reactance at high frequencies, which could degrade performance. Therefore, a 400-turn configuration is likely the optimal solution, effectively balancing these trade-offs.

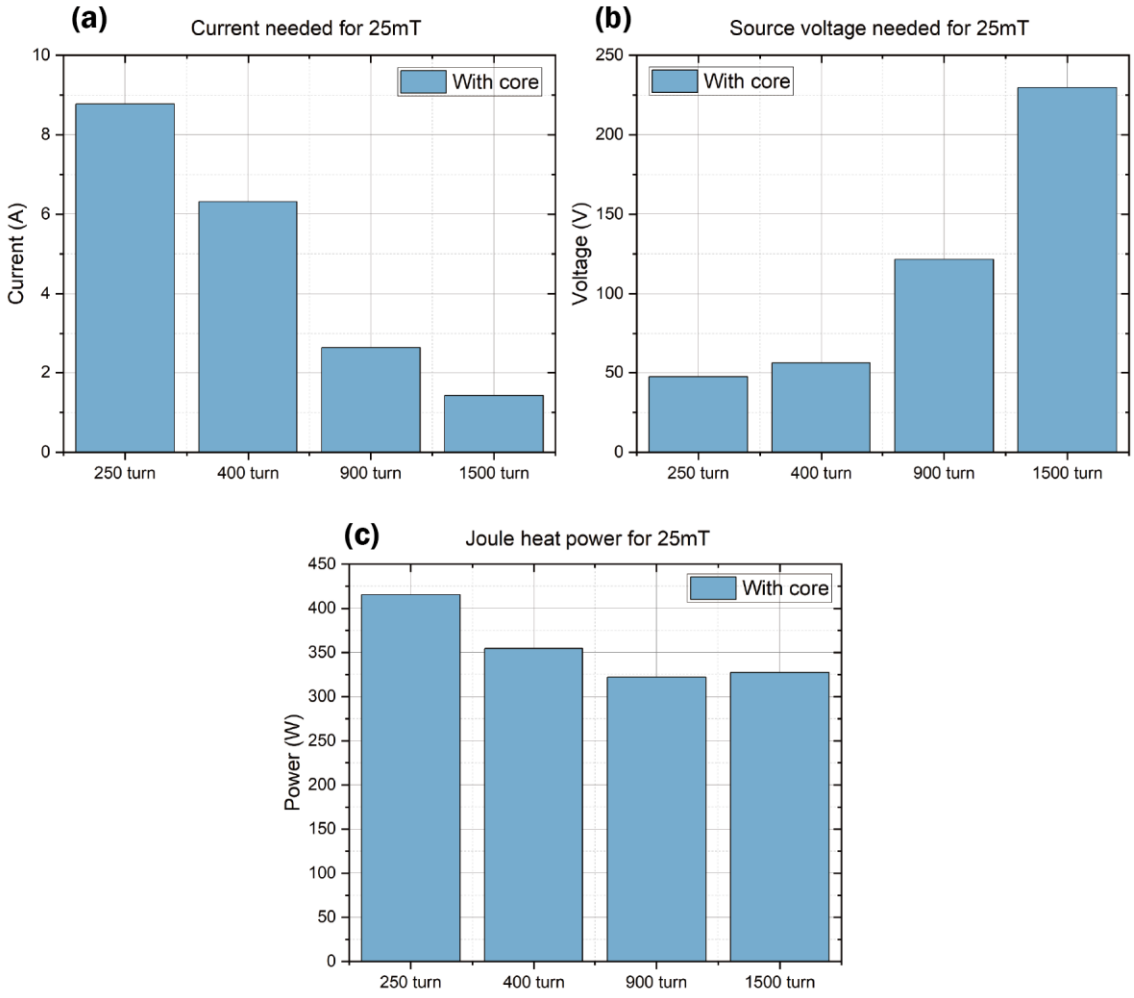

Figure 44. The estimated (**a**) current, (**b**) voltage, and (**c**) Joule heat power needed to generate 25mT magnetic field at 12mm distance for coil samples in Figure 43.

4.3.4 Parameter optimization for high-frequency application

The primary challenge in high-frequency applications arises from the high impedance response of the coil's inductance at elevated frequencies. Using LCR measurements, the inductance and equivalent resistance of the four coil configurations were determined at 20 Hz and 100 kHz. The results indicate that the presence of a magnetic core significantly increases the inductance, while the frequency (20 and 100k Hz) has minimal impact on the inductance value. In contrast, the equivalent resistance increases at higher frequencies, regardless of

whether a magnetic core is present. This rise in resistance can be attributed to the skin effect (under high frequency, the current tends to flow along the skin of wire, which will decrease equivalent cross section and increase the equivalent resistance), which becomes more pronounced as operating frequency increases. Additionally, the magnetic core further amplifies the equivalent resistance due to phenomena such as magnetic hysteresis, which are inherent to high-frequency magnetic fields. Furthermore, the large inductive reactance generated by the inductance at high frequencies contribute to a total impedance of at least 10 kΩ in magnitude.

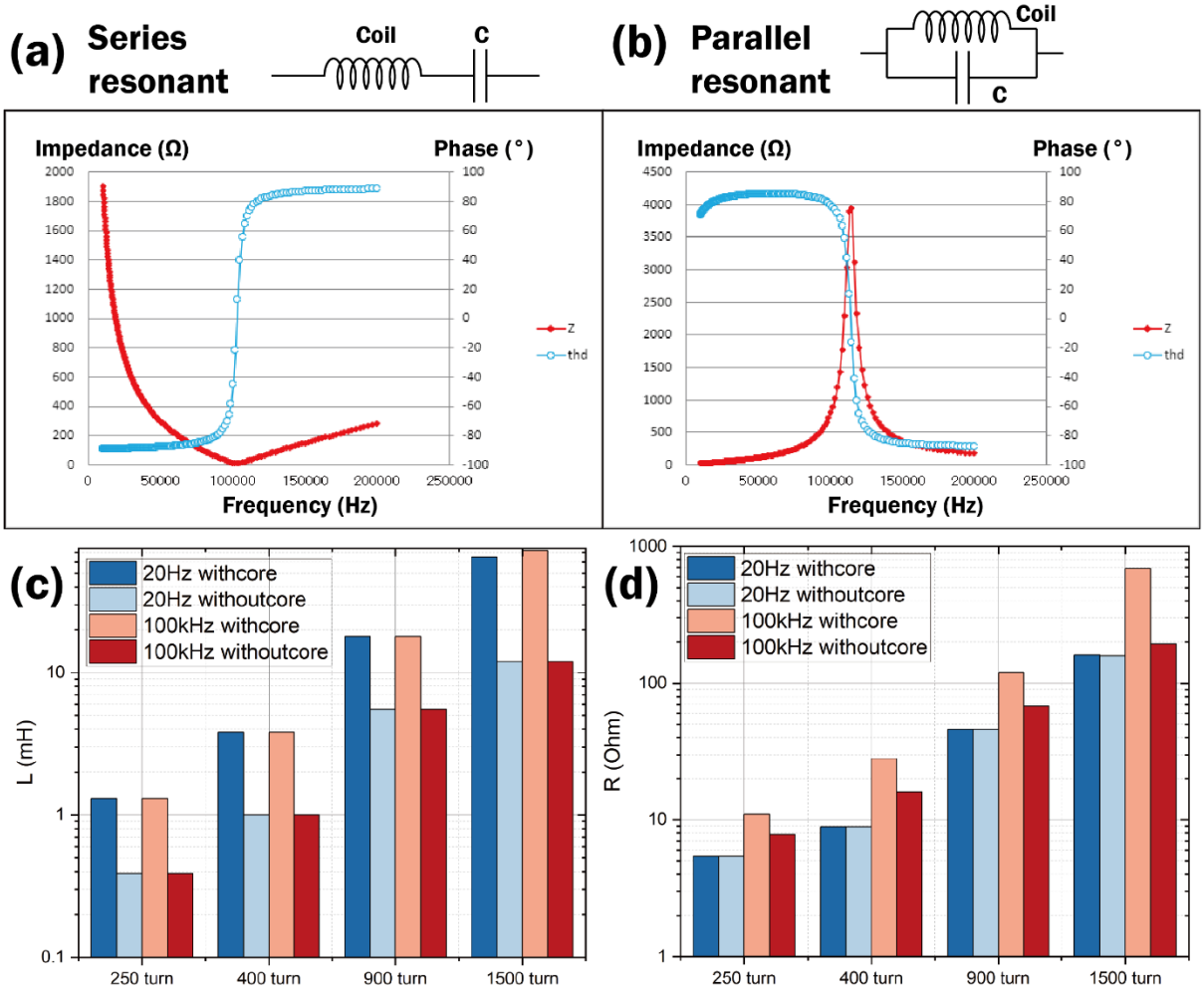

Figure 45. The structural and impedance characteristics of (**a**) series resonant circuits and (**b**) parallel resonant circuits. The (**c**) inductance and (**d**) equivalent resistance of coil samples in Figure 43.

To maximize the current flow in the inductance at high frequency, resonant circuits are commonly employed. These circuits can be configured in two structures: series resonant circuits and parallel resonant circuits. In a series resonant circuit, the coil is connected a capacitance serially, when the inductive reactance and capacitive reactance cancel each other, resulting in a resistive circuit and minimizing the impedance (shown in Figure 45. a). On the other hand, a parallel resonant circuit forms a resonant cavity by parallelly connect the coil

and capacitance (Figure 45. b), where the equivalent impedance may reach to a level of 104 to 105 Ω. This configuration allows for a small gross current while enabling large currents to flow through the capacitor and inductor but needs a very large voltage at the same time. Simulation and experiments are needed to decide to select which configuration.

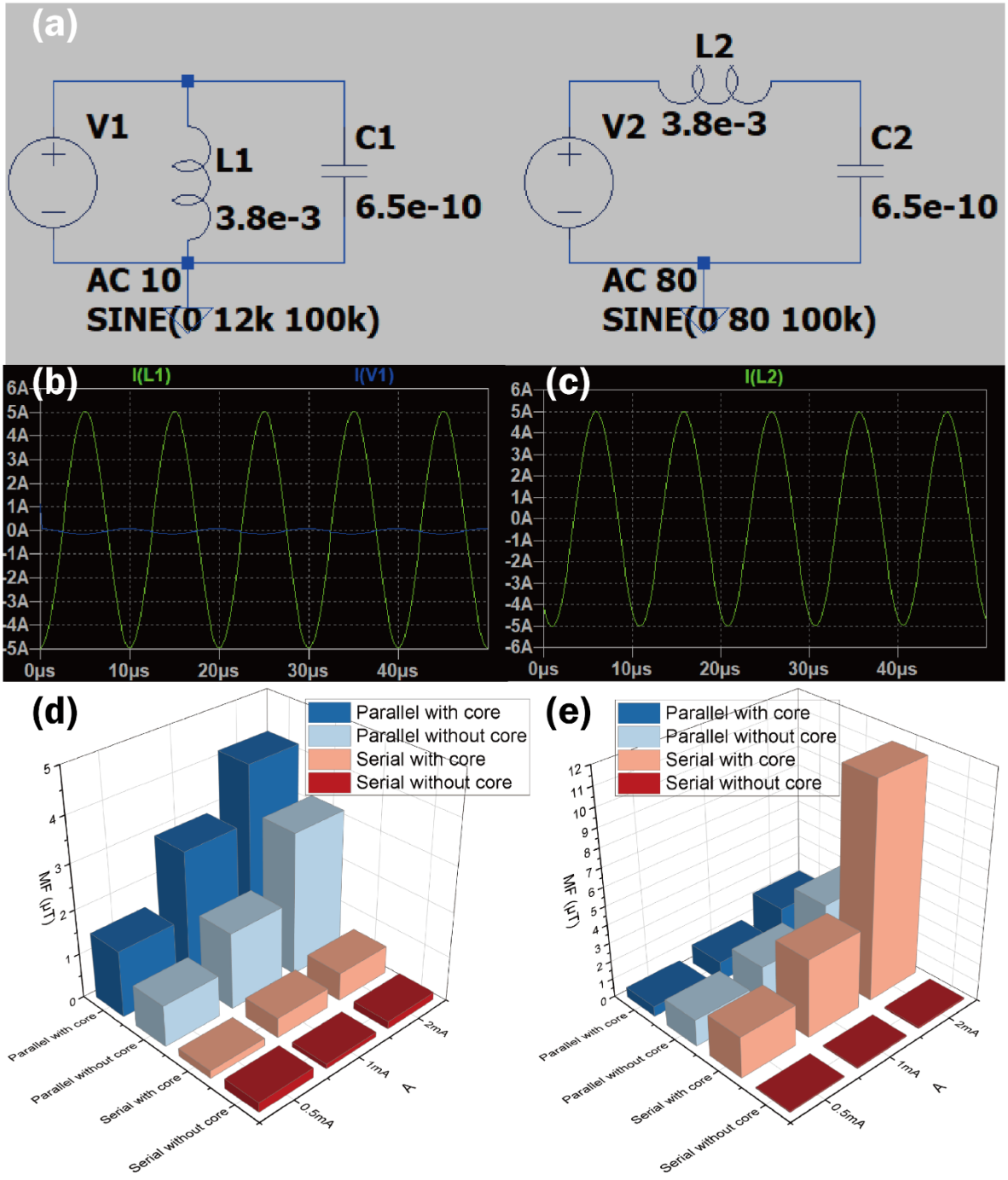

Figure 46. (**a**) LTspice simulation setup. Simulation results of (**b**) parallel resonant circuits and (**c**) series resonant circuits. Magnetic field measurement under both resonant circuit and different current input of (**d**) 400-turn sample and (**e**) 250-turn sample.

To decide which resonant circuits performs better, simulations were conducted using LTspice with set up as shown in Figure 46. a. The simulations utilized the previously chosen 400-turn

coil, incorporating its measured inductance and series resistance. The objective was to determine the source conditions required to achieve a 5 A current through the coil. The simulation results, presented in Figure 46. b and c, show that the parallel resonant circuit requires a 12 kV voltage source, with a total current of 80 mA. In contrast, the series resonant circuit requires only an 80 V voltage source, with the current through the voltage source matching the 5 A current in the inductor. As a result, the maximum power consumption of the parallel circuit is 960 W, while that of the series circuit is approximately 400 W. Therefore, the series circuit may have better performance, but needs further experiments to prove.

Magnetic field at 100kHz measurements were subsequently conducted for both resonant circuit configurations using the 400-turn coil, with the results shown in Figure 46. d. Although the parallel configuration appeared to perform better, this was primarily due to its inherent advantage to use a smaller current to generate a larger magnetic field. To facilitate a fair comparison, according to the simulation results where the ratio of current flow in power source is 80:5000, the parallel circuit's output under 1mA was scaled by a factor of 80, and similarly the series circuit's output under 1mA was scaled by a factor of 5000, aligning them with the simulated currents, to estimate the situation when they have the same expected current in the coil wire. After scaling, the parallel configuration produced a magnetic field of 214 μT, while the series configuration produced a field of 1.83 mT, which are significantly lower than the predicted values. Additionally, the linear relationship between magnetic field strength and current was found to be inconsistent.

To further investigate these discrepancies, a second set of tests was performed using a 250-turn coil under the same conditions. The results, shown in Figure 46. e, are compared to the previous experiment: the series configuration demonstrated superior results. Notably, the series configuration exhibited an unexpected peak value at 2 mA, far exceeding the predicted outcome (confirmed not to be a measurement error). Furthermore, the influence of the magnetic core in this experiment contradicted the findings from the first set of tests.

Currently, although no definitive explanation for these observations, our explanation is that the capacitor may not be precisely tuned to resonate with the coil at the intended frequency. A deviation between the actual resonant frequency and the target frequency of 100 kHz could result in suboptimal performance. To address this issue, a potential improvement could involve the design of a variable capacitor system, enabling adjustment of the capacitance to identify the optimal configuration for maximizing coil performance.

4.3.5 Optimization in weight

Given that the coil is intended for use in animal experiments, the weight-bearing capacity of the experimental subjects must be carefully considered. The 400-turn coil with dimensions of 2.9 × 1.8 × 1.8 cm, including the magnetic core, weighs 16.32 g, which may impose a significant burden on laboratory mice. To address this issue, a weight reduction strategy was implemented. By reducing the coil's thickness, using a smaller magnetic core, and employing more compact winding, a 400-turn coil with dimensions of 2.9 × 1.7 × 1.4 cm was developed. Measurements indicate that the new coil, including the magnetic core, weighs 10.21 g, representing a 38% reduction in weight. Additionally, due to the shorter total wire length resulting from the reduced size, the coil's resistance decreased by approximately 15% to 7.5 Ω. Although the new coil generates a weaker magnetic field than the original coil in the absence of a magnetic core, measurements show that the magnetic field strength is almost same to that of the original coil when a magnetic core is used. Therefore, this design achieves a significant reduction in weight and heat generation while maintaining the desired magnetic field strength. Further improvements will be pursued by utilizing magnetic cores with higher permeability and reducing their size. This approach aims to further decrease the weight and resistance of the coil while maintaining or enhancing its performance.

4.3.6 Thermal Management

Development of optimized thermal insulation and heat-resistant materials to ensure stable coil operation at potentially high current loads while minimizing thermal impact on biological specimens. Preliminary evaluation of novel 3D-printing PET-CF material has been used, demonstrating exceptional thermal stability (over 200°C) while maintaining structural integrity under significant thermal loads.

4.3.7 Summary

During the exploration of the slinky coil, first successfully achieved the generation of magnetic fields of tens of mT under low-frequency input conditions and observed the movement of nanoparticles in the magnetic field. At the same time, verified the linear relationship between the magnetic field and the current input, which could provide prediction of different current input. Furthermore, achieved some success in optimizing the magnetic field under high-frequency signal input. The addition of a resonant circuit proved that the magnetic field did increase compared to the case without the circuit, but it did not reach a stable state and could not be predicted based on a linear relationship. This may be due to the resonant circuit's extreme sensitivity to the resonant frequency, and inaccurate measurements of the coils and inductances that make up the circuit. This can lead to a small, non-negligible

gap between the input frequency and the resonant frequency, preventing the resonant circuit from fully functioning. This may be a key area for future research.

5 CONCLUSION AND OUTLOOK

This project proposed new techniques for magnetic stimulation technologies, including non-invasive, invasive, and nano-invasive magnetic stimulation, and explores microfabrication methods potentially applicable for the next-generation magnetic stimulation. Based on the review of current technological advancements, potential developmental direction for each technique is discussed, while recognizing how the coil development affects the technology. Building upon these assessments, investigation on coil optimization and fabrication of both invasive and nano-invasive magnetic stimulation technologies is performed.

5.1 INVASIVE MAGNETIC STIMULATION

For invasive magnetic stimulation, a novel coil type, probe micro-coil, is selected as the research object, and the working principle of its selective stimulation is fully reviewed, analyzed, and discussed. A hypothesis is brought up to solve existing questioning towards mechanism of selective invasive magnetic stimulation. Then three possible optimization routes of probe micro-coil are proposed, following large-scale fabrication of these designs. During the fabrication, a laser-assisted cleanroom fabrication process, along with a combination methodology between two system is innovated, hence significantly increasing the efficiency of the fabrication process. Last, biological compatibility testing confirmed that coils produced via this fabrication process exhibit excellent biocompatibility while enabling the incorporation of traditionally non-biocompatible metals (e.g., Al) into the design. This technological advancement significantly expands the range of applicable materials and potentially enables low-cost fabrication solutions, which will help cross the barrier to wide-spread applications of this technology.

The limitation of the research in this area is lack of *in vivo*/ *in vitro* experiments. This work has demonstrated certain limitations in mainstream theoretical explanations and proposed an alternative hypothesis based on existing experimental results. Although this hypothesis can well explain the current experimental phenomenon, direct evidence is essential to finally prove this hypothesis, which needs experiments. The coil design improvements performance is estimated through simulation and the biocompatibility of the fabrication technique has been demonstrated, which also needs experiments in real neurons to exam if it can really evoke neurons in an expected way. Besides, a circuit design might also be needed to perform mobile and precise control of stimulation.

5.2 Nano-invasive Magnetic Stimulation

In nano-invasive magnetic stimulation area, two mini-coil designs, planar and slinky coils, are proposed. As this field remains in its early stages with limited prior research, the coil designs explored here possess an experimental character. For planar coils, three fabrication methods are explored: laser processing, ultra-thick photolithography, and physical cutting. Here, several fabrication advancements are achieved: systematic parametric analysis of laser cutting parameters; optimization of development protocols for ultra-thick (over 80μm) photoresist layers; introduction of a novel, cost-effective physical cutting fabrication method, cutting down the overall fabrication expense from millions of pounds to hundreds of pounds. While the resulting planar coils demonstrated capability for nanoparticle control, their implementation was ultimately discontinued due to incompatibility with experimental setup and potentially insufficient magnetic field strength. However, all above fabrication methods accumulated experience for other microelectronics devices, and, additionally, this coil design can also be transformed to other applications like wireless power transfer. For the slinky coil, it is the first time that successfully miniaturize it into cm scale, capable to high-strength (tens of mT) magnetic fields. During its development, the fundamental design principles for the coil were summarized, and innovative approaches are explored, employing resonant circuits, thus enabling high-current operation at high working frequencies. These investigations have yielded promising preliminary results, though additional research is required to fully realize the technology's potential.

Since planar coils proved to be unsuitable for this application, future work may focus on exploring other possible applications such as wireless charging or mini heater. Regarding the slinky coil development, which remains ongoing, several specific future research directions have been identified:

1) **Controllable Variable Capacitor System**: Implementation of a precision-adjustable capacitor array to enable detailed characterization of coil performance under high-frequency conditions. This system will permit real-time tuning and optimization of resonant properties.
2) **Circuit Matching:** For high frequency application, matching problem is important for high frequency application, for example, the capacitor system mentioned above.
3) **Advanced Magnetic Core Materials**: Customized magnetic cores with enhanced permeability (μ_r above 2000) and operational frequency characteristics (up to 100MHz) are being procured to replace existing components. These cores will

undergo precision machining to reduce its size, thereby simultaneously improving thermal management and weight reduction.

After this, a more general strategies should focus on finishing tuning the resonant circuit under high-frequency mode. Then *in vitro*/ *in vivo* experiments are needed to exam the coil system.

In summary, the work presented in this project has accumulated substantial knowledge for next-generation magnetic stimulation coil design and fabrication. These contributions are expected to help accelerate ongoing research in the field, and firmly believe that completion of the proposed future work will significantly advance this technological domain.

6 REFERENCE

[1] D. Magis and J. Schoenen, "Advances and challenges in neurostimulation for headaches," *The Lancet Neurology,* vol. 11, no. 8, pp. 708-719, 2012, doi: 10.1016/S1474-4422(12)70139-4.

[2] W. Schuepbach *et al.*, "Neurostimulation for Parkinson's disease with early motor complications," *New England Journal of Medicine,* vol. 368, no. 7, pp. 610-622, 2013, doi: 10.1056/NEJMoa1205158.

[3] G. K. Bergey, "Neurostimulation in the treatment of epilepsy," *Experimental neurology,* vol. 244, pp. 87-95, 2013, doi: 10.1016/j.expneurol.2013.04.004.

[4] O. World Health, *Neurological disorders: public health challenges* (no. Book, Whole). Geneva: World Health Organization (in English U6 - ctx_ver=Z39.88-2004&ctx_enc=info%3Aofi%2Fenc%3AUTF-8&rfr_id=info%3Asid%2Fsummon.serialssolutions.com&rft_val_fmt=info%3Aofi%2Ffmt%3Akev%3Amtx%3Abook&rft.genre=book&rft.title=Neurological+disorders&rft.date=2006-01-01&rft.pub=World+Health+Organization&rft.externalDBID=TA1&rft.externalDocID=b34722191&paramdict=en-us U7 - eBook), 2006.

[5] D. Cappon, T. den Boer, C. Jordan, W. Yu, E. Metzger, and A. Pascual-Leone, "Transcranial magnetic stimulation (TMS) for geriatric depression," *Ageing Research Reviews,* vol. 74, p. 101531, 2022, doi: 10.1016/j.arr.2021.101531.

[6] X. Jiang *et al.*, "Effects of repetitive transcranial magnetic stimulation on neuropathic pain: A systematic review and meta-analysis," *Neuroscience & Biobehavioral Reviews,* vol. 132, pp. 130-141, 2022, doi: 10.1016/j.neubiorev.2021.11.037.

[7] H. Tavakoli and A. Heidarpanah, "Literature Review of the Efficacy of Repetitive Transcranial Magnetic Stimulation on Epilepsy," *Iranian Journal of Child Neurology,* vol. 17, no. 1, p. 9, 2023, doi: 10.22037/ijcn.v17i2.38752.

[8] Y. Tufail *et al.*, "Transcranial pulsed ultrasound stimulates intact brain circuits," *Neuron,* vol. 66, no. 5, pp. 681-694, 2010, doi: doi:10.1016/j.neuron.2010.05.008.

[9] G. Darmani *et al.*, "Non-invasive transcranial ultrasound stimulation for neuromodulation," *Clinical Neurophysiology,* vol. 135, pp. 51-73, 2022, doi: 10.1016/j.clinph.2021.12.010.

[10] J. M. Schwalb and C. Hamani, "The history and future of deep brain stimulation," *Neurotherapeutics,* vol. 5, no. 1, pp. 3-13, 2008, doi: 10.1016/j.nurt.2007.11.003.

[11] K. Starnes, K. Miller, L. Wong-Kisiel, and B. N. Lundstrom, "A review of neurostimulation for epilepsy in pediatrics," *Brain sciences,* vol. 9, no. 10, p. 283, 2019, doi: 10.3390/brainsci9100283.

[12] S. L. Tripathi, K. B. Prakash, V. E. Balas, S. K. Mohapatra, and J. Nayak, *Electronic devices, circuits, and systems for biomedical applications: Challenges and intelligent approach*. Academic Press, 2021.

[13] S. F. Cogan, K. A. Ludwig, C. G. Welle, and P. Takmakov, "Tissue damage thresholds during therapeutic electrical stimulation," *Journal of neural engineering,* vol. 13, no. 2, p. 021001, 2016, doi: 10.1088/1741-2560/13/2/021001.

[14] A. Butterwick, A. Vankov, P. Huie, Y. Freyvert, and D. Palanker, "Tissue damage by pulsed electrical stimulation," *IEEE Transactions on Biomedical Engineering,* vol. 54, no. 12, pp. 2261-2267, 2007, doi: 10.1109/TBME.2007.908310.

[15] A. C Thompson, P. R Stoddart, and E. D. Jansen, "Optical stimulation of neurons," *Current Molecular Imaging (Discontinued),* vol. 3, no. 2, pp. 162-177, 2014.

[16] J. A. Cardin *et al.*, "Targeted optogenetic stimulation and recording of neurons in vivo using cell-type-specific expression of Channelrhodopsin-2," *Nature protocols,* vol. 5, no. 2, pp. 247-254, 2010, doi: 10.1038/nprot.2009.228.

[17] F. Gilbert, A. R. Harris, and R. M. Kapsa, "Controlling brain cells with light: ethical considerations for optogenetic clinical trials," *AJOB Neuroscience,* vol. 5, no. 3, pp. 3-11, 2014, doi: 10.1080/21507740.2014.911213.

[18] R. S. Weiss, A. Voss, and W. Hemmert, "Optogenetic stimulation of the cochlea—A review of mechanisms, measurements, and first models," *Network: Computation in Neural Systems,* vol. 27, no. 2-3, pp. 212-236, 2016, doi: 10.1080/0954898X.2016.1224944.

[19] P. M. Rossini *et al.*, "Non-invasive electrical and magnetic stimulation of the brain, spinal cord, roots and peripheral nerves: Basic principles and procedures for routine clinical and research application. An updated report from an IFCN Committee," *Clinical neurophysiology,* vol. 126, no. 6, pp. 1071-1107, 2015, doi: 10.1016/j.clinph.2015.02.001.

[20] P. J. Basser and B. J. Roth, "New currents in electrical stimulation of excitable tissues," *Annual review of biomedical engineering,* vol. 2, no. 1, pp. 377-397, 2000, doi: 10.1146/annurev.bioeng.2.1.377.

[21] A. V. Peterchev *et al.*, "Fundamentals of transcranial electric and magnetic stimulation dose: definition, selection, and reporting practices," *Brain stimulation,* vol. 5, no. 4, pp. 435-453, 2012, doi: 10.1016/j.brs.2011.10.001.

[22] S. W. Lee, K. Thyagarajan, and S. I. Fried, "Micro-Coil Design Influences the Spatial Extent of Responses to Intracortical Magnetic Stimulation," (in English), *IEEE transactions on biomedical engineering,* vol. 66, no. 6, pp. 1680-1694, 2019, doi: 10.1109/TBME.2018.2877713.

[23] R. Chen, G. Romero, M. G. Christiansen, A. Mohr, and P. Anikeeva, "Wireless magnetothermal deep brain stimulation," *Science,* vol. 347, no. 6229, pp. 1477-1480, 2015, doi: 10.1126/science.1261821.

[24] M. d'Arsonval, "Dispositifs pour la mesure des courants alternatifs de toutes fréquences," *Comput. rend. Soc. biol.,* vol. 3, pp. 430-451, 1896.

[25] L. A. Geddes, "The history of magnetophosphenes [Retrospectroscope]," (in English), *IEEE engineering in medicine and biology magazine,* vol. 27, no. 4, pp. 101-102, 2008, doi: 10.1109/MEMB.2008.925871.

[26] M. Polson, "St-imulation of nerve trunks with time-varying mag-netic fields," *Med. Biol. Eng. Comput,* vol. 20, pp. 243-244, 1982, doi: 10.1007/BF02441362.

[27] A. T. Barker, R. Jalinous, and I. L. Freeston, "Non-invasive magnetic stimulation of human motor cortex," *The Lancet,* vol. 325, no. 8437, pp. 1106-1107, 1985, doi: 10.1016/S0140-6736(85)92413-4.

[28] Y. Terao and Y. Ugawa, "Basic mechanisms of TMS," *Journal of clinical neurophysiology,* vol. 19, no. 4, pp. 322-343, 2002, doi: 10.1097/00004691-200208000-00006.

[29] M. Hallett, "Transcranial magnetic stimulation: a primer," *Neuron,* vol. 55, no. 2, pp. 187-199, 2007, doi: 10.1016/j.neuron.2007.06.026.

[30] X. Yang, E. McGlynn, R. Das, S. P. Paşca, B. Cui, and H. Heidari, "Nanotechnology enables novel modalities for neuromodulation," *Advanced Materials,* vol. 33, no. 52, p. 2103208, 2021, doi: 10.1002/adma.202103208.

[31] A. Barker, I. Freeston, R. Jalinous, and J. Jarratt, "Magnetic stimulation of the human brain and peripheral nervous system: an introduction and the results of an initial clinical evaluation," *Neurosurgery,* vol. 20, no. 1, pp. 100-109, 1987, doi: 10.1097/00006123-198701000-00024

[32] F. A. Somaa, T. A. de Graaf, and A. T. Sack, "Transcranial magnetic stimulation in the treatment of neurological diseases," *Frontiers in neurology,* vol. 13, p. 793253, 2022, doi: 10.3389/fneur.2022.793253.

[33] X. Zong, J. Gu, D. Geng, and D. Gao, "Repetitive transcranial magnetic stimulation (rTMS) for multiple neurological conditions in rodent animal models: A systematic review," *Neurochemistry international,* vol. 157, p. 105356, 2022, doi: 10.1016/j.neuint.2022.105356.

[34] O. Numssen, A.-L. Zier, A. Thielscher, G. Hartwigsen, T. R. Knösche, and K. Weise, "Efficient high-resolution TMS mapping of the human motor cortex by nonlinear regression," (in English), *NeuroImage (Orlando, Fla.),* vol. 245, pp. 118654-118654, 2021, doi: 10.1016/j.neuroimage.2021.118654.

[35] S. Minusa and T. Tateno, "Developing an implantable micro magnetic stimulation system to induce neural activity in Vivo," presented at the International Conference on Neural Information Processing, 2016.

[36] H. Tischler *et al.*, "Mini-coil for magnetic stimulation in the behaving primate," *Journal of neuroscience methods,* vol. 194, no. 2, pp. 242-251, 2011, doi: 10.1016/j.jneumeth.2010.10.015.

[37] G. Bonmassar, S. W. Lee, D. K. Freeman, M. Polasek, S. I. Fried, and J. T. Gale, "Microscopic magnetic stimulation of neural tissue," *Nature communications,* vol. 3, no. 1, pp. 1-10, 2012, doi: 10.1038/ncomms1914 (2012).

[38] H.-J. Park, G. Bonmassar, J. A. Kaltenbach, A. G. Machado, N. F. Manzoor, and J. T. Gale, "Activation of the central nervous system induced by micro-magnetic stimulation," *Nature communications,* vol. 4, no. 1, pp. 1-9, 2013, doi: 10.1038/ncomms3463 (2013).

[39] S. W. Lee and S. I. Fried, "Suppression of subthalamic nucleus activity by micromagnetic stimulation," *IEEE Transactions on Neural Systems and Rehabilitation Engineering,* vol. 23, no. 1, pp. 116-127, 2014, doi: 10.1109/TNSRE.2014.2348415.

[40] S. Mukesh, D. Blake, B. McKinnon, and P. Bhatti, "Modeling intracochlear magnetic stimulation: a Finite-Element Analysis," *IEEE Transactions on Neural Systems and Rehabilitation Engineering,* vol. 25, no. 8, pp. 1353-1362, 2016, doi: 10.1109/TNSRE.2016.2624275.

[41] S. W. Lee, F. Fallegger, B. D. F. Casse, and S. I. Fried, "Implantable microcoils for intracortical magnetic stimulation," *Science advances,* vol. 2, no. 12, p. e1600889, 2016, doi: 10.1126/sciadv.1600889.

[42] G. E. Salvi and U. Brägger, "Mechanical and technical risks in implant therapy," (in English), *The International journal of oral and maxillofacial implants,* vol. 24 Suppl, pp. 69-85, 2009. [Online]. Available: https://go.exlibris.link/vFCWD6C6.

[43] J. B. Weaver, A. M. Rauwerdink, and E. W. Hansen, "Magnetic nanoparticle temperature estimation," (in English), *Medical physics (Lancaster),* vol. 36, no. 5, pp. 1822-1829, 2009, doi: 10.1118/1.3106342.

[44] S. Mornet *et al.*, "Magnetic nanoparticle design for medical applications," (in English), *Progress in solid state chemistry,* vol. 34, no. 2, pp. 237-247, 2006, doi: 10.1016/j.progsolidstchem.2005.11.010.

[45] R. Hergt, S. Dutz, R. Müller, and M. Zeisberger, "Magnetic particle hyperthermia: nanoparticle magnetism and materials development for cancer therapy," (in English), *Journal of physics. Condensed matter,* vol. 18, no. 38, pp. S2919-S2934, 2006, doi: 10.1088/0953-8984/18/38/S26.

[46] I. Šafařík and M. Šafaříková, *Magnetic nanoparticles and biosciences*. Springer, 2002.

[47] Q. A. Pankhurst, J. Connolly, S. K. Jones, and J. Dobson, "Applications of magnetic nanoparticles in biomedicine," *Journal of physics D: Applied physics,* vol. 36, no. 13, p. R167, 2003, doi: 10.1088/0022-3727/36/13/201.

[48] M. M. Selim, S. El-Safty, A. Tounsi, and M. Shenashen, "A review of magnetic nanoparticles used in nanomedicine," vol. 12, ed: AIP Publishing LLC, 2024, pp. 010601-010601-14.

[49] H. Huang, S. Delikanli, H. Zeng, D. M. Ferkey, and A. Pralle, "Remote control of ion channels and neurons through magnetic-field heating of nanoparticles," *Nature nanotechnology,* vol. 5, no. 8, pp. 602-606, 2010, doi: 10.1038/nnano.2010.125.

[50] J.-H. Lee, J.-w. Kim, M. Levy, A. Kao, S.-h. Noh, D. Bozovic, and J. Cheon, "Magnetic nanoparticles for ultrafast mechanical control of inner ear hair cells," *ACS nano,* vol. 8, no. 7, pp. 6590-6598, 2014, doi: 10.1021/nn5020616.

[51] S. Hughes, A. J. El Haj, and J. Dobson, "Magnetic micro-and nanoparticle mediated activation of mechanosensitive ion channels," *Medical engineering & physics,* vol. 27, no. 9, pp. 754-762, 2005, doi: 10.1016/j.medengphy.2005.04.006.

[52] S. Hughes, S. McBain, J. Dobson, and A. J. El Haj, "Selective activation of mechanosensitive ion channels using magnetic particles," *Journal of the Royal Society Interface,* vol. 5, no. 25, pp. 855-863, 2008, doi: 10.1098/rsif.2007.1274.

[53] B. Coste *et al.*, "Piezo1 and Piezo2 are essential components of distinct mechanically activated cation channels," (in English), *Science (American Association for the Advancement of Science),* vol. 330, no. 6000, pp. 55-60, 2010, doi: 10.1126/science.1193270.

[54] S. A. Stanley, J. E. Gagner, S. Damanpour, M. Yoshida, J. S. Dordick, and J. M. Friedman, "Radio-wave heating of iron oxide nanoparticles can regulate plasma glucose in mice," *Science,* vol. 336, no. 6081, pp. 604-608, 2012, doi: 10.1126/science.1216753.

[55] E. A. Périgo, G. Hemery, O. Sandre, D. Ortega, E. Garaio, F. Plazaola, and F. J. Teran, "Fundamentals and advances in magnetic hyperthermia," (in English), *Applied physics reviews,* vol. 2, no. 4, p. 41302, 2015, doi: 10.1063/1.4935688.

[56] M. G. Christiansen, A. Senko, R. Chen, G. Romero, and P. Anikeeva, "Magnetically multiplexed heating of single domain nanoparticles," *Applied Physics Letters,* vol. 104, no. 21, 2014, doi: 10.1063/1.4879842.
[57] D. Gregurec *et al.*, "Magnetic vortex nanodiscs enable remote magnetomechanical neural stimulation," *ACS nano,* vol. 14, no. 7, pp. 8036-8045, 2020, doi: 10.1021/acsnano.0c00562.
[58] D. Rosenfeld *et al.*, "Transgene-free remote magnetothermal regulation of adrenal hormones," *Science advances,* vol. 6, no. 15, p. eaaz3734, 2020, doi: 10.1126/sciadv.aaz3734.
[59] S.-A. Hescham *et al.*, "Magnetothermal nanoparticle technology alleviates parkinsonian-like symptoms in mice," *Nature communications,* vol. 12, no. 1, p. 5569, 2021, doi: 10.1038/s41467-021-25837-4.
[60] C. Sebesta *et al.*, "Subsecond multichannel magnetic control of select neural circuits in freely moving flies," (in English), *Nature materials,* vol. 21, no. 8, pp. 951-958, 2022, doi: 10.1038/s41563-022-01281-7.
[61] "Deep Brain Magnetothermal Silencing of Dopaminergic Neurons via Endogenous TREK1 Channels Abolishes Place Preference in Mice," ed: NewsRX LLC, 2024, p. 1063.
[62] M. Kobayashi and A. Pascual-Leone, "Transcranial magnetic stimulation in neurology," *The Lancet Neurology,* vol. 2, no. 3, pp. 145-156, 2003, doi: 10.1016/S1474-4422(03)00321-1.
[63] A. Rotenberg, J. C. Horvath, and A. Pascual-Leone, "The transcranial magnetic stimulation (TMS) device and foundational techniques," in *Transcranial magnetic stimulation*: Springer, 2014, pp. 3-13.
[64] A. H. Iglesias, "Transcranial magnetic stimulation as treatment in multiple neurologic conditions," *Current neurology and neuroscience reports,* vol. 20, no. 1, pp. 1-9, 2020, doi: 10.1007/s11910-020-1021-0.
[65] B. He, *Neural engineering*. Springer, 2005.
[66] J. Selvaraj, P. Rastogi, N. Prabhu Gaunkar, R. L. Hadimani, and M. Mina, "Transcranial Magnetic Stimulation: Design of a Stimulator and a Focused Coil for the Application of Small Animals," *IEEE Transactions on Magnetics,* vol. 54, pp. 1-5, 2018.
[67] V. Walsh and M. Rushworth, "A primer of magnetic stimulation as a tool for neuropsychology," *Neuropsychologia,* 1999, doi: 10.1016/S0028-3932(98)00087-6.
[68] B. Guse, P. Falkai, and T. Wobrock, "Cognitive effects of high-frequency repetitive transcranial magnetic stimulation: a systematic review," *Journal of neural transmission,* vol. 117, pp. 105-122, 2010, doi: 10.1007/s00702-009-0333-7.
[69] A. Hufnagel, D. Clause, C. Brunhoelzl, and T. Sudhop, "Short-term memory: no evidence of effect of rapid-repetitive transcranial magnetic stimulation in healthy individuals," *Journal of neurology,* vol. 240, pp. 373-376, 1993, doi: 10.1007/BF00839970.
[70] A. Pascual-Leone *et al.*, "Safety of rapid-rate transcranial magnetic stimulation in normal volunteers," *Electroencephalography and Clinical Neurophysiology/Evoked Potentials Section,* vol. 89, no. 2, pp. 120-130, 1993, doi: 10.1016/0168-5597(93)90094-6.
[71] A. Pascual-Leone, A. Dhuna, B. Roth, L. Cohen, and M. Hallett, "Risk of burns during rapid-rate magnetic stimulation in presence of electrodes," *The Lancet,* vol. 336, no. 8724, pp. 1195-1196, 1990, doi: 10.1016/0140-6736(90)92815-Y.
[72] B. J. Roth, A. Pascual-Leone, L. G. Cohen, and M. Hallett, "The heating of metal electrodes during rapid-rate magnetic stimulation: a possible safety hazard," *Electroencephalography and Clinical Neurophysiology/Evoked Potentials Section,* vol. 85, no. 2, pp. 116-123, 1992, doi: 10.1016/0168-5597(92)90077-O.
[73] L. S. Pereira, V. T. Müller, M. da Mota Gomes, A. Rotenberg, and F. Fregni, "Safety of repetitive transcranial magnetic stimulation in patients with epilepsy: a systematic review," *Epilepsy & behavior,* vol. 57, pp. 167-176, 2016, doi: 10.1016/j.yebeh.2016.01.015.
[74] J.-P. Lefaucheur *et al.*, "Evidence-based guidelines on the therapeutic use of repetitive transcranial magnetic stimulation (rTMS)," *Clinical Neurophysiology,* vol. 125, no. 11, pp. 2150-2206, 2014, doi: 10.1016/j.clinph.2014.05.021.
[75] J.-P. Lefaucheur *et al.*, "Evidence-based guidelines on the therapeutic use of repetitive transcranial magnetic stimulation (rTMS): an update (2014–2018)," *Clinical neurophysiology,* vol. 131, no. 2, pp. 474-528, 2020, doi: 10.1016/j.clinph.2019.11.002.
[76] X. Che *et al.*, "High-frequency rTMS over the dorsolateral prefrontal cortex on chronic and provoked pain: A systematic review and meta-analysis," *Brain Stimulation,* vol. 14, no. 5, pp. 1135-1146, 2021, doi: 10.1016/j.brs.2021.07.004.

[77] G. Pateraki *et al.*, "Therapeutic application of rTMS in neurodegenerative and movement disorders: A review," *Journal of Electromyography and Kinesiology,* vol. 62, p. 102622, 2022, doi: 10.1016/j.jelekin.2021.102622.

[78] J. Zhang *et al.*, "Effects of repetitive transcranial magnetic stimulation (rTMS) on aphasia in stroke patients: A systematic review and meta-analysis," *Clinical Rehabilitation,* vol. 35, no. 8, pp. 1103-1116, 2021, doi: 10.1177/0269215521999554.

[79] M. Sommer, A. Alfaro, M. Rummel, S. Speck, N. Lang, T. Tings, and W. Paulus, "Half sine, monophasic and biphasic transcranial magnetic stimulation of the human motor cortex," *Clinical neurophysiology,* vol. 117, no. 4, pp. 838-844, 2006, doi: 10.1016/j.clinph.2005.10.029.

[80] K. Wendt, M. M. Sorkhabi, C. J. Stagg, M. K. Fleming, T. Denison, and J. O'Shea, "The effect of pulse shape in theta-burst stimulation: Monophasic vs biphasic TMS," *Brain Stimulation,* vol. 16, no. 4, pp. 1178-1185, 2023, doi: 10.1016/j.brs.2023.08.001.

[81] N. Arai, S. Okabe, T. Furubayashi, Y. Terao, K. Yuasa, and Y. Ugawa, "Comparison between short train, monophasic and biphasic repetitive transcranial magnetic stimulation (rTMS) of the human motor cortex," *Clinical neurophysiology,* vol. 116, no. 3, pp. 605-613, 2005, doi: 10.1016/j.clinph.2004.09.020.

[82] K. Rösler, C. Hess, R. Heckmann, and H. Ludin, "Significance of shape and size of the stimulating coil in magnetic stimulation of the human motor cortex," *Neuroscience letters,* vol. 100, no. 1-3, pp. 347-352, 1989, doi: 10.1016/0304-3940(89)90711-8.

[83] S. Ueno, T. Tashiro, and K. Harada, "Localized stimulation of neural tissues in the brain by means of a paired configuration of time-varying magnetic fields," *Journal of Applied Physics,* vol. 64, no. 10, pp. 5862-5864, 1988, doi: 10.1063/1.342181.

[84] L. G. Cohen *et al.*, "Effects of coil design on delivery of focal magnetic stimulation. Technical considerations," *Electroencephalography and clinical neurophysiology,* vol. 75, no. 4, pp. 350-357, 1990, doi: 10.1016/0013-4694(90)90113-X.

[85] D. Cohen and B. N. Cuffin, "Developing a more focal magnetic stimulator. Part I: Some basic principles," *Journal of Clinical Neurophysiology,* vol. 8, no. 1, pp. 102-111, 1991, doi: 10.1097/00004691-199101000-00013.

[86] K. Yunokuchi and D. Cohen, "Developing a more focal magnetic stimulator. Part II: Fabricating coils and measuring induced current distributions," *Journal of clinical neurophysiology: official publication of the American Electroencephalographic Society,* vol. 8, no. 1, pp. 112-120, 1991, doi: 10.1097/00004691-199101000-00014.

[87] G. G. Westin, B. D. Bassi, S. H. Lisanby, B. Luber, and N. U. New York State Psychiatric Institute, "Determination of motor threshold using visual observation overestimates transcranial magnetic stimulation dosage: Safety implications," (in English U6 - ctx_ver=Z39.88-2004&ctx_enc=info%3Aofi%2Fenc%3AUTF-8&rfr_id=info%3Asid%2Fsummon.serialssolutions.com&rft_val_fmt=info%3Aofi%2Ffmt%3Akev%3Amtx%3Ajournal&rft.genre=article&rft.atitle=Determination+of+motor+threshold+using+visual+observation+overestimates+transcranial+magnetic+stimulation+dosage%3A+Safety+implications&rft.jtitle=Clinical+neurophysiology&rft.au=Westin%2C+Gregory+G.&rft.au=Bassi%2C+Bruce+D.&rft.au=Lisanby%2C+Sarah+H.&rft.au=Luber%2C+Bruce&rft.date=2014-01-01&rft.pub=Elsevier+Ireland+Ltd&rft.issn=1388-2457&rft.eissn=1872-8952&rft.volume=125&rft.issue=1&rft.spage=142&rft.epage=147&rft_id=info:doi/10.1016%2Fj.clinph.2013.06.187&rft.externalDocID=S1388245713009450&paramdict=en-us U7 - Journal Article), *Clinical neurophysiology,* vol. 125, no. 1, pp. 142-147, 2014, doi: 10.1016/j.clinph.2013.06.187.

[88] K. Mills, S. Boniface, and M. Schubert, "Magnetic brain stimulation with a double coil: the importance of coil orientation," *Electroencephalography and clinical neurophysiology/Evoked potentials section,* vol. 85, no. 1, pp. 17-21, 1992, doi: 10.1016/0168-5597(92)90096-T.

[89] J. B. Silveira *et al.*, "Double cone coil repetitive transcranial magnetic stimulation for severe obsessive-compulsive disorder after reversible cerebral vasoconstriction syndrome with intracerebral hemorrhage: a case report," ed: SciELO Brasil, 2022.

[90] S. Vanneste and D. De Ridder, "Differences between a single session and repeated sessions of 1 Hz TMS by double-cone coil prefrontal stimulation for the improvement of tinnitus," *Brain Stimulation,* vol. 6, no. 2, pp. 155-159, 2013, doi: 10.1016/j.brs.2012.03.019.

[91] S. Vanneste, M. Plazier, P. Van de Heyning, and D. De Ridder, "Repetitive transcranial magnetic stimulation frequency dependent tinnitus improvement by double cone coil

prefrontal stimulation," *Journal of Neurology, Neurosurgery & Psychiatry,* vol. 82, no. 10, pp. 1160-1164, 2011, doi: 10.1136/jnnp.2010.213959.

[92] N. Branston and P. Tofts, "Analysis of the distribution of currents induced by a changing magnetic field in a volume conductor," *Physics in medicine & biology,* vol. 36, no. 2, p. 161, 1991, doi: 10.1088/0031-9155/36/2/001.

[93] P. Tofts, "The distribution of induced currents in magnetic stimulation of the nervous system," *Physics in Medicine & Biology,* vol. 35, no. 8, p. 1119, 1990, doi: 10.1088/0031-9155/35/8/008.

[94] C. Ren, P. P. Tarjan, and D. B. Popovic, "A novel electric design for electromagnetic stimulation-the slinky coil," *IEEE Transactions on Biomedical Engineering,* vol. 42, no. 9, pp. 918-925, 1995, doi: 10.1109/10.412658.

[95] K. P. Zimmermann and R. K. Simpson, ""“Slinky” coils for neuromagnetic stimulation," *Electroencephalography and Clinical Neurophysiology/Electromyography and Motor Control,* vol. 101, no. 2, pp. 145-152, 1996. 10.1016/0924-980X(95)00227-C.

[96] Y. Roth, A. Zangen, and M. Hallett, "A coil design for transcranial magnetic stimulation of deep brain regions," *Journal of Clinical Neurophysiology,* vol. 19, no. 4, pp. 361-370, 2002, doi: 10.1097/00004691-200208000-00008.

[97] A. Zangen, Y. Roth, B. Voller, and M. Hallett, "Transcranial magnetic stimulation of deep brain regions: evidence for efficacy of the H-coil," *Clinical neurophysiology,* vol. 116, no. 4, pp. 775-779, 2005, doi: 10.1016/j.clinph.2004.11.008.

[98] Y. Roth, A. Amir, Y. Levkovitz, and A. Zangen, "Three-dimensional distribution of the electric field induced in the brain by transcranial magnetic stimulation using figure-8 and deep H-coils," *Journal of Clinical Neurophysiology,* vol. 24, no. 1, pp. 31-38, 2007, doi: 10.1097/WNP.0b013e31802fa393.

[99] E. V. Harel, A. Zangen, Y. Roth, I. Reti, Y. Braw, and Y. Levkovitz, "H-coil repetitive transcranial magnetic stimulation for the treatment of bipolar depression: an add-on, safety and feasibility study," *The World Journal of Biological Psychiatry,* vol. 12, no. 2, pp. 119-126, 2011, doi: 10.3109/15622975.2010.510893.

[100] E. V. Harel, L. Rabany, L. Deutsch, Y. Bloch, A. Zangen, and Y. Levkovitz, "H-coil repetitive transcranial magnetic stimulation for treatment resistant major depressive disorder: an 18-week continuation safety and feasibility study," *The World Journal of Biological Psychiatry,* vol. 15, no. 4, pp. 298-306, 2014, doi: 10.3109/15622975.2011.639802.

[101] E. Onesti *et al.*, "H-coil repetitive transcranial magnetic stimulation for pain relief in patients with diabetic neuropathy," *European Journal of Pain,* vol. 17, no. 9, pp. 1347-1356, 2013, doi: 10.1002/j.1532-2149.2013.00320.x.

[102] Y. Meng, R. L. Hadimani, L. J. Crowther, Z. Xu, J. Qu, and D. Jiles, "Deep brain transcranial magnetic stimulation using variable “Halo coil” system," *Journal of Applied Physics,* vol. 117, no. 17, 2015.

[103] P. Rastogi, E. G. Lee, R. L. Hadimani, and D. C. Jiles, "Transcranial magnetic stimulation: Development of a novel deep-brain triple-halo coil," *IEEE Magnetics Letters,* vol. 10, pp. 1-5, 2019, doi: 10.1109/LMAG.2019.2903993.

[104] J. Ruohonen, P. Ravazzani, F. Grandori, and R. J. Ilmoniemi, "Theory of multichannel magnetic stimulation: toward functional neuromuscular rehabilitation," *IEEE Transactions on biomedical Engineering,* vol. 46, no. 6, pp. 646-651, 1999, doi: 10.1109/10.764941.

[105] B. H. Han, I. K. Chun, S. C. Lee, and S. Y. Lee, "Multichannel magnetic stimulation system design considering mutual couplings among the stimulation coils," *IEEE Transactions on Biomedical Engineering,* vol. 51, no. 5, pp. 812-817, 2004, doi: 10.1109/TBME.2004.824123.

[106] S. Yang, G. Xu, L. Wang, Y. Geng, H. Yu, and Q. Yang, "Circular coil array model for transcranial magnetic stimulation," *IEEE Transactions on Applied Superconductivity,* vol. 20, no. 3, pp. 829-833, 2010, doi: 10.1109/TASC.2010.2040379.

[107] X. Wei, Y. Li, M. Lu, J. Wang, and G. Yi, "Comprehensive survey on improved focality and penetration depth of transcranial magnetic stimulation employing multi-coil arrays," *International Journal of Environmental Research and Public Health,* vol. 14, no. 11, p. 1388, 2017, doi: 10.3390/ijerph14111388.

[108] S. W. Lee and S. I. Fried, "Magnetic stimulation of subthalamic nucleus neurons using micro-coils for deep brain stimulation," presented at the 2013 6th International IEEE/EMBS Conference on Neural Engineering (NER), 2013.

[109] S. W. Lee and S. I. Fried, "Enhanced Control of Cortical Pyramidal Neurons With Micromagnetic Stimulation," *IEEE Transactions on Neural Systems and Rehabilitation Engineering,* vol. 25, no. 9, pp. 1375-1386, 2017, doi: 10.1109/TNSRE.2016.2631446.
[110] M. Zaeimbashi, Z. Wang, S. W. Lee, S. Cash, S. Fried, and N. Sun, "Micro-solenoid inductors with magnetic core for neural stimulation," presented at the 2018 40th Annual International Conference of the IEEE Engineering in Medicine and Biology Society (EMBC), 2018.
[111] A. Khalifa *et al.*, "The development of microfabricated solenoids with magnetic cores for micromagnetic neural stimulation," *Microsystems & nanoengineering,* vol. 7, no. 1, p. 91, 2021, doi: 10.1038/s41378-021-00320-8.
[112] H. Ye, V. Hall, and J. Hendee, "Improving focality and consistency in micromagnetic stimulation," *Frontiers in Computational Neuroscience,* vol. 17, p. 1105505, 2023, doi: 10.3389/fncom.2023.1105505.
[113] S. Minusa, H. Osanai, and T. Tateno, "Micromagnetic stimulation of the mouse auditory cortex in vivo using an implantable solenoid system," *IEEE Transactions on Biomedical Engineering,* vol. 65, no. 6, pp. 1301-1310, 2017, doi: 10.1109/TBME.2017.2748136.
[114] R. Saha *et al.*, "Strength-frequency curve for micromagnetic neurostimulation through excitatory postsynaptic potentials (EPSPs) on rat hippocampal neurons and numerical modeling of magnetic microcoil (μcoil)," *Journal of neural engineering,* vol. 19, no. 1, p. 016018, 2022, doi: 10.1088/1741-2552/ac4baf.
[115] S. W. Lee and S. I. Fried, "Enhanced control of cortical pyramidal neurons with micromagnetic stimulation," *IEEE Transactions on Neural Systems and Rehabilitation Engineering,* vol. 25, no. 9, pp. 1375-1386, 2016, doi: 10.1109/TNSRE.2016.2631446.
[116] L. Golestanirad *et al.*, "Solenoidal micromagnetic stimulation enables activation of axons with specific orientation," *Frontiers in physiology,* vol. 9, p. 724, 2018, doi: 10.3389/fphys.2018.00724.
[117] G. Bonmassar and P. Serano, "MRI-induced heating of coils for microscopic magnetic stimulation at 1.5 tesla: An initial study," *Frontiers in human neuroscience,* vol. 14, p. 53, 2020, doi: 10.3389/fnhum.2020.00053.
[118] T. Kim *et al.*, "Thermal effects on neurons during stimulation of the brain," *Journal of neural engineering,* vol. 19, no. 5, p. 056029, 2022, doi: 10.1088/1741-2552/ac9339.
[119] M. Rizou and T. Prodromakis, "A planar micro-magnetic platform for stimulation of neural cells in vitro," presented at the 2016 IEEE Biomedical Circuits and Systems Conference (BioCAS), 2016.
[120] M.-E. Rizou and T. Prodromakis, "Magnetic stimulation in the microscale: the development of a 6× 6 array of micro-coils for stimulation of excitable cells in vitro," *Biomedical Physics & Engineering Express,* vol. 4, no. 2, p. 025016, 2018, doi: 10.1088/2057-1976/aaa0dd.
[121] G. Bonmassar, "Advancing coil design in micromagnetic brain stimulation," in *2017 International Conference on Electromagnetics in Advanced Applications (ICEAA)*, 2017: IEEE, pp. 1875-1878, doi: 10.1109/ICEAA.2017.8065671.
[122] G. Bonmassar, L. Golestanirad, and J. Deng, "Enhancing coil design for micromagnetic brain stimulation," *MRS advances,* vol. 3, no. 29, pp. 1635-1640, 2018, doi: 10.1557/adv.2018.155.
[123] R. Bernardo *et al.*, "Novel magnetic stimulation methodology for low-current implantable medical devices," *Medical Engineering & Physics,* vol. 73, pp. 77-84, 2019, doi: 10.1016/j.medengphy.2019.07.015.
[124] L. Tian, L. Song, Y. Zheng, J. Wang, and H. Chen, "An improved F/C structure for cell-scale micro-magnetic coil," *IEEE Transactions on Magnetics,* vol. 56, no. 8, pp. 1-8, 2020, doi: 10.1109/TMAG.2020.2996955.
[125] H. Jeong, A. Cho, I. Ay, and G. Bonmassar, "Short-pulsed micro-magnetic stimulation of the vagus nerve," *Frontiers in Physiology,* vol. 13, p. 938101, 2022, doi: 10.3389/fphys.2022.938101.
[126] H. Jeong, J. Deng, and G. Bonmassar, "Planar figure-8 coils for ultra-focal and directional micromagnetic brain stimulation," *Journal of Vacuum Science & Technology B,* vol. 39, no. 6, 2021, doi: 10.1116/6.0001281.
[127] H.-J. Park, J. H. Seol, J. Ku, and S. Kim, "Computational Study on the Thermal Effects of Implantable Magnetic Stimulation Based on Planar Coils," (in English), *IEEE transactions on biomedical engineering,* vol. 63, no. 1, pp. 158-167, 2016, doi: 10.1109/TBME.2015.2490244.

[128] C. Ge, F. Walton, W. Xu, and H. Heidari, "Orientationally Selective micro-Coil Design of Intracortical Magnetic Neurostimulation," 2022, 2022. [Online]. Available: https://go.exlibris.link/mr70qX2w.
[129] S. B. Ryu *et al.*, "Spatially confined responses of mouse visual cortex to intracortical magnetic stimulation from micro-coils," *Journal of neural engineering,* vol. 17, no. 5, p. 056036, 2020, doi: 10.1088/1741-2552/abbd22.
[130] E. C. Szoka *et al.*, "Neural Probe Utilizing Programmable Micro-coil Magnetic Stimulation," presented at the 2021 10th International IEEE/EMBS Conference on Neural Engineering (NER), 2021.
[131] S. W. Lee and S. I. Fried, "Micro-magnetic stimulation of primary visual cortex induces focal and sustained activation of secondary visual cortex," *Philosophical Transactions of the Royal Society A,* vol. 380, no. 2228, p. 20210019, 2022, doi: 10.1098/rsta.2021.0019.
[132] K. Thyagarajan *et al.*, "Micro-coil probes for magnetic intracortical neural stimulation: Trade-offs in materials and design," *APL materials,* vol. 9, no. 1, 2021, doi: 10.1063/5.0023486.
[133] A. J. Whalen and S. I. Fried, "Thermal safety considerations for implantable micro-coil design," *Journal of Neural Engineering,* 2023, doi: 10.1088/1741-2552/ace79a.
[134] G. Bonmassar, J. Gale, and W. Vanduffel, "Optimizing Microscopic Magnetic Fields for Neuronal Stimulation," *International Journal of Bioelectromagnetism,* vol. 16, no. 1, 2014.
[135] M. E. Rizou and T. Prodromakis, "Magnetic stimulation in the microscale: the development of a 6 × 6 array of micro-coils for stimulation of excitable cells in vitro," (in English), *Biomedical physics & engineering express,* vol. 4, no. 2, p. 25016, 2018, doi: 10.1088/2057-1976/aaa0dd.
[136] S. Minusa, S. Muramatsu, H. Osanai, and T. Tateno, "A multichannel magnetic stimulation system using submillimeter-sized coils: system development and experimental application to rodent brain in vivo," *Journal of neural engineering,* vol. 16, no. 6, p. 066014, 2019, doi: 10.1088/1741-2552/ab3187.
[137] Y. Zheng, Q. Liu, Y. Zhao, Y. Qi, and L. Dong, "Design of a 1 × 4 micro-magnetic stimulation device and its targeted, coordinated regulation on LTP of Schaffer-CA1 in the hippocampus of rats," *Methods,* vol. 229, pp. 49-60, 2024/09/01/ 2024, doi: 10.1016/j.ymeth.2024.06.004.
[138] S. W. Lee, "Selective activation of cortical columns using multichannel magnetic stimulation with a bent flat microwire array," *IEEE Transactions on Biomedical Engineering,* vol. 68, no. 7, pp. 2164-2175, 2020, doi: 10.1109/TBME.2020.3033491.
[139] V. Raghuram, A. D. Datye, S. I. Fried, and B. P. Timko, "Transparent and Conformal Microcoil Arrays for Spatially Selective Neuronal Activation," *bioRxiv,* p. 2021.12. 07.471184, 2021, doi: 10.1101/2021.12.07.471184.
[140] S. Sugai, H. Higuchi, J. Nishikawa, K. Satoh, S. Murakami, and T. Tateno, "Numerical Analysis of Microcoil-Induced Electric Fields and Evaluation of In vivo Magnetic Stimulation of the Mouse Brain," *IEEJ Transactions on Electrical and Electronic Engineering,* vol. 15, no. 11, pp. 1672-1680, 2020, doi: 10.1002/tee.23237.
[141] G. Bonmassar, S. W. Lee, D. K. Freeman, M. Polasek, S. I. Fried, and J. T. Gale, "Microscopic magnetic stimulation of neural tissue," *Nature communications,* vol. 3, no. 1, p. 921, 2012, doi: 10.1038/ncomms1914 (2012).
[142] S. W. Lee and S. I. Fried, "The response of L5 pyramidal neurons of the PFC to magnetic stimulation from a micro-coil," in *2014 36th Annual International Conference of the IEEE Engineering in Medicine and Biology Society*, 2014: IEEE, pp. 6125-6128, doi: 10.1109/EMBC.2014.6945027.
[143] M. P. Calatayud, B. Sanz, V. Raffa, C. Riggio, M. R. Ibarra, and G. F. Goya, "The effect of surface charge of functionalized Fe3O4 nanoparticles on protein adsorption and cell uptake," (in English), *Biomaterials,* vol. 35, no. 24, pp. 6389-6399, 2014, doi: 10.1016/j.biomaterials.2014.04.009.
[144] S. A. Blank-Shim *et al.*, "Binding patterns of homo-peptides on bare magnetic nanoparticles: insights into environmental dependence," (in English), *Scientific reports,* vol. 7, no. 1, pp. 14047-11, 2017, doi: 10.1038/s41598-017-13928-6.
[145] R. Weissleder, K. Kelly, E. Y. Sun, T. Shtatland, and L. Josephson, "Cell-specific targeting of nanoparticles by multivalent attachment of small molecules," (in English), *Nature biotechnology,* vol. 23, no. 11, pp. 1418-1423, 2005, doi: 10.1038/nbt1159.

[146] J.-w. Kim, H.-k. Jeong, K. M. Southard, Y.-w. Jun, and J. Cheon, "Magnetic Nanotweezers for Interrogating Biological Processes in Space and Time," (in English), *Accounts of chemical research,* vol. 51, no. 4, pp. 839-849, 2018, doi: 10.1021/acs.accounts.8b00004.
[147] J. Dobson, "Remote control of cellular behaviour with magnetic nanoparticles," *Nature nanotechnology,* vol. 3, no. 3, pp. 139-143, 2008, doi: 10.1038/nnano.2008.39.
[148] D. Ortega and Q. A. Pankhurst, "Magnetic hyperthermia," *Nanoscience,* vol. 1, no. 60, p. e88, 2013, doi: 10.1039/9781849734844-00060.
[149] A. E. Deatsch and B. A. Evans, "Heating efficiency in magnetic nanoparticle hyperthermia," (in English), *Journal of magnetism and magnetic materials,* vol. 354, pp. 163-172, 2014, doi: 10.1016/j.jmmm.2013.11.006.
[150] K. Mahmoudi, A. Bouras, D. Bozec, R. Ivkov, and C. Hadjipanayis, "Magnetic hyperthermia therapy for the treatment of glioblastoma: a review of the therapy's history, efficacy and application in humans," *International Journal of Hyperthermia,* vol. 34, no. 8, pp. 1316-1328, 2018, doi: 10.1080/02656736.2018.1430867.
[151] R. Chen, G. Romero, M. G. Christiansen, A. Mohr, and P. Anikeeva, "Wireless magnetothermal deep brain stimulation," (in English), *Science (American Association for the Advancement of Science),* vol. 347, no. 6229, pp. 1477-1480, Mar 27 2015, doi: 10.1126/science.1261821.
[152] R. Munshi, S. M. Qadri, Q. Zhang, I. Castellanos Rubio, P. Del Pino, and A. Pralle, "Magnetothermal genetic deep brain stimulation of motor behaviors in awake, freely moving mice," (in English), *eLife,* vol. 6, 2017, doi: 10.7554/eLife.27069.
[153] D. Rosenfeld, H. Field, Y. J. Kim, K. K. L. Pang, K. Nagao, F. Koehler, and P. Anikeeva, "Magnetothermal Modulation of Calcium‐Dependent Nerve Growth," (in English), *Advanced functional materials,* vol. 32, no. 50, pp. n/a-n/a, 2022, doi: 10.1002/adfm.202204558.
[154] D. Rosenfeld *et al.*, "Transgene-free remote magnetothermal regulation of adrenal hormones," (in English), *Science advances,* vol. 6, no. 15, pp. eaaz3734-eaaz3734, 2020, doi: 10.1126/sciadv.aaz3734.
[155] P. Chandrasekharan *et al.*, "Using magnetic particle imaging systems to localize and guide magnetic hyperthermia treatment: tracers, hardware, and future medical applications," (in English), *Theranostics,* vol. 10, no. 7, pp. 2965-2981, 2020, doi: 10.7150/thno.40858.
[156] S. Min *et al.*, "Remote Control of Time‐Regulated Stretching of Ligand‐Presenting Nanocoils In Situ Regulates the Cyclic Adhesion and Differentiation of Stem Cells," *Advanced Materials,* vol. 33, no. 11, p. 2008353, 2021, doi: 10.1002/adma.202008353.
[157] S. Min *et al.*, "Independent Tuning of Nano‐Ligand Frequency and Sequences Regulates the Adhesion and Differentiation of Stem Cells," *Advanced Materials,* vol. 32, no. 40, p. 2004300, 2020, doi: 10.1002/adma.202004300.
[158] L. S. Ganapathe, M. A. Mohamed, R. Mohamad Yunus, and D. D. Berhanuddin, "Magnetite (Fe3O4) nanoparticles in biomedical application: From synthesis to surface functionalisation," *Magnetochemistry,* vol. 6, no. 4, p. 68, 2020, doi: 10.3390/magnetochemistry6040068.
[159] M. D. Nguyen, H.-V. Tran, S. Xu, and T. R. Lee, "Fe3O4 Nanoparticles: Structures, synthesis, magnetic properties, surface functionalization, and emerging applications," *Applied Sciences,* vol. 11, no. 23, p. 11301, 2021, doi: 10.3390/app112311301.
[160] K. N. Koo, A. F. Ismail, M. H. D. Othman, N. Bidin, and M. A. Rahman, "Preparation and characterization of superparamagnetic magnetite (Fe3O4) nanoparticles: A short review," *Malaysian Journal of Fundamental and Applied Sciences,* vol. 15, no. 1, pp. 23-31, 2019, doi: 10.11113/MJFAS.V15N2019.1224.
[161] N. Tran and T. J. Webster, "Magnetic nanoparticles: biomedical applications and challenges," (in English), *Journal of materials chemistry,* vol. 20, no. 40, pp. 8760-8767, 2010, doi: 10.1039/c0jm00994f.
[162] M. Srivastava, S. Alla, S. S. Meena, N. Gupta, R. Mandal, and N. Prasad, "Zn x Fe 3− x O 4 ($0.01 \leqslant x \leqslant 0.8$) nanoparticles for controlled magnetic hyperthermia application," *New Journal of Chemistry,* vol. 42, no. 9, pp. 7144-7153, 2018, doi: 10.1039/C8NJ00547H
[163] P. Saha, R. Rakshit, and K. Mandal, "Enhanced magnetic properties of Zn doped Fe3O4 nano hollow spheres for better bio-medical applications," *Journal of magnetism and magnetic materials,* vol. 475, pp. 130-136, 2019, doi: 10.1016/j.jmmm.2018.11.061.
[164] J. t. Jang, H. Nah, J. H. Lee, S. H. Moon, M. G. Kim, and J. Cheon, "Critical enhancements of MRI contrast and hyperthermic effects by dopant‐controlled magnetic nanoparticles,"

Angewandte Chemie International Edition, vol. 48, no. 7, pp. 1234-1238, 2009, doi: 10.1002/anie.200805149.

[165] K. Chatterjee, S. Sarkar, K. Jagajjanani Rao, and S. Paria, "Core/shell nanoparticles in biomedical applications," (in English), *Advances in colloid and interface science,* vol. 209, pp. 8-39, 2014, doi: 10.1016/j.cis.2013.12.008.

[166] L.-M. Lacroix, N. Frey Huls, D. Ho, X. Sun, K. Cheng, and S. Sun, "Stable single-crystalline body centered cubic Fe nanoparticles," *Nano letters,* vol. 11, no. 4, pp. 1641-1645, 2011, doi: 10.1021/nl200110t.

[167] L. D. Marks and L. Peng, "Nanoparticle shape, thermodynamics and kinetics," (in English), *Journal of physics. Condensed matter,* vol. 28, no. 5, pp. 053001-053001, 2016, doi: 10.1088/0953-8984/28/5/053001.

[168] K. L. Kelly, E. Coronado, L. L. Zhao, and G. C. Schatz, "The Optical Properties of Metal Nanoparticles: The Influence of Size, Shape, and Dielectric Environment," (in English), *The journal of physical chemistry. B,* vol. 107, no. 3, pp. 668-677, 2003, doi: 10.1021/jp026731y.

[169] Z. Nemati, S. Salili, J. Alonso, A. Ataie, R. Das, M. Phan, and H. Srikanth, "Superparamagnetic iron oxide nanodiscs for hyperthermia therapy: Does size matter?," *Journal of Alloys and Compounds,* vol. 714, pp. 709-714, 2017, doi: 10.1016/j.jallcom.2017.04.211.

[170] R. G. D. Andrade, S. R. S. Veloso, and E. M. S. Castanheira, "Shape Anisotropic Iron Oxide-Based Magnetic Nanoparticles: Synthesis and Biomedical Applications," (in English), *International journal of molecular sciences,* vol. 21, no. 7, p. 2455, 2020, doi: 10.3390/ijms21072455.

[171] D. Lisjak and A. Mertelj, "Anisotropic magnetic nanoparticles: A review of their properties, syntheses and potential applications," (in English), *Progress in materials science,* vol. 95, pp. 286-328, 2018, doi: 10.1016/j.pmatsci.2018.03.003.

[172] J. Borch and T. Hamann, "The nanodisc: a novel tool for membrane protein studies," 2009, doi: 10.1515/BC.2009.091.

[173] G. Zou, K. Xiong, C. Jiang, H. Li, Y. Wang, S. Zhang, and Y. Qian, "Magnetic Fe3O4 nanodisc synthesis on a large scale via a surfactant-assisted process," *Nanotechnology,* vol. 16, no. 9, p. 1584, 2005, doi: 10.1088/0957-4484/16/9/030.

[174] M. Hilse *et al.*, "GaAs–Fe3Si core–shell nanowires: Nanobar magnets," *Nano letters,* vol. 13, no. 12, pp. 6203-6209, 2013, doi: 10.1021/nl4035994.

[175] T. Zhang *et al.*, "Co@ C nanorods as both magnetic stirring nanobars and magnetic recyclable nanocatalysts for microcatalytic reactions," *Applied Catalysis B: Environmental,* vol. 304, p. 120925, 2022, doi: 10.1016/j.apcatb.2021.120925.

[176] L. Signorelli, S.-A. Hescham, A. Pralle, and D. Gregurec, "Magnetic nanomaterials for wireless thermal and mechanical neuromodulation," (in English), *iScience,* vol. 25, no. 11, pp. 105401-105401, 2022, doi: 10.1016/j.isci.2022.105401.

[177] S. Bevan, T. Quallo, and D. A. Andersson, "Trpv1," *Mammalian Transient Receptor Potential (TRP) Cation Channels: Volume I,* pp. 207-245, 2014, doi: 10.1007/978-3-642-54215-2_9.

[178] M. Tominaga and T. Tominaga, "Structure and function of TRPV1," (in English), *Pflügers Archiv,* vol. 451, no. 1, pp. 143-150, 2005, doi: 10.1007/s00424-005-1457-8.

[179] T. D. Plant and R. Strotmann, "TRPV4," (in English), *Handbook of experimental pharmacology,* no. 179, p. 189, 2007, doi: 10.1007/978-3-540-34891-7_11.

[180] M.-K. Chung, H. Lee, and M. J. Caterina, "Warm Temperatures Activate TRPV4 in Mouse 308 Keratinocytes," (in English), *The Journal of biological chemistry,* vol. 278, no. 34, pp. 32037-32046, 2003, doi: 10.1074/jbc.M303251200.

[181] H. Todaka, J. Taniguchi, J.-i. Satoh, A. Mizuno, and M. Suzuki, "Warm Temperature-sensitive Transient Receptor Potential Vanilloid 4 (TRPV4) Plays an Essential Role in Thermal Hyperalgesia," (in English), *The Journal of biological chemistry,* vol. 279, no. 34, pp. 35133-35138, 2004, doi: 10.1074/jbc.M406260200.

[182] E. R. Schneider, E. O. Anderson, E. O. Gracheva, and S. N. Bagriantsev, "Temperature sensitivity of two-pore (K2P) potassium channels," *Current topics in membranes,* vol. 74, pp. 113-133, 2014, doi: 10.1016/B978-0-12-800181-3.00005-1.

[183] F. N. Hamada, M. Rosenzweig, K. Kang, S. R. Pulver, A. Ghezzi, T. J. Jegla, and P. A. Garrity, "internal thermal sensor controlling temperature preference in Drosophila," (in English), *Nature,* vol. 454, no. 7201, pp. 217-220, 2008, doi: 10.1038/nature07001.

[184] M. Rosenzweig, K. M. Brennan, T. D. Tayler, P. O. Phelps, A. Patapoutian, and P. A. Garrity, "The Drosophila ortholog of vertebrate TRPA1 regulates thermotaxis," (in English), *Genes & development,* vol. 19, no. 4, pp. 419-424, 2005, doi: 10.1101/gad.1278205.
[185] Y. Yu *et al.*, "Remote and selective control of astrocytes by magnetomechanical stimulation," *Advanced Science,* vol. 9, no. 6, p. 2104194, 2022, doi: 10.1002/advs.202104194.
[186] M. Szczot, A. R. Nickolls, R. M. Lam, and A. T. Chesler, "The Form and Function of PIEZO2," (in English), *Annual review of biochemistry,* vol. 90, no. 1, pp. 507-534, 2021, doi: 10.1146/annurev-biochem-081720-023244.
[187] Y.-C. Lin, Y. R. Guo, A. Miyagi, J. Levring, R. MacKinnon, and S. Scheuring, "Force-induced conformational changes in PIEZO1," (in English), *Nature (London),* vol. 573, no. 7773, pp. 230-234, 2019, doi: 10.1038/s41586-019-1499-2.
[188] P. A. Gottlieb, C. Bae, and F. Sachs, "Gating the mechanical channel Piezo1: A comparison between whole-cell and patch recording," (in English), *Channels (Austin, Tex.),* vol. 6, no. 4, pp. 282-289, 2012, doi: 10.4161/chan.21064.
[189] Y. Jiang, X. Yang, J. Jiang, and B. Xiao, "Structural Designs and Mechanogating Mechanisms of the Mechanosensitive Piezo Channels," (in English), *Trends in biochemical sciences (Amsterdam. Regular ed.),* vol. 46, no. 6, pp. 472-488, 2021, doi: 10.1016/j.tibs.2021.01.008.
[190] Y. R. Guo and R. MacKinnon, "Structure-based membrane dome mechanism for Piezo mechanosensitivity," (in English), *eLife,* vol. 6, 2017, doi: 10.7554/eLife.33660.
[191] G. Calixto, J. Bernegossi, B. Fonseca-Santos, and M. Chorilli, "Nanotechnology-based drug delivery systems for treatment of oral cancer: a review," *International journal of nanomedicine,* pp. 3719-3735, 2014, doi: 10.2147/IJN.S61670.
[192] A. Garcia-Elias, S. Mrkonjić, C. Jung, C. Pardo-Pastor, R. Vicente, and M. A. Valverde, "The TRPV4 channel," (in English), *Handbook of experimental pharmacology,* vol. 222, p. 293, 2014, doi: 10.1007/978-3-642-54215-2_12.
[193] G. Du *et al.*, "Roles of TRPV4 and piezo channels in stretch-evoked Ca2+ response in chondrocytes," (in English), *Experimental biology and medicine (Maywood, N.J.),* vol. 245, no. 3, pp. 180-189, 2020, doi: 10.1177/1535370219892601.
[194] J. M. Kanczler, H. S. Sura, J. Magnay, D. Green, R. O. Oreffo, J. P. Dobson, and A. J. El Haj, "Controlled differentiation of human bone marrow stromal cells using magnetic nanoparticle technology," *Tissue engineering Part A,* vol. 16, no. 10, pp. 3241-3250, 2010, doi: 10.1089/ten.tea.2009.0638.
[195] F. Maingret, M. Fosset, F. Lesage, M. Lazdunski, and E. Honoré, "TRAAK Is a Mammalian Neuronal Mechano-gated K+Channel," (in English), *The Journal of biological chemistry,* vol. 274, no. 3, pp. 1381-1387, 1999, doi: 10.1074/jbc.274.3.1381.
[196] S. G. Brohawn, E. B. Campbell, and R. MacKinnon, "Physical mechanism for gating and mechanosensitivity of the human TRAAK K+ channel," (in English), *Nature (London),* vol. 516, no. 7529, pp. 126-130, 2014, doi: 10.1038/nature14013.
[197] J. McCarthy, X. Gong, D. Nahirney, M. Duszyk, and M. Radomski, "Polystyrene nanoparticles activate ion transport in human airway epithelial cells," *International journal of nanomedicine,* pp. 1343-1356, 2011, doi: 10.2147/IJN.S21145.
[198] P. Huang, H. C. Chan, W. K. Zhang, D. Wang, Y. Duan, and M. M. T. Loy, "Mechanosensitive gating of CFTR," (in English), *Nature cell biology,* vol. 12, no. 5, pp. 507-512, 2010, doi: 10.1038/ncb2053.
[199] Y. Yu *et al.*, "Remote and Selective Control of Astrocytes by Magnetomechanical Stimulation," (in English), *Advanced science,* vol. 9, no. 6, pp. e2104194-n/a, 2022, doi: 10.1002/advs.202104194.
[200] C.-L. Su, C.-C. Cheng, P.-H. Yen, J.-X. Huang, Y.-J. Ting, and P.-H. Chiang, "Wireless neuromodulation in vitro and in vivo by intrinsic TRPC-mediated magnetomechanical stimulation," (in English), *Communications biology,* vol. 5, no. 1, pp. 1166-1166, 2022, doi: 10.1038/s42003-022-04124-y.
[201] J.-H. Lee *et al.*, "Exchange-coupled magnetic nanoparticles for efficient heat induction," *Nature nanotechnology,* vol. 6, no. 7, pp. 418-422, 2011, doi: 10.1038/nnano.2011.95.
[202] D. Yoo, J.-H. Lee, T.-H. Shin, and J. Cheon, "Theranostic magnetic nanoparticles," *Accounts of chemical research,* vol. 44, no. 10, pp. 863-874, 2011, doi: 10.1021/ar200085c.
[203] L. Chen, C. Chen, P. Wang, and T. Song, "Mechanisms of cellular effects directly induced by magnetic nanoparticles under magnetic fields," *Journal of nanomaterials,* vol. 2017, 2017, doi: 10.1155/2017/1564634.

[204] J.-u. Lee *et al.*, "Non-contact long-range magnetic stimulation of mechanosensitive ion channels in freely moving animals," *Nature materials,* vol. 20, no. 7, pp. 1029-1036, 2021, doi: 10.1038/s41563-020-00896-y.
[205] "BRAINSTORM PROJECT." https://www.brainstorm-project.eu/ https://cordis.europa.eu/project/id/101099355 (accessed December, 2023).
[206] S. Wu *et al.*, "Genetically magnetic control of neural system via TRPV4 activation with magnetic nanoparticles," *Nano Today,* vol. 39, p. 101187, 2021, doi: 10.1016/j.nantod.2021.101187.
[207] H. Kim, J. Kim, J. Kim, S. Oh, K. Choi, and J. Yoon, "Magnetothermal-based non-invasive focused magnetic stimulation for functional recovery in chronic stroke treatment," (in English), *Scientific reports,* vol. 13, no. 1, pp. 4988-4988, 2023, doi: 10.1038/s41598-023-31979-w.
[208] Z. Wang, "Microsystems using three-dimensional integration and TSV technologies: Fundamentals and applications," *Microelectronic Engineering,* vol. 210, pp. 35-64, 2019/04/01/ 2019, doi: 10.1016/j.mee.2019.03.009.
[209] O. Seong Joon, K. Chunho, and D. F. Baldwin, "High density, high aspect ratio through-wafer electrical interconnect vias for MEMS packaging," *IEEE Transactions on Advanced Packaging,* vol. 26, no. 3, pp. 302-309, 2003, doi: 10.1109/TADVP.2003.818060.
[210] E. M. Chow, V. Chandrasekaran, A. Partridge, T. Nishida, M. Sheplak, C. F. Quate, and T. W. Kenny, "Process compatible polysilicon-based electrical through-wafer interconnects in silicon substrates," *Journal of Microelectromechanical Systems,* vol. 11, no. 6, pp. 631-640, 2002, doi: 10.1109/JMEMS.2002.805206.
[211] P. Dixit, J. Miao, and R. Preisser, "Fabrication of High Aspect Ratio 35 μm Pitch Through-Wafer Copper Interconnects by Electroplating for 3-D Wafer Stacking," *Electrochemical and Solid-State Letters,* vol. 9, no. 10, p. G305, 2006/08/01 2006, doi: 10.1149/1.2236374.
[212] G. Parès *et al.*, "Mid-process through silicon vias technology using tungsten metallization: Process optimazation and electrical results," in *2009 11th Electronics Packaging Technology Conference*, 9-11 Dec. 2009 2009, pp. 772-777, doi: 10.1109/EPTC.2009.5416444.
[213] T. Xu, J. Sun, H. Wu, H. Li, H. Li, and Z. Tao, "3D MEMS In-Chip Solenoid Inductor With High Inductance Density for Power MEMS Device," *IEEE Electron Device Letters,* vol. 40, no. 11, pp. 1816-1819, 2019, doi: 10.1109/LED.2019.2941003.
[214] R. Ballarini, H. Kahn, A. H. Heuer, M. P. De Boer, and M. T. Dugger, "8.09 - MEMS Structures for On-chip Testing of Mechanical and Surface Properties of Thin Films," in *Comprehensive Structural Integrity*, I. Milne, R. O. Ritchie, and B. Karihaloo Eds. Oxford: Pergamon, 2003, pp. 325-356.
[215] M. Javaid, A. Haleem, R. P. Singh, R. Suman, and S. Rab, "Role of additive manufacturing applications towards environmental sustainability," *Advanced Industrial and Engineering Polymer Research,* vol. 4, no. 4, pp. 312-322, 2021/10/01/ 2021, doi: 10.1016/j.aiepr.2021.07.005.
[216] J. M. Bustillo, R. T. Howe, and R. S. Muller, "Surface micromachining for microelectromechanical systems," *Proceedings of the IEEE,* vol. 86, no. 8, pp. 1552-1574, 1998, doi: 10.1109/5.704260.
[217] D.-M. Fang, Y. Zhou, W. Ding, X.-N. Wang, and X.-L. Zhao, *Surface micromachined three-dimentional solenoid-type inductor* (4M 2006 - Second International Conference on Multi-Material Micro Manufacture). Oxford: Elsevier, 2006, pp. 103-106.
[218] Y. Jun-Bo, C. Yun-Seok, K. Byeong-Il, E. Yunseong, and Y. Euisik, "CMOS-compatible surface-micromachined suspended-spiral inductors for multi-GHz silicon RF ICs," *IEEE Electron Device Letters,* vol. 23, no. 10, pp. 591-593, 2002, doi: 10.1109/LED.2002.803767.
[219] K. Yong-Jun and M. G. Allen, "Surface micromachined solenoid inductors for high frequency applications," *IEEE Transactions on Components, Packaging, and Manufacturing Technology: Part C,* vol. 21, no. 1, pp. 26-33, 1998, doi: 10.1109/3476.670025.
[220] M. Wang, J. Li, K. D. T. Ngo, and H. Xie, "A Surface-Mountable Microfabricated Power Inductor in Silicon for Ultracompact Power Supplies," *IEEE Transactions on Power Electronics,* vol. 26, no. 5, pp. 1310-1315, 2011, doi: 10.1109/TPEL.2010.2047406.
[221] Y. Jun-Bo, K. Bon-Kee, H. Chul-Hi, Y. Euisik, and K. Choong-Ki, "Surface micromachined solenoid on-Si and on-glass inductors for RF applications," *IEEE Electron Device Letters,* vol. 20, no. 9, pp. 487-489, 1999, doi: 10.1109/55.784461.

[222] Y. Shim, Z. Wu, and M. Rais-Zadeh, "A Multimetal Surface Micromachining Process for Tunable RF MEMS Passives," *Journal of Microelectromechanical Systems,* vol. 21, no. 4, pp. 867-874, 2012, doi: 10.1109/JMEMS.2012.2192911.

[223] P. Jin-Woo, F. Cros, and M. G. Allen, "A sacrificial layer approach to highly laminated magnetic cores," in *Technical Digest. MEMS 2002 IEEE International Conference. Fifteenth IEEE International Conference on Micro Electro Mechanical Systems (Cat. No.02CH37266)*, 24-24 Jan. 2002 2002, pp. 380-383, doi: 10.1109/MEMSYS.2002.984282.

[224] M. Gel, S. Takeuchi, and I. Shimoyama, "Fabrication method for out-of-plane, micro-coil by surface micromachining," *Sensors and Actuators A: Physical,* vol. 97-98, pp. 702-708, 2002/04/01/ 2002, doi: 10.1016/S0924-4247(02)00007-9.

[225] D. R. Hines, N. P. Siwak, L. A. Mosher, and R. Ghodssi, "MEMS Lithography and Micromachining Techniques," in *MEMS Materials and Processes Handbook*, R. Ghodssi and P. Lin Eds. Boston, MA: Springer US, 2011, pp. 667-753.

[226] G. N. Levy, R. Schindel, and J. P. Kruth, "RAPID MANUFACTURING AND RAPID TOOLING WITH LAYER MANUFACTURING (LM) TECHNOLOGIES, STATE OF THE ART AND FUTURE PERSPECTIVES," *CIRP Annals,* vol. 52, no. 2, pp. 589-609, 2003/01/01/ 2003, doi: 10.1016/S0007-8506(07)60206-6.

[227] K. Wang, Q. Ma, C.-X. Qu, H.-T. Zhou, M. Cao, and S.-D. Wang, "Review on 3D Fabrication at Nanoscale," *AUTEX Research Journal,* vol. 23, no. 3, pp. 350-369, 2023, doi: 10.2478/aut-2022-0014.

[228] D. Qin, Y. Xia, and G. M. Whitesides, "Soft lithography for micro- and nanoscale patterning," *Nature Protocols,* vol. 5, no. 3, pp. 491-502, 2010/03/01 2010, doi: 10.1038/nprot.2009.234.

[229] R. A. Lawson and A. P. G. Robinson, "Chapter 1 - Overview of materials and processes for lithography," in *Frontiers of Nanoscience*, vol. 11, A. Robinson and R. Lawson Eds.: Elsevier, 2016, pp. 1-90.

[230] A. Tritchkov, R. Jonckheere, and L. Van den hove, "Use of positive and negative chemically amplified resists in electron-beam direct-write lithography," *Journal of Vacuum Science & Technology B: Microelectronics and Nanometer Structures Processing, Measurement, and Phenomena,* vol. 13, no. 6, pp. 2986-2993, 1995, doi: 10.1116/1.588293.

[231] S. Ghosh, C. P. Pradeep, S. K. Sharma, P. G. Reddy, S. P. Pal, and K. E. Gonsalves, "Recent advances in non-chemically amplified photoresists for next generation IC technology," *RSC advances,* vol. 6, no. 78, pp. 74462-74481, 2016, doi: 10.1039/C6RA12077F.

[232] E. H. Waller and G. v. Freymann, "From photoinduced electron transfer to 3D metal microstructures via direct laser writing," *Nanophotonics,* vol. 7, no. 7, pp. 1259-1277, 2018, doi: 10.1515/nanoph-2017-0134.

[233] X. Zheng, K. Cheng, X. Zhou, J. Lin, and X. Jing, "A method for positioning the focal spot location of two photon polymerization," *AIP Advances,* vol. 7, no. 9, 2017, doi: 10.1063/1.4986102.

[234] F. Sima, K. Sugioka, R. M. Vázquez, R. Osellame, L. Kelemen, and P. Ormos, "Three-dimensional femtosecond laser processing for lab-on-a-chip applications," *Nanophotonics,* vol. 7, no. 3, pp. 613-634, 2018, doi: 10.1515/nanoph-2017-0097.

[235] M. Rothschild, "Projection optical lithography," *Materials Today,* vol. 8, no. 2, pp. 18-24, 2005/02/01/ 2005, doi: 10.1016/S1369-7021(05)00698-X.

[236] C. W. Ha, P. Prabhakaran, and Y. Son, "3D-Printed Polymer/Metal Hybrid Microstructures with Ultraprecision for 3D Microcoils," *3D Printing and Additive Manufacturing,* vol. 6, no. 3, pp. 165-170, 2019/06/01 2019, doi: 10.1089/3dp.2018.0139.

[237] R. Winkler, J. D. Fowlkes, P. D. Rack, and H. Plank, "3D nanoprinting via focused electron beams," *Journal of Applied Physics,* vol. 125, no. 21, 2019, doi: 10.1063/1.5092372.

[238] P. Orús, F. Sigloch, S. Sangiao, and J. M. De Teresa, "Superconducting Materials and Devices Grown by Focused Ion and Electron Beam Induced Deposition," *Nanomaterials,* vol. 12, no. 8, p. 1367, 2022. [Online]. Available: https://www.mdpi.com/2079-4991/12/8/1367.

[239] A. Fernández-Pacheco, L. Skoric, J. M. De Teresa, J. Pablo-Navarro, M. Huth, and O. V. Dobrovolskiy, "Writing 3D Nanomagnets Using Focused Electron Beams," (in eng), *Materials (Basel),* vol. 13, no. 17, Aug 26 2020, doi: 10.3390/ma13173774.

[240] M. Toth, C. Lobo, V. Friedli, A. Szkudlarek, and I. Utke, "Continuum models of focused electron beam induced processing," *Beilstein Journal of Nanotechnology,* vol. 6, pp. 1518-1540, // 2015, doi: 10.3762/bjnano.6.157.

[241] W. F. van Dorp and C. W. Hagen, "A critical literature review of focused electron beam induced deposition," *Journal of Applied Physics,* vol. 104, no. 8, 2008, doi: 10.1063/1.2977587.
[242] M. Huth, F. Porrati, and O. V. Dobrovolskiy, "Focused electron beam induced deposition meets materials science," *Microelectronic Engineering,* vol. 185-186, pp. 9-28, 2018/01/05/ 2018, doi: 10.1016/j.mee.2017.10.012.
[243] M. Jaafar *et al.*, "Customized MFM probes based on magnetic nanorods," *Nanoscale,* 10.1039/D0NR00322K vol. 12, no. 18, pp. 10090-10097, 2020, doi: 10.1039/D0NR00322K.
[244] H. Mattiat *et al.*, "Nanowire Magnetic Force Sensors Fabricated by Focused-Electron-Beam-Induced Deposition," *Physical Review Applied,* vol. 13, no. 4, p. 044043, 04/16/ 2020, doi: 10.1103/PhysRevApplied.13.044043.
[245] B. J. Nelson and L. Dong, "Nanorobotics," in *Springer Handbook of Nanotechnology*, B. Bhushan Ed. Berlin, Heidelberg: Springer Berlin Heidelberg, 2010, pp. 1633-1659.
[246] W. Tiddi, A. Elsukova, H. T. Le, P. Liu, M. Beleggia, and A. Han, "Organic Ice Resists," *Nano Letters,* vol. 17, no. 12, pp. 7886-7891, 2017/12/13 2017, doi: 10.1021/acs.nanolett.7b04190.
[247] W. Tiddi, A. Elsukova, M. Beleggia, and A. Han, "Organic ice resists for 3D electron-beam processing: Instrumentation and operation," *Microelectronic Engineering,* vol. 192, pp. 38-43, 2018/05/15/ 2018, doi: 10.1016/j.mee.2018.01.021.
[248] J. A. Lewis and G. M. Gratson, "Direct writing in three dimensions," *Materials Today,* vol. 7, no. 7, pp. 32-39, 2004/07/01/ 2004, doi: 10.1016/S1369-7021(04)00344-X.
[249] E. J. Brandon, E. E. Wesseling, C. Vincent, and W. B. Kuhn, "Printed microinductors on flexible substrates for power applications," *IEEE Transactions on Components and Packaging Technologies,* vol. 26, no. 3, pp. 517-523, 2003, doi: 10.1109/TCAPT.2003.817641.
[250] T. Zhang, X. Wang, T. Li, Q. Guo, and J. Yang, "Fabrication of flexible copper-based electronics with high-resolution and high-conductivity on paper via inkjet printing," *Journal of Materials Chemistry C,* vol. 2, no. 2, pp. 286-294, 2014, doi: 10.1039/C3TC31740D.
[251] X. Wang, L. Xu, G. Zheng, W. Cheng, and D. Sun, "Pulsed electrohydrodynamic printing of conductive silver patterns on demand," *Science China Technological Sciences,* vol. 55, no. 6, pp. 1603-1607, 2012/06/01 2012, doi: 10.1007/s11431-012-4843-4.
[252] R. R. Sarreal and P. Bhatti, "Characterization and Miniaturization of Silver-Nanoparticle Microcoil via Aerosol Jet Printing Techniques for Micromagnetic Cochlear Stimulation," *Sensors,* vol. 20, no. 21, p. 6087, 2020, doi: 10.3390/s20216087.
[253] G. McKerricher, M. Vaseem, and A. Shamim, "Fully inkjet-printed microwave passive electronics," *Microsystems & Nanoengineering,* vol. 3, no. 1, p. 16075, 2017/01/30 2017, doi: 10.1038/micronano.2016.75.
[254] J.-U. Park *et al.*, "High-resolution electrohydrodynamic jet printing," *Nature Materials,* vol. 6, no. 10, pp. 782-789, 2007/10/01 2007, doi: 10.1038/nmat1974.
[255] G. L. Goh, V. Dikshit, R. Koneru, Z. K. Peh, W. Lu, G. D. Goh, and W. Y. Yeong, "Fabrication of design-optimized multifunctional safety cage with conformal circuits for drone using hybrid 3D printing technology," *The International Journal of Advanced Manufacturing Technology,* vol. 120, no. 3, pp. 2573-2586, 2022/05/01 2022, doi: 10.1007/s00170-022-08831-y.
[256] D. A. Pardo, G. E. Jabbour, and N. Peyghambarian, "Application of Screen Printing in the Fabrication of Organic Light-Emitting Devices," *Advanced Materials,* vol. 12, no. 17, pp. 1249-1252, 2000, doi: 10.1002/1521-4095(200009)12:17<1249::AID-ADMA1249>3.0.CO;2-Y.
[257] Y. Wang, Y. Shi, C. X. Zhao, J. I. Wong, X. W. Sun, and H. Y. Yang, "Printed all-solid flexible microsupercapacitors: towards the general route for high energy storage devices," *Nanotechnology,* vol. 25, no. 9, p. 094010, 2014/02/12 2014, doi: 10.1088/0957-4484/25/9/094010.
[258] A. Pepłowski *et al.*, "Electrochemistry of Graphene Nanoplatelets Printed Electrodes for Cortical Direct Current Stimulation," (in English), *Frontiers in Neuroscience,* Brief Research Report vol. 14, 2020-October-29 2020, doi: 10.3389/fnins.2020.594235.
[259] A. Han, J. Chervinsky, D. Branton, and J. A. Golovchenko, "An ice lithography instrument," *Review of Scientific Instruments,* vol. 82, no. 6, 2011, doi: 10.1063/1.3601005.
[260] E. Saleh *et al.*, "3D Inkjet Printing of Electronics Using UV Conversion," *Advanced Materials Technologies,* vol. 2, no. 10, p. 1700134, 2017, doi: 10.1002/admt.201700134.

[261] "3D-Printed Polymer/Metal Hybrid Microstructures with Ultraprecision for 3D Microcoils," *3D Printing and Additive Manufacturing,* vol. 6, no. 3, pp. 165-170, 2019, doi: 10.1089/3dp.2018.0139.
[262] J. A. Rogers, R. J. Jackman, G. M. Whitesides, D. L. Olson, and J. V. Sweedler, "Using microcontact printing to fabricate microcoils on capillaries for high resolution proton nuclear magnetic resonance on nanoliter volumes," *Applied physics letters,* vol. 70, no. 18, pp. 2464-2466, 1997, doi: 10.1063/1.118857.
[263] A. Khalifa, "Design, Fabrication, and Validation of a Highly Miniaturized Wirelessly Powered Neural Implant," Johns Hopkins University, 2019.
[264] M. S. Onses, E. Sutanto, P. M. Ferreira, A. G. Alleyne, and J. A. Rogers, "Mechanisms, capabilities, and applications of high‐resolution electrohydrodynamic jet printing," *Small,* vol. 11, no. 34, pp. 4237-4266, 2015, doi: 10.1002/smll.201500593.
[265] O. A. Basaran, "Small-scale free surface flows with breakup: Drop formation and emerging applications," *American Institute of Chemical Engineers. AIChE Journal,* vol. 48, no. 9, p. 1842, 2002.
[266] P. Galliker, J. Schneider, H. Eghlidi, S. Kress, V. Sandoghdar, and D. Poulikakos, "Direct printing of nanostructures by electrostatic autofocussing of ink nanodroplets," *Nature Communications,* vol. 3, no. 1, p. 890, 2012/06/12 2012, doi: 10.1038/ncomms1891.
[267] S. J. P. Kress, P. Richner, S. V. Jayanti, P. Galliker, D. K. Kim, D. Poulikakos, and D. J. Norris, "Near-Field Light Design with Colloidal Quantum Dots for Photonics and Plasmonics," *Nano Letters,* vol. 14, no. 10, pp. 5827-5833, 2014/10/08 2014, doi: 10.1021/nl5026997.
[268] P. Galliker, J. Schneider, L. Rüthemann, and D. Poulikakos, "Open-atmosphere sustenance of highly volatile attoliter-size droplets on surfaces," *Proceedings of the National Academy of Sciences,* vol. 110, no. 33, pp. 13255-13260, 2013, doi: 10.1073/pnas.1305886110.
[269] J. Schneider, P. Rohner, D. Thureja, M. Schmid, P. Galliker, and D. Poulikakos, "Electrohydrodynamic NanoDrip Printing of High Aspect Ratio Metal Grid Transparent Electrodes," *Advanced Functional Materials,* vol. 26, no. 6, pp. 833-840, 2016, doi: 10.1002/adfm.201503705.
[270] P. Richner, P. Galliker, T. Lendenmann, S. J. P. Kress, D. K. Kim, D. J. Norris, and D. Poulikakos, "Full-Spectrum Flexible Color Printing at the Diffraction Limit," *ACS Photonics,* vol. 3, no. 5, pp. 754-757, 2016/05/18 2016, doi: 10.1021/acsphotonics.6b00131.
[271] D.-Y. Lee, Y.-S. Shin, S.-E. Park, T.-U. Yu, and J. Hwang, "Electrohydrodynamic printing of silver nanoparticles by using a focused nanocolloid jet," *Applied Physics Letters,* vol. 90, no. 8, p. 081905, 2007, doi: 10.1063/1.2645078.
[272] D. Gao and J. G. Zhou, "Designs and applications of electrohydrodynamic 3D printing," *International journal of bioprinting,* vol. 5, no. 1, 2019.
[273] H. Zhou and Y. Song, "Fabrication of Electronics by Electrohydrodynamic Jet Printing," *Advanced Electronic Materials,* vol. 8, no. 11, p. 2200728, 2022, doi: 10.1002/aelm.202200728.
[274] W. Chen, C. S. Fernandez, L. Xu, E. Velliou, S. Homer-Vanniasinkam, and M. K. Tiwari, "9 - High-resolution 3D printing for healthcare," in *3D Printing in Medicine (Second Edition)*, D. M. Kalaskar Ed.: Woodhead Publishing, 2023, pp. 225-271.
[275] J. Kim, H. Oh, and S. S. Kim, "Electrohydrodynamic drop-on-demand patterning in pulsed cone-jet mode at various frequencies," *Journal of Aerosol Science,* vol. 39, no. 9, pp. 819-825, 2008/09/01/ 2008, doi: 10.1016/j.jaerosci.2008.05.001.
[276] M. Alhendi *et al.*, "Printed electronics for extreme high temperature environments," *Additive Manufacturing,* vol. 54, p. 102709, 2022/06/01/ 2022, doi: 10.1016/j.addma.2022.102709.
[277] E. B. Secor, "Principles of aerosol jet printing," *Flexible and Printed Electronics,* vol. 3, no. 3, p. 035002, 2018, doi: 10.1088/2058-8585/aace28.
[278] C. Hollar *et al.*, "High-Performance Flexible Bismuth Telluride Thin Film from Solution Processed Colloidal Nanoplates," *Advanced Materials Technologies,* vol. 5, no. 11, p. 2000600, 2020, doi: 10.1002/admt.202000600.
[279] T. Pandhi *et al.*, "Fully inkjet-printed multilayered graphene-based flexible electrodes for repeatable electrochemical response," *Rsc Advances,* vol. 10, no. 63, pp. 38205-38219, 2020, doi: 10.1039/D0RA04786D.
[280] M. T. Craton, J. D. Albrecht, P. Chahal, and J. Papapolymerou, "Multimaterial Aerosol Jet Printed Magnetic Nanocomposites for Microwave Circuits," *IEEE Transactions on*

Components, Packaging and Manufacturing Technology, vol. 11, no. 5, pp. 865-871, 2021, doi: 10.1109/TCPMT.2021.3071113.

[281] Y. Gu, D. Park, S. Gonya, J. Jendrisak, S. Das, and D. R. Hines, "Direct-write printed broadband inductors," *Additive Manufacturing,* vol. 30, p. 100843, 2019/12/01/ 2019, doi: 10.1016/j.addma.2019.100843.

[282] L.-k. Tsui, Y. Sui, T. M. Hartmann, J. Dye, and J. M. Lavin, "Additive Manufacturing of Inductors and Transformers by Hybrid Aerosol Jet Printing and Electrochemical Deposition," *ECS Meeting Abstracts,* vol. MA2023-01, no. 22, p. 1558, 2023/08/28 2023, doi: 10.1149/MA2023-01221558mtgabs.

[283] S. Krainer, C. Smit, and U. Hirn, "The effect of viscosity and surface tension on inkjet printed picoliter dots," *RSC advances,* vol. 9, no. 54, pp. 31708-31719, 2019, doi: 10.1039/C9RA04993B.

[284] B. Derby, "Inkjet printing of functional and structural materials: fluid property requirements, feature stability, and resolution," *Annual Review of Materials Research,* vol. 40, pp. 395-414, 2010, doi: 10.1146/annurev-matsci-070909-104502.

[285] G. Grau, J. Cen, H. Kang, R. Kitsomboonloha, W. J. Scheideler, and V. Subramanian, "Gravure-printed electronics: recent progress in tooling development, understanding of printing physics, and realization of printed devices," *Flexible and Printed Electronics,* vol. 1, no. 2, p. 023002, 2016, doi: 10.1088/2058-8585/1/2/023002.

[286] R. Kitsomboonloha, S. Morris, X. Rong, and V. Subramanian, "Femtoliter-scale patterning by high-speed, highly scaled inverse gravure printing," *Langmuir,* vol. 28, no. 48, pp. 16711-16723, 2012, doi: 10.1021/la3037132.

[287] R. Wu and J. K. O. Sin, "A Novel Silicon-Embedded Coreless Inductor for High-Frequency Power Management Applications," *IEEE Electron Device Letters,* vol. 32, no. 1, pp. 60-62, 2011, doi: 10.1109/LED.2010.2082489.

[288] H. T. Le *et al.*, "Fabrication of 3D air-core MEMS inductors for very-high-frequency power conversions," *Microsystems & Nanoengineering,* vol. 4, no. 1, p. 17082, 2018/01/29 2018, doi: 10.1038/micronano.2017.82.

[289] M. J. K. Klein, T. Ono, M. Esashi, and J. G. Korvink, "Process for the fabrication of hollow core solenoidal microcoils in borosilicate glass," *Journal of Micromechanics and Microengineering,* vol. 18, no. 7, p. 075002, 2008/05/20 2008, doi: 10.1088/0960-1317/18/7/075002.

[290] H. T. Le *et al.*, "High-Q Three-Dimensional Microfabricated Magnetic-Core Toroidal Inductors for Power Supplies in Package," *IEEE Transactions on Power Electronics,* vol. 34, no. 1, pp. 74-85, 2019, doi: 10.1109/TPEL.2018.2847439.

[291] H. Y. Li *et al.*, "Three-Dimensional Solenoids Realized via High-Density Deep Coil Stacking for MEMS Application," *IEEE Electron Device Letters,* vol. 33, no. 3, pp. 432-434, 2012, doi: 10.1109/LED.2011.2182601.

[292] T. Sun, H. Sharma, P. M. Raj, F. Yoshihiro, S. Hachiya, K. Takemura, and R. Tummala, "Substrate-Embedded Low-Resistance Solenoid Inductors for Integrated Voltage Regulators," *IEEE Transactions on Components, Packaging and Manufacturing Technology,* vol. 10, no. 1, pp. 134-141, 2020, doi: 10.1109/TCPMT.2019.2956528.

[293] S. J. Bleiker *et al.*, "High-Aspect-Ratio Through Silicon Vias for High-Frequency Application Fabricated by Magnetic Assembly of Gold-Coated Nickel Wires," *IEEE Transactions on Components, Packaging and Manufacturing Technology,* vol. 5, no. 1, pp. 21-27, 2015, doi: 10.1109/TCPMT.2014.2369236.

[294] H. Li, J. Liu, T. Xu, J. Xia, X. Tan, and Z. Tao, "Fabrication and Optimization of High Aspect Ratio Through-Silicon-Vias Electroplating for 3D Inductor," (in eng), *Micromachines (Basel),* vol. 9, no. 10, Oct 18 2018, doi: 10.3390/mi9100528.

[295] W. Zhang, J. Gu, G. Xu, L. Luo, and X. Li, "An optimized through-via bottom-up method for simultaneous-filling TSVS of different aspect-ratios and its potential application on high-frequency passive interposer," *Microelectronics Journal,* vol. 101, p. 104798, 2020/07/01/ 2020, doi: 10.1016/j.mejo.2020.104798.

[296] Z. Tao, J. Sun, H. Li, Y. Huang, H. Li, T. Xu, and H. Wu, "A Radial-Flux Permanent Magnet Micromotor With 3D Solenoid Iron-Core MEMS In-Chip Coils of High Aspect Ratio," *IEEE Electron Device Letters,* vol. 41, no. 7, pp. 1090-1093, 2020, doi: 10.1109/LED.2020.2998356.

[297] R. Anthony, E. Laforge, D. P. Casey, J. F. Rohan, and C. O'Mathuna, "High-aspect-ratio photoresist processing for fabrication of high resolution and thick micro-windings," *Journal of Micromechanics and Microengineering,* vol. 26, no. 10, p. 105012, 2016/09/07 2016, doi: 10.1088/0960-1317/26/10/105012.
[298] B. Magali, O. D. Terence, O. B. Joe, M. Paul, and M. Seán Cian Ó, "Thick photoresist development for the fabrication of high aspect ratio magnetic coils," *Journal of Micromechanics and Microengineering,* vol. 12, no. 4, p. 444, 2002/06/19 2002, doi: 10.1088/0960-1317/12/4/317.
[299] D. Bourrier, A. Ghannam, M. Dilhan, and H. Granier, "Potential of BPN as a new negative photoresist for a very thick layer with high aspect ratio," *Microsystem Technologies,* vol. 20, no. 10, pp. 2089-2096, 2014/10/01 2014, doi: 10.1007/s00542-014-2071-5.
[300] D. V. Harburg *et al.*, "Microfabricated Racetrack Inductors With Thin-Film Magnetic Cores for On-Chip Power Conversion," *IEEE Journal of Emerging and Selected Topics in Power Electronics,* vol. 6, no. 3, pp. 1280-1294, 2018, doi: 10.1109/JESTPE.2018.2808375.
[301] R. Anthony, N. Wang, D. P. Casey, C. Ó Mathúna, and J. F. Rohan, "MEMS based fabrication of high-frequency integrated inductors on Ni–Cu–Zn ferrite substrates," *Journal of Magnetism and Magnetic Materials,* vol. 406, pp. 89-94, 2016/05/15/ 2016, doi: 10.1016/j.jmmm.2015.12.099.
[302] X. Liu *et al.*, "MEMS micro-coils for magnetic neurostimulation," *Biosensors and Bioelectronics,* vol. 227, p. 115143, 2023/05/01/ 2023, doi: 10.1016/j.bios.2023.115143.
[303] H.-J. Park, H. Kang, J. Jo, E. Chung, and S. Kim, "Planar coil-based contact-mode magnetic stimulation: synaptic responses in hippocampal slices and thermal considerations," *Scientific Reports,* vol. 8, no. 1, p. 13423, 2018/09/07 2018, doi: 10.1038/s41598-018-31536-w.
[304] Y. Matsumoto, M. Setomoto, D. Noda, and T. Hattori, "Cylindrical coils created with 3D X-ray lithography and metallization," *Microsystem Technologies,* vol. 14, no. 9, pp. 1373-1379, 2008/10/01 2008, doi: 10.1007/s00542-007-0547-2.
[305] M. Colella *et al.*, "A study of flex miniaturized coils for focal nerve magnetic stimulation," *Medical Physics,* vol. 50, no. 3, pp. 1779-1792, 2023, doi: 10.1002/mp.16148.
[306] I. Utke, J. Michler, R. Winkler, and H. Plank, "Mechanical Properties of 3D Nanostructures Obtained by Focused Electron/Ion Beam-Induced Deposition: A Review," *Micromachines,* vol. 11, no. 4, p. 397, 2020. [Online]. Available: https://www.mdpi.com/2072-666X/11/4/397.
[307] H. G. Gnanasambanthan and D. Maji, "Development of a Flexible and Wearable Microelectrode Array Patch Using a Screen-Printed Masking Technique for Accelerated Wound Healing," *ACS Applied Electronic Materials,* vol. 5, no. 8, pp. 4426-4436, 2023/08/22 2023, doi: 10.1021/acsaelm.3c00637.
[308] A. Imai *et al.*, "Flexible Thin-Film Neural Electrodes with Improved Conformability for ECoG Measurements and Electrical Stimulation," *Advanced Materials Technologies,* vol. 8, no. 21, p. 2300300, 2023, doi: 10.1002/admt.202300300.
[309] X. Yu, W. Huang, M. Li, T. M. Comberiate, S. Gong, J. E. Schutt-Aine, and X. Li, "Ultra-Small, High-Frequency and Substrate-Immune Microtube Inductors Transformed from 2D to 3D," *Scientific Reports,* vol. 5, no. 1, p. 9661, 2015/04/27 2015, doi: 10.1038/srep09661.
[310] W. Huang *et al.*, "Monolithic mtesla-level magnetic induction by self-rolled-up membrane technology," *Science Advances,* vol. 6, no. 3, p. eaay4508, 2020, doi: doi:10.1126/sciadv.aay4508.
[311] W. Huang *et al.*, "Three-dimensional radio-frequency transformers based on a self-rolled-up membrane platform," *Nature Electronics,* vol. 1, no. 5, pp. 305-313, 2018/05/01 2018, doi: 10.1038/s41928-018-0073-5.
[312] W. Rushton, "The effect upon the threshold for nervous excitation of the length of nerve exposed, and the angle between current and nerve," *The Journal of physiology,* vol. 63, no. 4, p. 357, 1927, doi: 10.1113/jphysiol.1927.sp002409.
[313] J. B. Ranck Jr, "Which elements are excited in electrical stimulation of mammalian central nervous system: a review," *Brain research,* vol. 98, no. 3, pp. 417-440, 1975, doi: 10.1016/0006-8993(75)90364-9.
[314] D. R. McNeal, "Analysis of a model for excitation of myelinated nerve," *IEEE Transactions on Biomedical Engineering,* no. 4, pp. 329-337, 1976.
[315] M. Alzahrani and B. J. Roth, "The electric field induced by a microcoil during magnetic stimulation," *IEEE Transactions on Biomedical Engineering,* vol. 70, no. 11, pp. 3260-3262, 2023.

[316] E. McGlynn, B. P. Yalagala, and H. Heidari, "Microfabrication of Implantable, Flexible Neural Probes Towards Bidirectional Interfacing in the Deep Brain," 2022, no. Conference Proceedings. [Online]. Available: https://go.exlibris.link/v5NhS5r5. [Online]. Available: https://go.exlibris.link/v5NhS5r5
[317] A. G. Roca, B. Wiese, J. Timmis, G. Vallejo-Fernandez, and K. O'Grady, "Effect of Frequency and Field Amplitude in Magnetic Hyperthermia," (in English), *IEEE transactions on magnetics,* vol. 48, no. 11, pp. 4054-4057, 2012, doi: 10.1109/TMAG.2012.2201459.
[318] Z. Zhang, K. T. Chau, C. Qiu, and C. Liu, "Energy Encryption for Wireless Power Transfer," (in English), *IEEE transactions on power electronics,* vol. 30, no. 9, pp. 5237-5246, 2015, doi: 10.1109/TPEL.2014.2363686.

7 Appendix

7.1 Preparation and Experiment Setup

MASMCs were isolated previously from mouse aortas of C57BLK6/J mice (Envigo - UK). A stock of both cells is stored at –135°C in liquid nitrogen storage within sterile cryogenic storage vials (E3110-6122, StarLab). They are stored at a density of 1x106 cells/mL in 10 % Dimethyl Sulfoxide (DMSO) (D/4120/PB08, Fisher scientific, UK). In order to culture the cells for experiments, vials were defrosted rapidly in a 37°C water bath. 1 mL of culture media was added to the thawed cells and the cells were spun at 1500 rpm for 5 minutes. The supernatant was removed, and the pellet was broken up in 1 mL of culture media. The suspended cells were then transferred to a vented T75 culture flask (430641, Corning, USA). MASMCs were cultivated in Dulbecco's Modified Eagle's Medium (DMEM) (21885025, Gibco, ThermoFisher) with 10 % Foetal Bovine Serum (10270106, Gibco, ThermoFisher) and 5 % penicillin (10,000 units) streptomycin (10 mg) (P0781, Sigma-Aldrich, Merck). Culture flasks containing cells were incubated in an incubator at 37°C with 95% relative humidity and 5% CO2. Every experiment that required cell culturing was placed within an incubator with the same temperature, humidity and CO2 levels of 37°C, 95% and 5% respectively.

Initially, culture media is aspirated and discarded from the T75 flask. The flasks are then rinsed twice with 5 mL of Dulbecco's phosphate-buffered saline (PBS) (14190094, Gibco, ThermoFisher) to eliminate excess calcium. Following the removal of PBS, cells are trypsinized from the flask using 2.5 mL of Trypsin-EDTA solution (T3924, Sigma Aldrich, Merck). Subsequently, the cells are returned to the incubator for 5 minutes and examined under a microscope for detachment from the flask. Once detachment is observed, the cells in Trypsin EDTA are transferred to a sterile centrifuge tube (430790, Corning, USA). The Trypsin EDTA is neutralized with 2.5 mL of DMEM with HEPES, and the mixture is aspirated from the tube. A portion of this stock solution is then placed on a hemocytometer

for cell counting. The centrifuge tube is spun at 1500 rpm for 5 minutes, after which the supernatant is discarded, leaving a pellet of cells. The pellet is disaggregated and resuspended in DMEM with HEPES to create a stock solution.

Prior to cell seeding, each experimental material was sterilized with 70% ethanol and rinsed thrice with dH2O to remove any ethanol residue within a sterile laminar flow hood. These experimental materials were then placed in their respective well. Cells were subsequently seeded at the 100,000 densities per well to a sterile 12 well plate cell culture plate (ThermoFisher, Massachusetts, United States), and incubated for 24 hours.

After 24 hours of cell proliferation, Acridine Orange/Propidium Iodide staining solution was prepared to stain SMCs. Acridine orange was prepared through dissolving 5 µL of 10 mg/mL of acridine orange (AO) (Sigma-Aldrich, USA) in 10 mL of PBS firstly. 1.5 mL propidium iodide solution (PI, eBioscience, San Diego, United States) was then mixed with AO to cover the cell monolayer in equal amount like 25 µL of AO mixed with 25 µL of PI to form the final staining with volume of 50 µL. Prior to staining, all previous culture media was removed, and cell monolayer was washed with PBS to remove any residue. Culture plates were then carried and mounted to an Olympus IX71 (Olympus Corporation, Japan) for fluorescent imaging once the staining solution was pipetted to the each well of the culture plates. Prior to imaging, a specially built heating hood around the microscope was heated to 37°C to improve the atmospheric conditions for MASMCs during imaging.

7.2 Arduino Code

```
const int analogPin = A0;

void setup() {
  // put your setup code here, to run once:
  analogReference(DEFAULT);
  Serial.begin(9600);
}

void loop() {
  int sensorValue = analogRead(analogPin);              // read analogue value
 (0-1023)
  float R = 1023.0/sensorValue-1.0;         // convert to voltage value
  float T=(3950/(log(R)+13.25))-279.15;
  Serial.print(T);
  Serial.println("");
  delay(100);
}
```

7.3 Python Code

```
def draw_spiral_polygon(sides, turns, ri, ro):
    # sides: number of sides
    # turns: number of turns

    theta = np.linspace(0, 2 * np.pi * turns, sides * turns + 1)
    radius = np.linspace(ri, ro, sides * turns + 1)

    x = radius * np.cos(theta)
    y = radius * np.sin(theta)

    doc = ezdxf.new(dxfversion='R2010')
    msp = doc.modelspace()

    # draw each side
    for i in range(sides * turns):
        msp.add_line((x[i], y[i]) , (x[i+1], y[i+1]))

    doc.saveas('C:xxxxxx/file.dxf')# save as dxf file

# Use Function to draw the patern
draw_spiral_polygon(sides=6, turns=10, ri=0.1, ro=1.0)
```